MATERIAL DESIGN AND FUNDAMENTAL MECHANISM STUDY FOR THE RECHARGEABLE APROTIC LITHIUM-OXYGEN BATTERY

by

Xiangyi Luo

A dissertation submitted to the faculty of
The University of Utah
in partial fulfillment of the requirements for the degree of

Doctor of Philosophy

Department of Metallurgical Engineering

The University of Utah

May 2015

The University of Utah Graduate School

STATEMENT OF DISSERTATION APPROVAL

The dissertation of **Xiangyi Luo**

has been approved by the following supervisory committee members:

Zhigang Zak Fang	, Chair	**11-26-2014** Date Approved
Michael L. Free	, Member	**11-26-2014** Date Approved
Sivaraman Guruswamy	, Member	**11-26-2014** Date Approved
Jun Lu	, Member	**11-26-2014** Date Approved
Yang Ren	, Member	**11-26-2014** Date Approved

and by **Michael L. Free** , Chair/Dean of

the Department/College/School of **Metallurgical Engineering**

and by David B. Kieda, Dean of The Graduate School.

ABSTRACT

The rechargeable Li-O_2 battery is still in its infancy. More studies are required before a commercial product can be reached. My research aims at the major hurdles in current research, such as the fundamental mechanism and the high overpotential of the electrochemical reactions. In this dissertation, firstly, I demonstrated the mass and charge transport relevant to the formation of toroidal Li_2O_2 nanoparticles during the discharge/charge cycles in an aprotic Li-O_2 cell. The accumulations of the discharge product Li_2O_2 not only clog the O_2 pathway in the cathode, but also hinder the charge transfer process. Overfull Li_2O_2 requires extra energy to break its chemical bonds during charge, and causes a high charge overpotential. Electrocatalysts were employed to lower the charge overpotential.

In the second part of this dissertation, atomic layer deposition (ALD) was used to deposit nanostructured palladium on porous carbon as the cathode material for Li-O_2 cells. STEM showed discrete crystalline nanoparticles decorating the surface of the porous carbon support, where the size could be controlled in the range of 2-8 nm depending on the number of Pd ALD cycles performed. X-ray absorption spectroscopy at the Pd K-edge revealed that the carbon supported Pd existed in a mixed phase of metallic

palladium and palladium oxide. The conformality of ALD allowed us to uniformly disperse the Pd catalyst onto the carbon support while preserving the initial porous structure. As a result, the charging and discharging performance of the oxygen cathode in a Li-O_2 cell was improved. These results suggest that ALD is a promising technique for tailoring the surface composition and structure of nanoporous supports in energy storage devices.

Furthermore, uniformly dispersed Pd nanoparticles on ZnO-passivated porous carbon were synthesized via an atomic layer deposition (ALD) technique, which was tested as a cathode material in a rechargeable Li-O_2 battery, showing highly active catalytic effect towards the electrochemical reactions, in particular, oxygen evolution reaction. Transmission electron microscopy showed discrete crystalline nanoparticles decorating the surface of the ZnO-passivated porous carbon support, where the size could be controlled in the range of 3-6 nm depending on the number of Pd ALD cycles performed. X-ray absorption spectroscopy at the Pd K-edge revealed that the carbon supported Pd existed in a mixed phase of metallic palladium and palladium oxide. These results suggest that ALD is a promising technique for tailoring the surface composition and structure of nanoporous supports for Li-O_2 batteries.

TABLE OF CONTENTS

LIST OF FIGURES

LIST OF TABLES

LIST OF ABBREVIATIONS

1NM3	Tri(ethylene glycol)-substituted methyltrimethyl silane
AIMD	*Ab initio* molecular dynamics
Al	Aluminum
Al_2O_3	Alumina
ALD	Atomic layer deposition
Ar	Argon
Au	Gold
C	Carbon
CH_3CO_2Li	Lithium acetate
CH_3Li	Methyllithium
CH_3OLi	Lithium methoxide
CNT	Carbon nanotube
CO_2	Carbon dioxide
Co_3O_4	Cobaltosic oxide
$CoFe_2O_4$	Cobalt ferrite
CuO	Cupric oxide
DEC	Diethyl carbonate
DFT	Density functional theory

DMC	Dimethyl carbonate
DME	1,2-dimethoxyethane
DOS	Density of states
EC	Ethylene carbonate
EDX	Energy-dispersive X-ray spectroscopy
EIS	Electrochemical impedance spectroscopy
EPR	Electron paramagnetic resonance
EXAFS	Extended X-ray absorption fine structure
fcc	Face-centered cubic
Fe_2O_3	Ferric oxide
Fe_3O_4	Ferriferrous oxide
FGS	Functionalized graphene sheets
H_2O	Water
HCO_2Li	Lithium formate
HE-XRD	High energy X-ray diffraction
HF	Hydrogen fluoride
HR-TEM	High-resolution transmission electron microscope
Li	Lithium
Li_2CO_3	Lithium carbonate
Li_2O	Lithium oxide
Li_2O_2	Lithium peroxide
$LiCF_3SO_3$	Lithium trifluoromethanesulfonate; Lithium triflate
LiF	Lithium fluoride

LiO_2	Lithium superoxide
LiOH	Lithium hydroxide
$LiPF_6$	Lithium hexafluorophosphate
LiTFSI	Lithium bis(trifluoromethane sulfonimide)
Mg	Magnesium
MnO_2	Manganese dioxide
MSD	Mean square displacement
N_2	Nitrogen
NMP	1-methyl-2-pyrrolidinone
O_2	Oxygen
O^{2-}	Oxide ion
O_2^-	Superoxide ion
O_2^{2-}	Peroxide ion
OER	Oxygen evolution reaction
ORR	Oxygen reduction reaction
PC	Propylene carbonate
Pd	Palladium
PdO	Palladium oxide
Pt	Platinum
PVDF	Polyvinylidene fluoride
rGO	Reduced graphene oxide
SEI	Solid-electrolyte interface
SEM	Scanning electron microscopy

SPL	Super P Li conductive carbon black
STEM	Scanning transmission electron microscopy
TEGDME	Tetraethylene glycol dimethyl ether
TEM	Transmission electron microscopy
USABC	United States Advanced Battery Consortium
XAFS	X-ray absorption fine structure
XANES	X-ray absorption near edge structure
XAS	X-ray absorption spectroscopy
XPS	X-ray photoelectron spectroscopy
XRD	X-ray diffraction
ZnO	Zinc oxide

ACKNOWLEDGEMENTS

Foremost, I would like to express my sincere gratitude to my advisor Prof. Z. Zak Fang for continuous support of my Ph.D. study and research, for his patience and motivation. His guidance helped me in all the time of research and writing of this dissertation. I could not have imagined having a better advisor and mentor for my Ph.D. study. I also wish to show my heartfelt thanks to my co-advisor Dr. Jun Lu for his constant guidance and encouragement throughout my research. His enthusiasm and immense knowledge in the field of energy storage materials have been a constant source of inspiration. This dissertation would not have been possible without their advice and support.

Besides my advisors, I would like to thank the rest of my dissertation committee: Prof. Michael L. Free, Prof. Sivaraman Guruswamy, and Dr. Yang Ren, for their encouragement, insightful comments, and hard questions.

I am grateful to all members of the battery research in Argonne National Laboratory who made this dissertation possible, in particular to Dr. Kah-Chun Lau for the computer modelling of simulation, which is of great help to understand the mechanism theoretically. And I must acknowledge Dr. Yu Lei for the atomic layer deposition

technique. Also, excellent support and assistance were received from Dr. Yang Ren, Dr. Tianpin Wu, and Dr. Jianguo Wen for the characterization methods. The financial support from the graduate student programs by Division of Educational Programs in Argonne National Laboratory is gratefully acknowledged.

I would like to thank my labmates in the Advanced Battery Technology Group in Argonne and the Powder Metallurgy Research Group in University of Utah (sequenced by last name): Jingzhu Li, Yan Li, Pei Sun, Rui Xu, Zhenzhen Yang, Chun Zhan, and Chengshang Zhou, for the stimulating discussions on research, for the official procedures when I was off campus, and for all the fun we have had in the last three years. Also it is a pleasure to thank my friends (sequenced by last name): Qin Dai, Yu Dai, Yanfei Mao, Sichun Sun, Xiaolin Tang, Chen Zhang, and Mingyuan Zhang, for their encouragement and company since I came to the US in 2008, although we are far apart geographically now.

Last but not least, I owe my deepest gratitude to my parents, Jichun Luo and Yinghua Chen, for giving birth and love to me at the first place and supporting me spiritually throughout my life.

CHAPTER 1

INTRODUCTION

In modern times, environmental pollution is aggravated due to the increasing reliance on fossil fuels, which produce around 20 billion tons of CO_2 and a large quantity of other green-house gas per year in the atmosphere, causing global warming.[1] The combustion products of fossil fuels fall to Earth as acid rain, which impacts both the natural and built environment. On the other hand, it takes millions of years to form fossil fuels from the remains of organisms, but only a few hundreds of years to deplete all the known reserves. The rising use of fossil fuels and decrease of supply will lead to a serious energy crisis. To reduce the emission of green-house gas and the reliance on fossil fuels, the world is seeking alternative green energy sources, such as nuclear energy and renewable energy sources (*e.g.*, solar power, hydropower, wind power, geothermal energy, etc.).[2] The main purpose of developing these energy sources is power generation. Thus accumulators—the devices that store electrical energy—come as an answer to the acute demand. Meanwhile, electrical energy storage has been a major element in economic development of modern states.

The rechargeable lithium battery, as a candidate for such devices, has attracted considerable attention since the invention of the rechargeable Li-ion battery in 1985.[3] The rechargeable Li-ion battery has been in everyday use in portable electronics, such as cell phones and laptops, with one of the best energy densities, no memory effect, and the slow loss of charge.[4,5] However, in the electrification of the transportation sector, for example the electric vehicle, the specific energy and energy density for state-of-the-art Li-ion batteries are much too low for an all-electric vehicle.[6-10] The specific energy of current automobile Li-ion cells is about 150 Wh/kg at the cell level and about 105 Wh/kg at the pack level, *i.e.*, a driving range of 70 miles for a 200 kg battery pack;[11] it could be pushed up to 400 Wh/kg with the high-capacity electrode materials, leading to a driving range of 140 miles at the most, which is still much lower than the goal of 300 miles per single charge set by the United States Advanced Battery Consortium (USABC).[12] Besides the driving range, the USABC set goals for working temperature range (-40 °C to +66 °C), calendar life (15 years), and so on,[12] which are also far beyond the electrochemical properties of Li-ion batteries at the present time. Thus beyond-Li-ion-battery research is put on the front burner, in order to develop the energy storage systems with much higher specific energy and energy density,[6,7,13,14] and thereby to achieve the required level of electric vehicle.

Rechargeable Li-air battery, which was originally proposed in the 1970s as a potential high-capacity energy source,[15,16] has a high theoretical energy density

12 kWh/kg excluding the oxygen mass.[17] It has been theorized that the practical value could be 1.7 kWh/kg on the cell level.[17] Meanwhile, the theoretical energy density of gasoline is around 13 kWh/kg, and the energy provided to the wheels after losses is also 1.7 kWh/kg. According to the energy densities of various kinds of rechargeable batteries shown in Figure 1.1,[17-20] the ultrahigh energy density and the comparability with gasoline make Li-air battery a promising large-scale energy storage system.

Li-air battery induces a current flow by the oxidation of lithium at the anode and the reduction of oxygen at the cathode. In 1996, Abraham and Jiang[21] reported the first nonaqueous Li-air battery consisting of a Li-metal anode, a porous carbon cathode, and a polymer organic electrolyte. Thereafter the research did not advance until the late 2000s due to the advance in materials technology. Especially in the last 3-4 years, it has attracted increasing attention[6,11,22-30] because of the burning issues in the fields of environmental protection and energy supplies. Besides the extremely high energy density, the major benefit of the Li-air battery is the potential to utilize oxygen from air instead of storing an oxidizer internally, which is also one of the reasons for its high energy density. However, in current laboratory work, cells are performed in a pure oxygen environment, because other components in air—H_2O, CO_2, etc.—would cause the degradation of the battery.[31-33] This is the reason why the name "Li-air battery" has been replaced by "Li-O_2 battery" in many recent articles.[22,26,34-38] In spite of this, the true "Li-air battery" is still the ultimate goal.

According to the types of electrolyte, Li-O_2 battery is subdivided into four types: aprotic,[39,40] aqueous,[33,41] solid state,[42,43] and hybrid aqueous/aprotic.[44-46] Currently, most effort has focused on the aprotic Li-O_2 battery, which is actually the nonaqueous Li-air battery in many previous articles[47-49] using organic electrolytes. The reason to replace "non-aqueous" by "aprotic" is to not confuse it with solid state or protonic nonaqueous batteries. An aprotic system is the most basic system, which would favor fundamental research on mechanism and battery components. Therefore my research will focus on the aprotic Li-O_2 battery, consisting of the following aspects: fundamental mechanism, cathode catalysts, and cathode architecture.

Despite significant progress that has been achieved recently, the aprotic Li-O_2 battery is still in an embryonic stage. The electrochemical reactions and mechanism have not been understood in detail yet, and many formidable challenges prevent the viable commercial implementation. One of biggest issues facing the development of Li-O_2 batteries is the accumulation of the insoluble and nonconducting discharge product Li_2O_2 on a porous carbon cathode.[48,50-53] Such accumulation would clog the pores of the porous carbon, leading to the reduction of the electron conductivity, the blockage of the pathway for further O_2 diffusion, and somehow an increase in the charge overpotential. Therefore, understanding and controlling the formation of Li_2O_2 particles upon discharge would be the key factor in engineering air electrode structures that can provide high energy and power density of the reversible Li-O_2 cell with a long cycle life.

Meanwhile, the colossal charge overpotential presented in the current Li-O_2 system, which is likely due to the lack of effective cathode catalyst to promote the discharge and charge reactions,[54,55] significantly impacts the cell efficiency and cyclability. Various electrocatalysts on cathode have been shown to lower the overpotential[54,55] or enhance the cycle life,[23] and thus improve the electrochemical performance of the cells. However, none of the current electrocatalysts has improved all aspects of the battery performance yet. Some catalysts are even an important cause of side reactions, such as electrolyte decomposition. And the popular methods of loading electrocatalysts, such as mechanical milling, cannot control the catalyst nanoparticles and have the potential to destroy the microstructure of the substrate material, which is critical for the battery performance. Moreover, the mechanism of how these catalysts act in the cell has not been fully addressed yet. Therefore the research on the electrocatalyst is a large proportion of all of the research on the Li-O_2 battery. The stability of the aprotic electrolyte against the active species (*e.g.*, O^{2-}, O_2^{2-}, and O_2^{-}) in the electrolyte[56-59] or on the surface of lithium anode[37] is also a big concern. The undesired discharge products from the electrolyte decomposition are responsible for the high charge overpotential observed. These problems result in the fast decay of the cell. Without doubt, significant research effort is required to push this promising technology towards practical application.

In this dissertation, I will start with the literature survey to create an overview of

the aprotic Li-O_2 battery in Chapter 2. The research objectives are presented in Chapter 3, including the battery performance, cathode electrocatalysts, ether-based electrolyte, and Li-metal anode. Chapter 4 will introduce the experimental approaches, composed of three parts: the electrochemical test, catalyst preparation methods, and characterization methods. The experimental and theoretical results, focusing on the above problems, will be presented and discussed from Chapter 5 to Chapter 7. Chapter 5 is a systemic study on the evolution of Li_2O_2 morphology during the discharge-charge cycle, demonstrating that the mass transport of diffusive active species and the underlying evolving interfaces is critical to the oxygen reduction reaction (ORR) and oxygen evolution reaction (OER) in the Li-O_2 battery. The techniques of uniformly deposition with particle control, presented in Chapter 6 and 7, were applied on the catalyst loading and cathode architecture, and the resulting materials significantly improved the battery performance. Chapter 8 is the conclusion of the current work and the prospects for the further development of Li-air battery.

1.1 References

1. *What Are Greenhouse Gases?* US Department of Energy, **Retrieved 2007-09-09**.

2. *Renewable Energy... into the mainstream*, 2002.

3. Akira, Y.; Kenichi, S.; Takayuki, N. 1987; Vol. US 4668595 A.

4. Bates, J. B.; Dudney, N. J.; Neudecker, B.; Ueda, A.; Evans, C. D. *Solid State Ion.*

2000, *135*, 33.

5. Scrosati, B.; Hassoun, J.; Sun, Y.-K. *Energy Environ. Sci.* **2011**, *4*, 3287.

6. Bruce, P. G.; Freunberger, S. A.; Hardwick, L. J.; Tarascon, J.-M. *Nat. Mater.* **2012**, *11*, 19.

7. Lee, J.-S.; Kim, S. T.; Cao, R.; Choi, N.-S.; Liu, M.; Lee, K. T.; Cho, J. *Adv. Energy Mater.* **2011**, *1*, 34.

8. Lu, L.; Han, X.; Li, J.; Hua, J.; Ouyang, M. *J. Power Sources* **2013**, *226*, 272.

9. Bhatt, M. D.; Geaney, H.; Nolan, M.; O'Dwyer, C. *Phys. Chem. Chem. Phys.* **2014**, *16*, 12093.

10. Elgowainy, A.; Burnham, A.; Wang, M.; Molburg, J.; Rousseau, A. *Well-to-Wheels Energy Use and Greenhouse Gas Emissions Analysis of Plug-in Hybrid Electric Vehicles. Report No. ANL/ESD/09-2. Feb* **2009**.

11. Lu, J.; Li, L.; Park, J.-B.; Sun, Y.-K.; Wu, F.; Amine, K. *Chem. Rev.* **2014**, *114*, 5611.

12. *USABC Goals for Advanced Batteries for EVs - CY 2020 Commercialization* **2014-May-12**.

13. Bruce, P. G.; Hardwick, L. J.; Abraham, K. M. *MRS Bull.* **2011**, *36*, 506.

14. Cheng, F.; Chen, J. *Chem. Soc. Rev.* **2012**, *41*, 2172.

15. Bennion, D. N.; Littauer, E. L. *J. Electrochem. Soc.* **1976**, *123*, 1462.

16. Momyer, W. R.; Littauer, E. L. *"Energy to the 21st Century". Proceedings of the 15th Intersociety Energy Conversion Engineering Conference* **1980**, 1480.

17. Girishkumar, G.; McCloskey, B.; Luntz, A. C.; Swanson, S.; Wilcke, W. *J. Phys. Chem. Lett.* **2010**, *1*, 2193.

18. Blurton, K. F.; Sammells, A. F. *J. Power Sources* **1979**, *4*, 263.

19. Winter, M.; Brodd, R. J. *Chem. Rev.* **2004**, *104*, 4245.

20. Yang, Z.; Zhang, J.; Kintner-Meyer, M. C. W.; Lu, X.; Choi, D.; Lemmon, J. P.; Liu, J. *Chem. Rev.* **2011**, *111*, 3577.

21. Abraham, K. M.; Jiang, Z. *J. Electrochem. Soc.* **1996**, *143*, 1.

22. Chen, Y.; Freunberger, S. A.; Peng, Z.; Fontaine, O.; Bruce, P. G. *Nat. Chem.* **2013**, *5*, 489.

23. Jung, H.-G.; Hassoun, J.; Park, J.-B.; Sun, Y.-K.; Scrosati, B. *Nat. Chem.* **2012**, *4*, 579.

24. Oh, S. H.; Black, R.; Pomerantseva, E.; Lee, J.-H.; Nazar, L. F. *Nat. Chem.* **2012**, *4*, 1004.

25. Lu, J.; Cheng, L.; Lau, K. C.; Tyo, E.; Luo, X.; Wen, J.; Miller, D.; Assary, R.; Wang, H.-H.; Redfern, P.; Wu, H.; Park, J.-B.; Sun, Y.-K.; Vajda, S.; Amine, K.; Curtiss, L. A. *Nat. Commun.* **2014**, *5:4895*.

26. Lu, J.; Lei, Y.; Lau, K. C.; Luo, X.; Du, P.; Wen, J.; Assary, R. S.; Das, U.; Miller, D. J.; Elam, J. W. *Nat. Commun.* **2013**, *4:2383*.

27. Oh, D.; Qi, J.; Lu, Y.-C.; Zhang, Y.; Shao-Horn, Y.; Belcher, A. M. *Nat. Commun.* **2013**, *4:2756*.

28. Ottakam Thotiyl, M. M.; Freunberger, S. A.; Peng, Z.; Chen, Y.; Liu, Z.; Bruce, P. G. *Nat. Mater.* **2013**, *12*, 1050.

29. Armand, M.; Tarascon, J. M. *Nature* **2008**, *451*, 652.

30. Peng, Z.; Freunberger, S. A.; Chen, Y.; Bruce, P. G. *Science* **2012**, *337*, 563.

31. Lim, H.-K.; Lim, H.-D.; Park, K.-Y.; Seo, D.-H.; Gwon, H.; Hong, J.; Goddard, W. A.; Kim, H.; Kang, K. *J. Am. Chem. Soc.* **2013**, *135*, 9733.

32. He, H.; Niu, W.; Asl, N. M.; Salim, J.; Chen, R.; Kim, Y. *Electrochim. Acta* **2012**, *67*, 87.

33. Zhang, T.; Zhou, H. *Angew. Chem. Int. Ed.* **2012**, *51*, 11062.

34. Jung, H.-G.; Kim, H.-S.; Park, J.-B.; Oh, I.-H.; Hassoun, J.; Yoon, C. S.; Scrosati, B.; Sun, Y.-K. *Nano Lett.* **2012**, *12*, 4333.

35. Shui, J.-L.; Karan, N. K.; Balasubramanian, M.; Li, S.-Y.; Liu, D.-J. *J. Am. Chem. Soc.* **2012**, *134*, 16654.

36. Xu, D.; Wang, Z.-l.; Xu, J.-j.; Zhang, L.-l.; Wang, L.-m.; Zhang, X.-b. *Chem. Commun.* **2012**, *48*, 11674.

37. Assary, R. S.; Lu, J.; Du, P.; Luo , X.; Zhang, X.; Ren, Y.; Curtiss, L. A.; Amine, K. *ChemSusChem* **2013**, *6*, 51.

38. Du, P.; Lu, J.; Lau, K. C.; Luo, X.; Bareno, J.; Zhang, X.; Ren, Y.; Zhang, Z.; Curtiss, L. A.; Sun, Y.-K.; Amine, K. *Phys. Chem. Chem. Phys.* **2013**, *15*, 5572.

39. Li, F.; Zhang, T.; Zhou, H. *Energy Environ. Sci.* **2013**, *6*, 1125.

40. Lu, J.; Amine, K. *Energies* **2013**, *6*, 6016.

41. Zhang, T.; Imanishi, N.; Takeda, Y.; Yamamoto, O. *Chem. Lett.* **2011**, *40*, 668.

42. Kumar, B.; Kumar, J.; Leese, R.; Fellner, J. P.; Rodrigues, S. J.; Abraham, K. M. *J. Electrochem. Soc.* **2010**, *157*, A50.

43. Hassoun, J.; Croce, F.; Armand, M.; Scrosati, B. *Angew. Chem. Int. Ed.* **2011**, *50*, 2999.

44. Zhou, H.; Wang, Y.; Li, H.; He, P. *ChemSusChem* **2010**, *3*, 1009.

45. He, P.; Wang, Y.; Zhou, H. *J. Power Sources* **2011**, *196*, 5611.

46. Wang, Y.; He, P.; Zhou, H. *Energy Environ. Sci.* **2011**, *4*, 4994.

47. Black, R.; Adams, B.; Nazar, L. F. *Adv. Energy Mater.* **2012**, *2*, 801.

48. Peng, Z.; Freunberger, S. A.; Hardwick, L. J.; Chen, Y.; Giordani, V.; Barde, F.; Novak, P.; Graham, D.; Tarascon, J.-M.; Bruce, P. G. *Angew. Chem. Int. Ed.* **2011**, *50*, 6351.

49. Shanmukaraj, D.; Grugeon, S.; Gachot, G. g.; Laruelle, S. p.; Mathiron, D.; Tarascon, J.-M.; Armand, M. *J. Am. Chem. Soc.* **2010**, *132*, 3055.

50. Ogasawara, T.; Debart, A.; Holzapfel, M.; Novak, P.; Bruce, P. G. *J. Am. Chem. Soc.* **2006**, *128*, 1390.

51. Chan, M. K. Y.; Shirley, E. L.; Karan, N. K.; Balasubramanian, M.; Ren, Y.; Greeley, J. P.; Fister, T. T. *J. Phys. Chem. Lett.* **2011**, *2*, 2483.

52. Viswanathan, V.; Thygesen, K. S.; Hummelshoj, J. S.; Norskov, J. K.; Girishkumar, G.; McCloskey, B. D.; Luntz, A. C. *J. Chem. Phys.* **2011**, *135*, 214704.

53. Lau, K. C.; Assary, R. S.; Redfern, P. C.; Greeley, J. P.; Curtiss, L. A. *J. Phys. Chem. C* **2012**, *116*, 23890.

54. Hardwick, L. J.; Bruce, P. G. *Curr. Opin. Solid State Mater. Sci.* **2012**, *16*, 178.

55. Shao, Y.; Park, S.; Xiao, J.; Zhang, J.-G.; Wang, Y.; Liu, J. *ACS Catal.* **2012**, *2*, 844.

56. Zhang, Z. C.; Lu, J.; Assary, R. S.; Du, P.; Wang, H. H.; Sun, Y. K.; Qin, Y.; Lau, K. C.; Greeley, J.; Redfern, P. C.; Iddir, H.; Curtiss, L. A.; Amine, K. *J. Phys. Chem. C* **2011**, *115*, 25535.

57. Laino, T.; Curioni, A. *Chem. Eur. J.* **2012**, *18*, 3510.

58. Xu, W.; Hu, J.; Engelhard, M. H.; Towne, S. A.; Hardy, J. S.; Xiao, J.; Feng, J.; Hu, M. Y.; Zhang, J.; Ding, F.; Gross, M. E.; Zhang, J.-G. *J. Power Sources* **2012**, *215*, 240.

59. Bryantsev, V. S.; Uddin, J.; Giordani, V.; Walker, W.; Addison, D.; Chase, G. V. *J. Electrochem. Soc.* **2013**, *160*, A160.

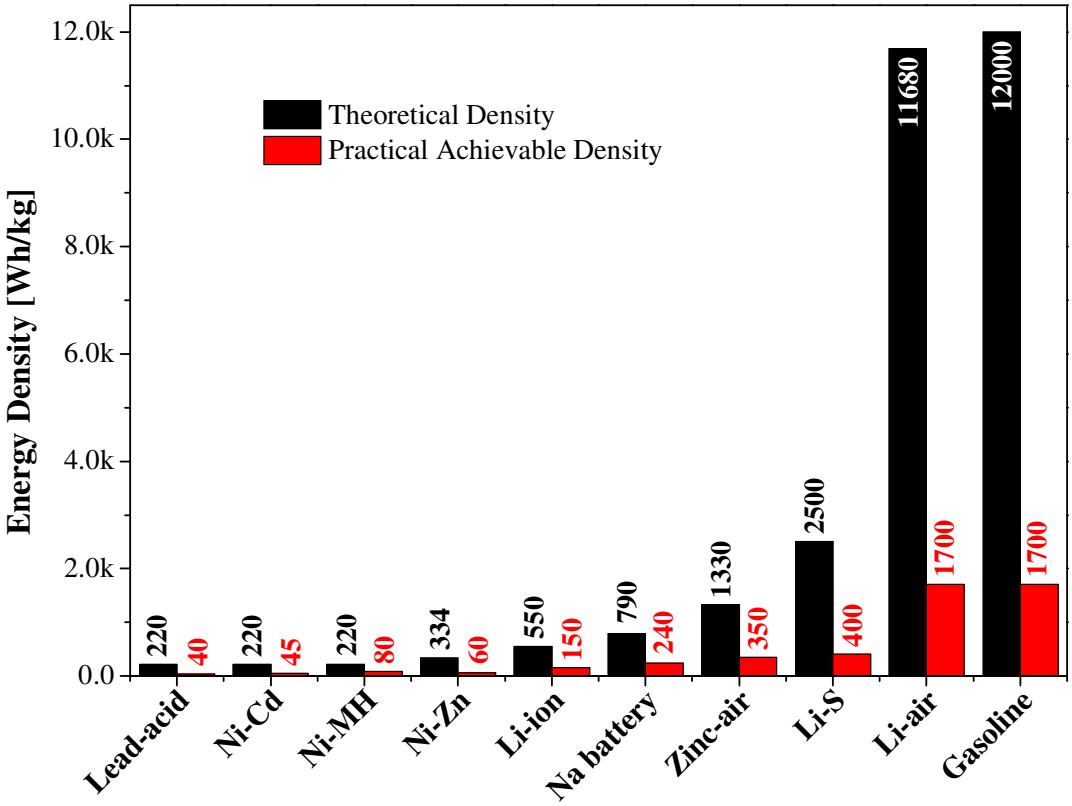

Figure 1.1: The energy densities for various batteries compared to gasoline. The theoretical density is indicated by the black bars while the practical achievable density is shown as the red bars, both with numerical values. Data from ref. 17-20.

CHAPTER 2

LITERATURE SURVEY

This chapter is a brief literature survey of the recent research on the aprotic Li-O_2 battery, including the electrochemical reactions in the battery system, the O_2-breathing cathode and efficiency electrocatalysts, the stability of the organic electrolyte and its effect on the battery performance, and the importance of a stable lithium anode.

2.1 Reactions and Mechanism

A typical aprotic Li-O_2 cell is made of a lithium metal anode, a porous cathode (usually the porous carbon), and a glass-fiber separator filled with aprotic electrolyte, as shown in Figure 2.1. It induces a current flow by the oxidation of lithium at the anode and the reduction of oxygen at the cathode, namely the oxygen reduction reaction (ORR) at the cathode during discharge. In the charge process, the oxygen evolution reaction (OER) on the cathode decomposes the discharge products.[1-6]

Without regard to the side reactions, the fundamental chemistry of an aprotic Li-O_2 battery is a Li/O_2 electrochemical couple, probably involving the reactions as

follows:

$$O_2 + Li^+ + e^- \rightarrow LiO_2 \ (E^0 = 3.0\ V\ vs.\ Li/Li^+) \quad \ldots\ldots [2.1];$$

$$O_2 + 2Li^+ + 2e^- \rightarrow Li_2O_2 \ (E^0 = 3.10\ V\ vs.\ Li/Li^+) \quad \ldots\ldots [2.2];$$

$$O_2 + 4Li^+ + 4e^- \rightarrow 2Li_2O \ (E^0 = 2.91\ V\ vs.\ Li/Li^+) \quad \ldots\ldots [2.3].$$

All the reactions above are equally dominant in thermodynamics, because they have the similar standard redox potential. In the condensed phase of Li_xO_y compounds, the two most thermodynamically stable structures are lithium oxide (Li_2O) and lithium peroxide (Li_2O_2).[7] However, reaction [2.3] is the least dominant in kinetics due to the four-electron transfer. And the irreversible discharge product Li_2O is only found when the cut-off voltage is below 2.0 V.[8-10] So reaction [2.3] cannot process, *i.e.*, Li_2O cannot be produced, under the voltage range 2.2-4.5 V in the electrochemical test of this dissertation. The reversible product Li_2O_2 was confirmed as the main discharge product by most research with the cut-off voltage > 2.0 V,[11-21] ever since the first report by Abraham and Jiang,[22] using a Raman spectroscopy and qualitative analysis. It could form directly through reaction [2.2], the two-electron transfer;[23] or be produced from LiO_2, which is unstable in the battery and forms through reaction [2.1], possibly via the following reactions:

$$2LiO_2 \rightarrow Li_2O_2 + O_2 \quad \ldots\ldots\ldots [2.4];$$

$$LiO_2 + Li^+ + e^- \rightarrow Li_2O_2 \ (E^0 = 2.96\ V\ vs.\ Li/Li^+) \quad \ldots\ldots [2.5].$$

The latter process, from reaction [2.1] to reaction [2.4] or [2.5], would be more

kinetically favored due to these one-electron transfers. And it corresponds with the discovery of the superoxide-like surface structure by both simulation[24-25] and experiments.[26-27] However, there is no direct evidence to prove which reaction predominates, or whether these reactions coexist in terms of the Li_2O_2 formation.

In OER of charge process, Li_2O_2 is decomposed to lithium cation and oxygen. The reaction could be as follows:

$$Li_2O_2 \rightarrow O_2 + 2Li^+ + 2e^- \quad \ldots\ldots \text{[2.6]};$$

$$Li_2O_2 \rightarrow LiO_2 + Li^+ + e^- \quad \ldots\ldots \text{[2.7]}.$$

Ogasawara *et al.*[28] presented the direct evidence of oxygen release on charging. Yet it is not a negation for the one-electron transfer reaction [2.7], because McClosky *et al.*[29-30] showed that the amount of O_2 evolved upon charging is only 60% of the consumption in discharge. However, the difference in the O_2 amount cannot be a strong support of reaction [2.7] either, because it might be caused by side reactions. Similar to the current knowledge of discharge reactions, it is also unclear which oxygen evolution reaction is more favorable in the charging process.

The insoluble product Li_2O_2 has been considered the principal reason for the high charge overpotential[20, 31-32] and poor cyclability[33] of the current Li-O_2 battery. Electrocatalysts are widely applied to lower the overpotential, which will be discussed in the following section, in order to improve the roundtrip efficiency of the cell. In 2011, Mitchell *et al.*[9] reported a toroid-shaped discharge product in an aprotic Li-O_2 cell using

binder-free hollow carbon fibers as the cathode material. They affirmed that the toroid is Li_2O_2, according to its morphological evolution as a function of both discharge rate and capacity. This conclusion is generally accepted by other researchers. However, there was no direct evidence until Lu *et al.*[34] reported an electron diffraction pattern on a single toroid using high-resolution transmission electron microscope (HR-TEM), confirming the presence of Li_2O_2 in the toroidal shape. Findings on the toroidal morphology of Li_2O_2 are interesting since they lead to very nonuniform surface coverage, which is beneficial to increasing the discharge capacity of the cell due to easier oxygen diffusion at the late stage of the discharge. Besides the toroidal morphologies, the discharge products are observed to form isolated Li_2O_2 islands on FGS,[10] and homogenous Li_2O_x membrane coating on porous carbon particles under high current density.[17]

Understanding the nucleation and morphology evolution of Li_2O_2 particles upon discharge is the crucial factor to improving the battery performance. Black *et al.*[26] showed that the crystallization of Li_2O_2 is governed by its rate of nucleation from LiO_2, in the absence of binder and catalyst. The morphology evolution of the discharge products is also dominated by current density in the discharge/charge process, in which toroid products appear at a low current rate and small equiaxed particles grow at a high rate.[17, 21] The nature of Li_2O_2 is a crucial point that can help to control its nucleation and evolution. The paramagnetism of Li_2O_2 formed in discharge has been detected by Lu *et al.*,[24] using electron paramagnetic resonance (EPR). This work provided direct evidence

that the spin in the Li_2O_2 comes from a superoxide-like structure, which corresponds to the density function theory (DFT) study by Lau *et al.*,[25] that a localized unpaired spin and the shorter O-O distance was found. The result is further confirmed by Yang *et al.*[27] with the 1125 cm^{-1} peak in the Raman spectra. Hummelshoj *et al.*[35] propounded a theory that the electronic band gap of bulk Li_2O_2 can be lowered from 4.9 eV to ~ 3.0 eV by inducing Li vacancies into the bulk, which is supported by the Li_2O_2 nanoparticles observed as the discharge product.[21, 36]

2.2 Cathode and Electrocatalysts

In an aprotic Li-O_2 battery, most electrochemical reactions react on the O_2-breathing cathode, which is also the place for deposition of the discharge product Li_2O_2, and for most of the voltage drop in a cell. A cathode material with the following requirements would be able to cater for the needs of high performance: (1) fast oxygen diffusion; (2) good electric conductivity; (3) good ionic conductivity; (4) high specific surface area; and (5) stable property. Porous carbon has been used as the cathode material in most Li-O_2 batteries because it shows compliance with these requirements.[10, 37-40] Other than that, porous carbon also has the advantages of low weight and the existence of defect sites, which may catalyze the oxygen reduction reactions. Read *et al.*[41] have studied the effects of porosity of various porous carbon, *i.e.*, micro-, meso-, and macro-porosities, and suggested that tailoring of the cathode can improve the battery

performance. High surface area guarantees enough active sites for reactions. However, in a comparison among several carbon materials, the highest discharge capacity appears in the cell with Super P carbon as the cathode material, which has a relatively low surface area (62 m^2/g).[42] It has been realized that the pore size in the range of 2-50 nm, not specific surface area, is the primary factor of the capacity when using porous carbon as the cathode material.[43] Younesi *et al.*[44] revealed that overmuch binder in cathode slurry would also clog the pores and lead to a sharp decline in the battery capacity.

Commercial carbon black, such as Super P,[42] Acetylene,[45] Ketjen black,[46] and Graphitized carbon black,[34] is the most widely-applied porous carbon in current research on the aprotic Li-O_2 battery, to achieve high battery capacity and high energy density. Recent research also demonstrates various new carbon-based materials. Mitchell *et al.*[9] reported a high discharge capacity of 7200 mAh/g using hollow carbon fibers directly growing on a ceramic porous substrate as the cathode, in which the Li_2O_2 toroid was first reported. They also used carbon nanotube (CNT) cathode in the research of the morphological evolution of Li_2O_2 toroid.[21] Xiao *et al.*[10] reported a hierarchically porous functionalized graphene sheets (FGS) cathode delivering an extremely high capacity of 15000 mAh/g. Despite achieving the high capacity, the big hurdle of Li-O_2 battery, large overpotential, still exists even at very low current density, causing low round-trip efficiencies (< 60%).

Overpotential is the difference between the thermodynamically determined

reduction potential of a half-reaction and the observed potential at which the redox event occurred. As mentioned in section 2.1, all the possible ideal reactions in an aprotic Li-O_2 battery have a similar standard redox potential around 3.0 V, which is the thermodynamically determined reduction potential. Experimentally, it is a surprise to have a discharge voltage plateau in the range of 2.6-2.7 V for different cathodes, no matter whether catalyst is loaded or not. It suggests that the reaction kinetics of ORR is not by the catalyst, but probably by the oxygen diffusion rate. This conjecture is supported by the reports that an increase in the oxygen pressure, which enhances the diffusivity in the cathode, would lead to a higher specific capacity.[47] In the charge process, the voltage plateau is above 4.0 V for most bare carbon cathodes. The high overpotential requires extra energy to drive the reactions, thus causing a low round-trip efficiency of the battery. And the electrolytes at present are unstable under such a high voltage, which is behind the bad performance of the battery. Various catalysts[48] have been examined to lower the charge overpotential, and to improve the capacity and cyclability of battery.

Cobalt pthalocyanine-catalyzed porous carbon was used in the first Li-O_2 battery.[22] Since then, many new catalysts have been reported, including metal oxides,[49-53] precious metals,[54-56] and mixed-metal oxides.[57-63] In 2006, the Bruce group[28] used electrolytic manganese dioxide (MnO_2) as the catalyst and significantly improved the cyclability to more than 30 cycles. They also evaluated the effects of other metal-oxide

catalysts to the battery performance in follow-up work,[64] and found that Fe_2O_3 cell has the highest initial capacity but the worst cyclability, the cells with catalysts Fe_3O_4, CuO, or $CoFe_2O_4$ have excellent capacity retention, and Co_3O_4 improves the cell performance in both initial capacity and capacity retention. MnO_2 is so far the most widely studied catalyst, because it is easy to synthesize under control with high purity, and has a wide variety of crystallographic structures (*e.g.*, α,[65-69] β,[70-73] γ,[74-75] and δ forms[76]) among which the single α-MnO_2 nanotubes have the best catalysis and present a much better performance than other forms of MnO_2 catalysts. Precious metals, such as Au and Pt, were reported as efficiency catalysts in carbonate-based electrolytes,[56] but did not perform well in ether-based electrolytes.[77] The effects and importance of electrolytes will be introduced in section 2.3.

Earlier research concluded that catalysts would reduce the reduction activation energy, which has been confirmed by many catalysts such as metals and metal oxides. Black *et al.*[18] presumed that their catalyst, Co_3O_4/rGO, reduces the binding energy of Li_xO_2 species and acts as a promoter to enhance their mass transport, instead of lowering the activation energy like conventional electrocatalysts. This finding would help to better understand surface reactivity and tailor electrodes to overcome the limitations.

Various details are still unclear in the mechanism of the catalysis. The structure and distribution of a catalyst has been deemed to influence the porosity of cathode material and thereby determine the specific capacity and energy density of the cells. A

uniformly distributed catalyst is generally considered to improve the battery performance. However, according to the a drift-diffusion-based model reported by Andrei *et al.*,[78] the uniform distribution catalysts only improve the current and power density, while the nonuniform catalyst is more efficient in enhancing the reaction rate at the separator-cathode interface. This theory has not been validated because of the lack of the deposition technique to build a controlled nonuniform distribution of catalyst nanoparticles.

2.3 Aprotic Electrolyte

In an aprotic Li-O_2 battery, electrolyte formulation has been found to be an important influence on battery performance. The bad stability of the electrolyte is one of the key factors causing the poor performance of aprotic Li-O_2 battery. Organic carbonate based electrolytes, such as propylene carbonate (PC),[79-86] ethylene carbonate (EC),[87-93] and dimethyl carbonate (DMC),[94-97] were widely applied in early investigation of aprotic Li-O_2 battery, because of their advantages of wide electrochemical window and wide liquid-temperature range, which make them the main electrolytes in Li-ion batteries. But they are not stable in a Li-O_2 battery due to the presence of reactive radicals (O_2^-, O_2^{2-} *et al.*). Preceding the first report of the Li-O_2 battery in 1996,[22] it has been reported since 1989 that PC would decompose in oxygen reduction,[98-99] but made little impression until the coming of direct evidence in 2010. Instead of Li_2O_2, the main discharge products are lithium carbonate (Li_2CO_3), lithium formate (HCO_2Li), and lithium acetate (CH_3CO_2Li)

in a Li-O_2 battery using organic carbonates as the electrolyte solvent.[100-106] These carbonate compounds decompose in charge process and produce CO_2, causing the high charge overpotential and furthermore leading to bad cyclability of the cell. DFT studies show that PC could easily decompose on Li_2O_2 [100] surface,[81] and the reaction with O_2^- is the major hurdle of electrolyte stability.[102] PC is easily impacted by the nucleophilic attack of oxygen reduced species O_2^-. Once the ring of PC is open, the subsequent C-O bond breaking, *i.e.*, the decomposition, is easier and thermodynamically favored.[101] Therefore the carbonate-based electrolyte is no longer the mainstream in the aprotic Li-O_2 battery. Conclusions drawn from the investigations in the cells using carbonate-based electrolytes should be re-examined in other stable and efficient electrolytes. In some research, EC is mixed with a linear organic carbonate (*e.g.*, DMC, DEC) to approach a better cell performance.[16, 87-90, 95-97, 107-111] This method also comes from the Li-ion battery, in which a stable solid-electrolyte interface (SEI) is formed in the mixed-solvent electrolyte, enhancing the cyclability and safety of the battery. However, due to the presence of O_2 in Li-O_2 battery, side reactions would be more complex, and are still subjects to be investigated.

After a broad search,[8, 23, 101-104, 112-113] ether-based solvents gain their popularity due to high stability, high oxidation potentials, low viscosity, inflammability, and low cost. They were firstly reported by Read in 2006,[114] with improved stability and battery performance. And plenty of articles have confirmed that the main discharge product is

Li_2O_2 when using ether-based electrolyte, such as 1,2-dimethoxyethane (DME),[115-116] tetraethylene glycol dimethyl ether (TEGDME),[17, 117-121] and tri(ethylene glycol)-substituted methyltrimethyl silane (1NM3);[24, 101, 122] although DME has the possibility of degradation due to the presence of O_2^- or O_2^{2-} according to DFT study.[113] The long-chain ether TEGDME is stable against O_2^- and Li metal,[26] and has less polarity and volatility. By using the TEGDME electrolyte, the cell reported by Jung *et al.*[123] has a specific capacity of 1000 mAh/g with up to 100 cycles, under both low and high current rates, which is an amazingly stable performance at the current stage of research. 1NM3 is a silicon-containing oligo solvent with a low glass transition temperature, high oxidation potential, and good lithium ion conductivity.[101] It results in a low charge voltage (3.5 V vs. Li/Li^+), but a bad cyclability. Freunberger *et al.*[124] investigated other linear or cyclic ether-based electrolytes, but found that decomposition occurs, producing a mixture of Li_2CO_3, HCO_2Li, CH_3CO_2Li, $C_2H_4(OCO_2Li)_2$, CO_2, or H_2O.

Besides solvent, the lithium salt in the aprotic electrolyte is also an important source of side reactions. In most early-stage investigations, the salt is lithium hexafluorophosphate ($LiPF_6$) because it is widely used in Li-ion batteries.[125-126] $LiPF_6$ is stable against cathode, and has high conductivity and low internal resistance. But it is extremely sensitive to H_2O, and its decomposition has been found with the formation of HF and LiF. Du *et al.*[122] reported the decomposition of 1NM3 solvent triggered by the formation of HF from the decomposition of $LiPF_6$, which leads to degradation of the

electrolyte and cause bad battery performance. In Freunberger's investigation mentioned above,[124] the usage of $LiPF_6$ should take the blame for their conclusion that ether-based electrolytes are not suitable for Li-O_2 battery. However, Du *et al.*[122] also demonstrated that $LiPF_6$ is more stable in TEGDME than in 1NM3, and the similar side reactions are not observed when LiTFSI and $LiCF_3SO_3$ [127] are used as the salt. The usage of $LiCF_3SO_3$ in the research of Jung *et al.*[123] contributes to the significant improvement of the cell performance as mentioned above. These results suggest that the electrolyte stability in Li-O_2 batteries depends on the stability of lithium salts and the compatibility of lithium salts with solvent.

2.4 Anode

Reversible charge storage in the anode is accomplished by depositing and dissolving Li^+ from the Lithium metal. Li metal is a theoretically ideal anode material for battery to provide extraordinarily high energy density, because of its great electrochemical potential and largest specific energy (3860 mAh/g) among the metallic elements. However, the unwanted dendrite formation on the anode has been discovered in Li-ion batteries since the mid-1980s.[128-130] These growth particles penetrate the separator and cause an electrical short. Thus it becomes the longstanding problem, impeding the development of the secondary Li-ion batteries with long cycle life. In the Li-O_2 battery, dendrite is not as influential as the problems created by cathode and electrolyte, since it

has not been reported so far. Indeed, reactions occurring on the interface between Li metal and electrolyte are the most serious problems on the anode. The anode failure in Li-ion battery has been shown by Aurbach *et al.*[130] and Zhuang *et al.*[131] due to the decomposition of the carbonate-based electrolyte, producing lithium methoxide (CH_3OLi), methyllithium (CH_3Li), and polymeric layers. Assary *et al.*[132-133] presented the decomposition of ether-based electrolytes in Li-O_2 battery, indicating that crossover of O_2 from the cathode to the anode results in different decomposition reactions at the Li-anode than in a Li-ion battery. To reduce the failure, there have been several suggestions for developing the anode. For example, alloying Li with other elements (*e.g.*, Mg) may raise the surface energy and reduce morphology changes, and an efficient protective layer on the anode could avoid the active species from the decomposition of electrolyte. Truong *et al.*[134] fabricated single-crystal silicon membranes to eliminate the O_2 crossover, but the Li^+ conductivity of the membrane is too low. More research is needed to improve the anode material.

2.5 References

1. Black, R.; Adams, B.; Nazar, L. F. *Adv. Energy Mater.* **2012,** *2*, 801-815.

2. Bruce, P. G.; Freunberger, S. A.; Hardwick, L. J.; Tarascon, J.-M. *Nat. Mater.* **2012,** *11*, 19-29.

3. Bruce, P. G.; Hardwick, L. J.; Abraham, K. M. *MRS Bull.* **2011,** *36*, 506-512.

4. Christensen, J.; Albertus, P.; Sanchez-Carrera, R. S.; Lohmann, T.; Kozinsky, B.; Liedtke, R.; Ahmed, J.; Kojic, A. *J. Electrochem. Soc.* **2012,** *159*, R1-R30.

5. Girishkumar, G.; McCloskey, B.; Luntz, A. C.; Swanson, S.; Wilcke, W. *J. Phys. Chem. Lett.* **2010,** *1*, 2193-2203.

6. Lu, J.; Li, L.; Park, J.-B.; Sun, Y.-K.; Wu, F.; Amine, K. *Chem. Rev.* **2014,** *114*, 5611-5640.

7. Lau, K. C.; Curtiss, L. A.; Greeley, J. *J. Phys. Chem. C* **2011,** *115*, 23625-23633.

8. Laoire, C. O.; Mukerjee, S.; Plichta, E. J.; Hendrickson, M. A.; Abraham, K. M. *J. Electrochem. Soc.* **2011,** *158*, A302-A308.

9. Mitchell, R. R.; Gallant, B. M.; Thompson, C. V.; Shao-Horn, Y. *Energy Environ. Sci.* **2011,** *4*, 2952-2958.

10. Xiao, J.; Mei, D.; Li, X.; Xu, W.; Wang, D.; Graff, G. L.; Bennett, W. D.; Nie, Z.; Saraf, L. V.; Aksay, I. A.; Liu, J.; Zhang, J.-G. *Nano Lett.* **2011,** *11*, 5071-5078.

11. Gallant, B. M.; Mitchell, R. R.; Kwabi, D. G.; Zhou, J.; Zuin, L.; Thompson, C. V.; Shao-Horn, Y. *J. Phys. Chem. C* **2012,** *116*, 20800-20805.

12. Harding, J. R.; Lu, Y.-C.; Tsukada, Y.; Shao-Horn, Y. *Phys. Chem. Chem. Phys.* **2012,** *14*, 10540-10546.

13. Fan, W.; Cui, Z.; Guo, X. *J. Phys. Chem. C* **2013,** *117* (6), 2623-2627.

14. Jung, H.-G.; Kim, H.-S.; Park, J.-B.; Oh, I.-H.; Hassoun, J.; Yoon, C. S.; Scrosati, B.; Sun, Y.-K. *Nano Lett.* **2012,** *12*, 4333-4335.

15. Kang, J.; Jung, Y. S.; Wei, S.-H.; Dillon, A. C. *Phys. Rev. B* **2012,** *85*, 035210.

16. Nanda, J.; Biheux, H.; Voisin, S.; Veith, G. M.; Archibald, R.; Walker, L.; Allu, S.; Dudney, N. J.; Pannala, S. *J. Phys. Chem. C* **2012,** *116*, 8401-8408.

17. Adams, B. D.; Radtke, C.; Black, R.; Trudeau, M. L.; Zaghib, K.; Nazar, L. F. *Energy Environ. Sci.* **2013,** *6*, 1772-1778.

18. Black, R.; Lee, J.-H.; Adams, B.; Mims, C. A.; Nazar, L. F. *Angew. Chem. Int. Ed.* **2013,** *52*, 392-396.

19. Liu, X. H.; Liu, Y.; Kushima, A.; Zhang, S.; Zhu, T.; Li, J.; Huang, J. Y. *Adv. Energy Mater.* **2012,** *2*, 722-741.

20. Luntz, A. C.; Viswanathan, V.; Voss, J.; Varley, J. B.; Nørskov, J. K.; Scheffler, R.; Speidel, A. *J. Phys. Chem. Lett.* **2013,** *4*, 3494-3499.

21. Mitchell, R. R.; Gallant, B. M.; Shao-Horn, Y.; Thompson, C. V. *J. Phys. Chem. Lett.* **2013,** *4*, 1060-1064.

22. Abraham, K. M.; Jiang, Z. *J. Electrochem. Soc.* **1996,** *143*, 1-5.

23. Peng, Z.; Freunberger, S. A.; Chen, Y.; Bruce, P. G. *Science* **2012,** *337*, 563-566.

24. Lu, J.; Jung, H.-J.; Lau, K. C.; Zhang, Z.; Schlueter, J. A.; Du, P.; Assary, R. S.; Greeley, J.; Ferguson, G. A.; Wang, H.-H.; Hassoun, J.; Iddir, H.; Zhou, J.; Zuin, L.; Hu, Y.; Sun, Y.-K.; Scrosati, B.; Curtiss, L. A.; Amine, K. *ChemSusChem* **2013,** *6*, 1196-1202.

25. Lau, K. C.; Assary, R. S.; Redfern, P. C.; Greeley, J. P.; Curtiss, L. A. *J. Phys. Chem. C* **2012,** *116*, 23890-23896.

26. Black, R.; Oh, S. H.; Lee, J.-H.; Yim, T.; Adams, B.; Nazar, L. F. *J. Am. Chem. Soc.* **2012,** *134*, 2902-2905.

27. Yang, J.; Zhai, D.; Wang, H.-H.; Lau, K. C.; Schlueter, J. A.; Du, P.; Myers, D. J.; Sun, Y.-K.; Curtiss, L. A.; Amine, K. *Phys. Chem. Chem. Phys.* **2013,** *15*, 3764-3771.

28. Ogasawara, T.; Debart, A.; Holzapfel, M.; Novak, P.; Bruce, P. G. *J. Am. Chem. Soc.* **2006,** *128*, 1390-1393.

29. McCloskey, B. D.; Valery, A.; Luntz, A. C.; Gowda, S. R.; Wallraff, G. M.; Garcia, J. M.; Mori, T.; Krupp, L. E. *J. Phys. Chem. Lett.* **2013,** *4*, 2989-2993.

30. McCloskey, B. D.; Speidel, A.; Scheffler, R.; Miller, D. C.; Viswanathan, V.; Hummelshoj, J. S.; Norskov, J. K.; Luntz, A. C. *J. Phys. Chem. Lett.* **2012,** *3*, 997-1001.

31. Yao, K. P. C.; Kwabi, D. G.; Quinlan, R. A.; Mansour, A. N.; Grimaud, A.; Lee, Y.-L.; Lu, Y.-C.; Shao-Horn, Y. *J. Electrochem. Soc.* **2013,** *160*, A824-A831.

32. Younesi, R.; Hahlin, M.; Bjorefors, F.; Johansson, P.; Edstrom, K. *Chem. Mater.* **2013,** *25*, 77-84.

33. Viswanathan, V.; Thygesen, K. S.; Hummelshoj, J. S.; Norskov, J. K.; Girishkumar, G.; McCloskey, B. D.; Luntz, A. C. *J. Chem. Phys.* **2011,** *135*, 214704.

34. Lu, J.; Lei, Y.; Lau, K. C.; Luo, X.; Du, P.; Wen, J.; Assary, R. S.; Das, U.; Miller, D. J.; Elam, J. W. *Nat. Commun.* **2013,** *4:2383*.

35. Hummelshøj, J. S.; Luntz, A. C.; Nørskov, J. K. *J. Chem. Phys.* **2013,** *138*, 034703.

36. Gallant, B. M.; Kwabi, D. G.; Mitchell, R. R.; Zhou, J.; Thompson, C. V.; Shao-Horn, Y. *Energy Environ. Sci.* **2013,** *6*, 2518-2528.

37. Mirzaeian, M.; Hall, P. J.; Ieee, *Nano Structure Carbons for Energy Storage in Lithium Oxygen Batteries*. 2009; p 1694-1703.

38. Williford, R. E.; Zhang, J.-G. *J. Power Sources* **2009,** *194*, 1164-1170.

39. Hayashi, M.; Minowa, H.; Takahashi, M.; Shodai, T. *Electrochemistry* **2010,** *78*, 325-328.

40. Ottakam Thotiyl, M. M.; Freunberger, S. A.; Peng, Z.; Bruce, P. G. *J. Am. Chem. Soc.* **2012,** *135*, 494-500.

41. Read, J. *J. Electrochem. Soc.* **2002,** *149*, A1190-A1195.

42. Cheng, H.; Scott, K. *Appl. Catal. B* **2011,** *108*, 140-151.

43. Yang, X.-H.; He, P.; Xia, Y.-Y. *Electrochem. Commun.* **2009,** *11*, 1127-1130.

44. Younesi, S. R.; Urbonaite, S.; Bjorefors, F.; Edstrom, K. *J. Power Sources* **2011,** *196*, 9835-9838.

45. Zeng, J.; Nair, J. R.; Chen, Q.; Francia, C.; Bodoardo, S.; Penazzi, N. *ChemElectroChem* **2014**, DOI: 10.1002/celc.201402028.

46. Zhang, J.-G.; Wang, D.; Xu, W.; Xiao, J.; Williford, R. E. *J. Power Sources* **2010,** *195*, 4332-4337.

47. Yang, X.-H.; Xia, Y.-Y. *J. Solid State Electrochem.* **2010,** *14*, 109-114.

48. Shao, Y.; Park, S.; Xiao, J.; Zhang, J.-G.; Wang, Y.; Liu, J. *ACS Catal.* **2012,** *2*, 844-857.

49. Truong, T. T.; Liu, Y.; Ren, Y.; Trahey, L.; Sun, Y. *ACS Nano* **2012,** *6*, 8067-8077.

50. Su, X.; Yu, C.; Qiang, C. *Appl. Surf. Sci.* **2011,** *257*, 9014-9018.

51. Kim, K. S.; Park, Y. J. *Nanoscale Res. Lett.* **2012,** *7*, 47.

52. Sun, B.; Liu, H.; Munroe, P.; Ahn, H.; Wang, G. *Nano Res.* **2012,** *5*, 460-469.

53. Lu, J.; Qin, Y.; Du, P.; Luo, X.; Wu, T.; Ren, Y.; Wen, J.; Miller, D. J.; Miller, J. T.; Amine, K. *RSC Adv.* **2013,** *3*, 8276-8285.

54. Chen, Z.; Waje, M.; Li, W.; Yan, Y. *Angew. Chem. Int. Ed.* **2007,** *46*, 4060-4063.

55. Dutta, I.; Carpenter, M. K.; Balogh, M. P.; Ziegelbauer, J. M.; Moylan, T. E.; Atwan, M. H.; Irish, N. P. *J. Phys. Chem. C* **2010,** *114*, 16309-16320.

56. Lu, Y.-C.; Xu, Z.; Gasteiger, H. A.; Chen, S.; Hamad-Schifferli, K.; Shao-Horn, Y. *J. Am. Chem. Soc.* **2010,** *132*, 12170-12171.

57. Fu, Z.; Lin, X.; Huang, T.; Yu, A. *J. Solid State Electrochem.* **2012,** *16*, 1447-1452.

58. Lee, J.-H.; Black, R.; Popov, G.; Pomerantseva, E.; Nan, F.; Botton, G. A.; Nazar, L. F. *Energy Environ. Sci.* **2012,** *5*, 9558-9565.

59. Wang, H.; Yang, Y.; Liang, Y.; Zheng, G.; Li, Y.; Cui, Y.; Dai, H. *Energy Environ. Sci.* **2012,** *5*, 7931-7935.

60. Hung, T.-F.; Mohamed, S. G.; Shen, C.-C.; Tsai, Y.-Q.; Chang, W. S.; Liu, R.-S. *Nanoscale* **2013,** *5*, 12115-12119.

61. Xu, J.-J.; Xu, D.; Wang, Z.-L.; Wang, H.-G.; Zhang, L.-L.; Zhang, X.-B. *Angew.*

Chem. Int. Ed. **2013,** *52*, 3887-3890.

62. Zhang, L.; Zhang, S.; Zhang, K.; Xu, G.; He, X.; Dong, S.; Liu, Z.; Huang, C.; Gu, L.; Cui, G. *Chem. Commun.* **2013,** *49*, 3540-3542.

63. Zhang, G. Q.; Hendrickson, M.; Plichta, E. J.; Au, M.; Zheng, J. P. *J. Electrochem. Soc.* **2012,** *159*, A310-A314.

64. Debart, A.; Bao, J.; Armstrong, G.; Bruce, P. G. *J. Power Sources* **2007,** *174*, 1177-1182.

65. Benbow, E. M.; Kelly, S. P.; Zhao, L.; Reutenauer, J. W.; Suib, S. L. *J. Phys. Chem. C* **2011,** *115*, 22009-22017.

66. Cao, Y.; Wei, Z.; He, J.; Zang, J.; Zhang, Q.; Zheng, M.; Dong, Q. *Energy Environ. Sci.* **2012,** *5*, 9765-9768.

67. Debart, A.; Paterson, A. J.; Bao, J.; Bruce, P. G. *Angew. Chem. Int. Ed.* **2008,** *47*, 4521-4524.

68. Ling, C.; Mizuno, F. *Chem. Mater.* **2012,** *24*, 3943–3951.

69. Zhang, G. Q.; Zheng, J. P.; Liang, R.; Zhang, C.; Wang, B.; Au, M.; Hendrickson, M.; Plichta, E. J. *J. Electrochem. Soc.* **2011,** *158*, A822-A827.

70. Jiao, F.; Bruce, P. G. *Adv. Mater.* **2007,** *19*, 657-660.

71. Mellan, T. A.; Maenetja, K.; Ngoepe, P.; Woodley, S. M.; Catlow, C. R. A.; Grau-Crespo, R. *J. Mater. Chem. A* **2013,** *1*, 14879-14887.

72. Thapa, A. K.; Hidaka, Y.; Hagiwara, H.; Ida, S.; Ishihara, T. *J. Electrochem. Soc.* **2011,** *158*, A1483-A1489.

73. Tompsett, D. A.; Parker, S. C.; Bruce, P. G.; Islam, M. S. *Chem. Mater.* **2013,** *25*, 536-541.

74. Jin, L.; Xu, L.; Morein, C.; Chen, C.-H.; Lai, M.; Dharmarathna, S.; Dobley, A.; Suib, S. L. *Adv. Funct. Mater.* **2010,** *20*, 3373-3382.

75. Zhang, L.; Zhang, X.; Wang, Z.; Xu, J.; Xu, D.; Wang, L. *Chem. Commun.* **2012,** *48*, 7598-7600.

76. Liu, S.; Zhu, Y.; Xie, J.; Huo, Y.; Yang, H. Y.; Zhu, T.; Cao, G.; Zhao, X.; Zhang, S. *Adv. Energy Mater.* **2014**, DOI: 10.1002/aenm.201301960.

77. McCloskey, B. D.; Scheffler, R.; Speidel, A.; Bethune, D. S.; Shelby, R. M.; Luntz, A. C. *J. Am. Chem. Soc.* **2011,** *133*, 18038-18041.

78. Andrei, P.; Zheng, J. P.; Hendrickson, M.; Plichta, E. J. *J. Electrochem. Soc.* **2010,** *157*, A1287-A1295.

79. Allen, C. J.; Hwang, J.; Kautz, R.; Mukerjee, S.; Plichta, E. J.; Hendrickson, M. A.; Abraham, K. M. *J. Phys. Chem. C* **2012,** *116*, 20755–20764.

80. Herranz, J.; Garsuch, A.; Gasteiger, H. A. *J. Phys. Chem. C* **2012,** *116*, 19084-19094.

81. Laino, T.; Curioni, A. *Chem. Eur. J.* **2012,** *18*, 3510-3520.

82. Mirzaeian, M.; Hall, P. J.; Sillars, F. B.; Fletcher, I.; Goldin, M. M.; Shitta-Bey, G. O. *J. Electrochem. Soc.* **2013,** *160*, A25-A30.

83. Shitta-Bey, G. O.; Mirzaeian, M.; Halla, P. J. *J. Electrochem. Soc.* **2012,** *159*, A315-A320.

84. Sun, B.; Wang, B.; Su, D.; Xiao, L.; Ahn, H.; Wang, G. *Carbon* **2012,** *50*, 727-733.

85. Younesi, R.; Urbonaite, S.; Edström, K.; Hahlin, M. *J. Phys. Chem. C* **2012,** *116*, 20673–20680.

86. Yuasa, M.; Matsuyoshi, T.; Kida, T. *J. Power Sources* **2013,** *242*, 216-221.

87. Yoo, E.; Nakamura, J.; Zhou, H. *Energy Environ. Sci.* **2012,** *5*, 6928-6932.

88. Yang, Y.; Shi, M.; Zhou, Q.-F.; Li, Y.-S.; Fu, Z.-W. *Electrochem. Commun.* **2012,** *20*, 11-14.

89. Leskes, M.; Drewett, N. E.; Hardwick, L. J.; Bruce, P. G.; Goward, G. R.; Grey, C. P. *Angew. Chem. Int. Ed.* **2012,** *51*, 8560-8563.

90. Ke, F.-S.; Solomon, B. C.; Ma, S.-G.; Zhou, X.-D. *Electrochim. Acta* **2012,** *85*, 444-449.

91. Li, Y.; Huang, Z.; Huang, K.; Carnahan, D. L.; Xing, Y. *Energy Environ. Sci.* **2013,** *6*, 3339-3345.

92. Lu, Y.-C.; Crumlin, E. J.; Veith, G. M.; Harding, J. R.; Mutoro, E.; Baggetto, L.; Dudney, N. J.; Liu, Z.; Shao-Horn, Y. *Sci. Rep.* **2012,** *2*, 715.

93. Gao, Y.; Wang, C.; Pu, W.; Liu, Z.; Deng, C.; Zhang, P.; Mao, Z. *Int. J. Hydrogen Energy* **2012,** *37*, 12725-12730.

94. He, H.; Niu, W.; Asl, N. M.; Salim, J.; Chen, R.; Kim, Y. *Electrochim. Acta* **2012,** *67*, 87-94.

95. Lee, S. W.; Gallant, B. M.; Lee, Y.; Yoshida, N.; Kim, D. Y.; Yamada, Y.; Noda, S.; Yamada, A.; Shao-Horn, Y. *Energy Environ. Sci.* **2012,** *5*, 5437-5444.

96. Yin, J.; Fang, B.; Luo, J.; Wanjala, B.; Mott, D.; Loukrakpam, R.; Ng, M. S.; Li, Z.; Hong, J.; Whittingham, M. S.; Zhong, C.-J. *Nanotechnology* **2012,** *23*, 305404.

97. Zhamu, A.; Chen, G.; Liu, C.; Neff, D.; Fang, Q.; Yu, Z.; Xiong, W.; Wang, Y.; Wang, X.; Jang, B. Z. *Energy Environ. Sci.* **2012,** *5*, 5701-5707.

98. Aurbach, D.; Gofer, Y.; Langzam, J. *J. Electrochem. Soc.* **1989,** *136*, 3198-3205.

99. Aurbach, D.; Daroux, M.; Faguy, P.; Yeager, E. *J. Electroanal. Chem.* **1991,** *297*, 225-244.

100. Mizuno, F.; Nakanishi, S.; Kotani, Y.; Yokoishi, S.; Iba, H. *Electrochemistry* **2010,** *78*, 403-405.

101. Zhang, Z. C.; Lu, J.; Assary, R. S.; Du, P.; Wang, H. H.; Sun, Y. K.; Qin, Y.; Lau, K. C.; Greeley, J.; Redfern, P. C.; Iddir, H.; Curtiss, L. A.; Amine, K. *J. Phys. Chem. C* **2011,** *115*, 25535-25542.

102. Bryantsev, V. S.; Blanco, M. *J. Phys. Chem. Lett.* **2011,** *2*, 379-383.

103. Bryantsev, V. S.; Giordani, V.; Walker, W.; Blanco, M.; Zecevic, S.; Sasaki, K.;

Uddin, J.; Addison, D.; Chase, G. V. *J. Phys. Chem. A* **2011,** *115*, 12399-12409.

104. McCloskey, B. D.; Bethune, D. S.; Shelby, R. M.; Girishkumar, G.; Luntz, A. C. *J. Phys. Chem. Lett.* **2011,** *2*, 1161-1166.

105. Xu, W.; Viswanathan, V. V.; Wang, D.; Towne, S. A.; Xiao, J.; Nie, Z.; Hu, D.; Zhang, J.-G. *J. Power Sources* **2011,** *196*, 3894-3899.

106. Xu, W.; Xu, K.; Viswanathan, V. V.; Towne, S. A.; Hardy, J. S.; Xiao, J.; Hu, D.; Wang, D.; Zhang, J.-G. *J. Power Sources* **2011,** *196*, 9631-9639.

107. Garsuch, A.; Badine, D. M.; Leitner, K.; Gasparotto, L. H. S.; Borisenko, N.; Endres, F.; Vracar, M.; Janek, J.; Oesten, R. *Z. Phys. Chem.* **2012,** *226*, 107-119.

108. Huff, L. A.; Rapp, J. L.; Zhu, L.; Gewirth, A. A. *J. Power Sources* **2013,** *235*, 87-94.

109. Thapa, A. K.; Shin, T. H.; Ida, S.; Sumanasekera, G. U.; Sunkara, M. K.; Ishihara, T. *J. Power Sources* **2012,** *220*, 211-216.

110. Wang, H.; Xie, K. *Electrochim. Acta* **2012,** *64*, 29-34.

111. Wang, L.; Ara, M.; Wadumesthrige, K.; Salley, S.; Ng, K. Y. S. *J. Power Sources* **2013,** *234*, 8-15.

112. Assary, R. S.; Curtiss, L. A.; Redfern, P. C.; Zhang, Z.; Amine, K. *J. Phys. Chem. C* **2011,** *115*, 12216-12223.

113. Assary, R. S.; Lau, K. C.; Amine, K.; Sun, Y.-K.; Curtiss, L. A. *J. Phys. Chem. C* **2013,** *117*, 8041-8049.

114. Read, J. *J. Electrochem. Soc.* **2006,** *153*, A96-A100.

115. Crowther, O.; Keeny, D.; Moureau, D. M.; Meyer, B.; Salomon, M.; Hendrickson, M. *J. Power Sources* **2012,** *202*, 347-351.

116. Ren, X.; Wu, Y. *J. Am. Chem. Soc.* **2013,** *135*, 2923-2926.

117. Barile, C. J.; Gewirth, A. A. *J. Electrochem. Soc.* **2013,** *160*, A549-A552.

118. Cecchetto, L.; Salomon, M.; Scrosati, B.; Croce, F. *J. Power Sources* **2012,** *213*, 233-238.

119. Elia, G. A.; Park, J.-B.; Scrosati, B.; Sun, Y.-K.; Hassoun, J. *Electrochem. Commun.* **2013,** *34*, 250-253.

120. Guo, Z.; Zhou, D.; Dong, X.; Qiu, Z.; Wang, Y.; Xia, Y. *Adv. Mater.* **2013,** *25*, 5668-5672.

121. Hassoun, J.; Jung, H.-G.; Lee, D.-J.; Park, J.-B.; Amine, K.; Sun, Y.-K.; Scrosati, B. *Nano Lett.* **2012,** *12*, 5775-5779.

122. Du, P.; Lu, J.; Lau, K. C.; Luo, X.; Bareno, J.; Zhang, X.; Ren, Y.; Zhang, Z.; Curtiss, L. A.; Sun, Y.-K.; Amine, K. *Phys. Chem. Chem. Phys.* **2013,** *15*, 5572-5581.

123. Jung, H.-G.; Hassoun, J.; Park, J.-B.; Sun, Y.-K.; Scrosati, B. *Nat. Chem.* **2012,** *4*, 579-585.

124. Freunberger, S. A.; Chen, Y.; Drewett, N. E.; Hardwick, L. J.; Barde, F.; Bruce, P. G. *Angew. Chem. Int. Ed.* **2011,** *50*, 8609-8613.

125. Aurbach, D.; Markovsky, B.; Rodkin, A.; Cojocaru, M.; Levi, E.; Kim, H. J. *Electrochim. Acta* **2002,** *47*, 1899-1911.

126. Aurbach, D.; Markovsky, B.; Salitra, G.; Markevich, E.; Talyossef, Y.; Koltypin, M.; Nazar, L.; Ellis, B.; Kovacheva, D. *J. Power Sources* **2007,** *165*, 491-499.

127. Lightfoot, P.; Mehta, M. A.; Bruce, P. G. *Science* **1993,** *262*, 883-885.

128. Yamaki, J.-i.; Tobishima, S.-i.; Hayashi, K.; Saito, K.; Nemoto, Y.; Arakawa, M. *J. Power Sources* **1998,** *74*, 219-227.

129. Megahed, S.; Scrosati, B. *J. Power Sources* **1994,** *51*, 79-104.

130. Aurbach, D.; Zinigrad, E.; Cohen, Y.; Teller, H. *Solid State Ion.* **2002,** *148*, 405-416.

131. Zhuang, G. V.; Yang, H.; Blizanac, B.; Philip, J.; Ross, N. *Electrochem. Solid-State Lett.* **2005,** *8*, A441.

132. Assary, R. S.; Lu, J.; Du, P.; Luo , X.; Zhang, X.; Ren, Y.; Curtiss, L. A.; Amine, K. *ChemSusChem* **2013,** *6*, 51-55.

133. Assary, R. S.; Lu, J.; Luo , X.; Zhang, X.; Ren, Y.; Wu, H.; Albishri, H. M.; El-Hady, D. A.; Curtiss, L. A.; Amine, K. *ChemPhysChem* **2014,** *15*, 2077-2083.

134. Truong, T. T.; Qin, Y.; Ren, Y.; Chen, Z.; Chan, M. K.; Greeley, J. P.; Amine, K.; Sun, Y. *Adv. Mater.* **2011,** *23*, 4947-4952.

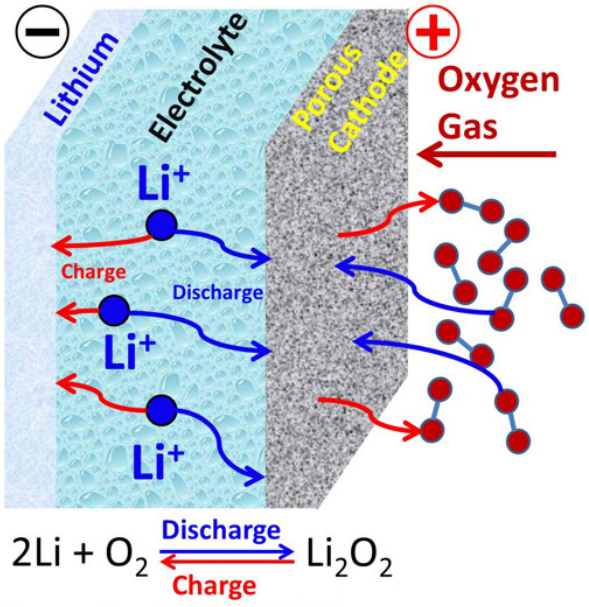

Figure 2.1: Schematic representations of the aprotic Li-O_2 battery.

CHAPTER 3

RESEARCH OBJECTIVES

The Li-O_2 battery has attracted attention due to its high theoretical energy density, which is comparable to gasoline. Hundreds of articles have been published since the first report of the Li-O_2 battery. There is no doubt that significant improvements on cell performance are urgently needed to push the Li-O_2 battery towards practical application, with the top of the list being the development of stable electrolytes to suppress the side reactions and the improvement of cathode performance by tuning its catalytic composition and microstructure. In this work, the following topics are investigated in detail, *i.e.*, the mechanism of discharge product aggregation, and the approaches and effects of the electrocatalysts loaded on cathode. These topics aim at the current major hurdles of the commercial battery, and would help to improve battery performance systematically.

3.1 Mechanism

The nonaqueous rechargeable lithium-oxygen battery, which has the potential to utilize oxygen from air,[1] is a promising energy storage system owing to its ultrahigh energy density (> 3500 Wh/kg by the overall reaction $2Li^{+} + 2e^{-} + O_2 \leftrightarrow Li_2O_2$).[2,3] Ideally, Li_2O_2 is produced by reducing O_2 molecules at the porous catalytic cathode and subsequently combining Li^+ from the electrolyte during the cell discharge. The insoluble Li_2O_2 particles deposit on the porous cathode, which continues for as long as active surface sites for oxygen reduction reaction (ORR) and deposition sites for Li_2O_2 are available. Recharging the cell is expected to decompose Li_2O_2 through the oxygen evolution reaction (OER) to release O_2 and Li^+ and, therefore, recover the active sites and pores on the cathode.

Despite significant progress that has been achieved recently, the Li-O_2 battery is still in its infancy. There is no doubt that significant improvements in cell performance are urgently needed to realize the high theoretical energy densities and practical application of this technology, with the top of the list being the development of stable electrolytes to suppress the side reactions[4-9] and the improvement of cathode performance by tuning its catalytic composition and microstructure.[10-21] It has been shown that the poor performance of the current Li-O_2 cell, including low power output (*i.e.*, low current density), poor cyclability, and low energy efficiency (*i.e.*, large overpotential), are caused by the materials and system design. Beyond that, studies on the mechanism and

underlying electrochemical reactions parameters, which have not been investigated in detail yet, could enable better understanding and design of the Li-O_2 cell.

Recently, Mitchell *et al.*[22] reported a Li-O_2 cell using binder-free hollow carbon fibers as the cathode material, showing an exceptionally high discharge capacity of 7200 mAh/g due to low carbon packing and highly efficient utilization of the available carbon mass and void volume for Li_2O_2 formation. With such a unique structure of the carbon fiber, the toroid-shape Li_2O_2 was the first ever reported as the discharge products, which represents a critical step toward understanding the key processes that limit rate capability and low round-trip efficiencies of the Li-O_2 batteries. The direct evidence using high-resolution transmission electron microscope (HR-TEM) along with electron diffraction pattern on a single toroid, as reported by Lu *et al.*,[13] confirms the presence of Li_2O_2 in the toroids. Findings on the toroidal morphology of Li_2O_2 are interesting since it leads to very nonuniform surface coverage, which is beneficial to increasing the discharge capacity of the cell due to easier oxygen diffusion at the late stage of the discharge. Therefore, understanding and controlling the nucleation and morphological evolution of Li_2O_2 particles upon discharge is the key factor to engineering air electrode structures that can provide high energy and power density of the reversible Li-O_2 cell with long cycle life.

The morphology transition of Li_2O_2 from single-crystalline disc to complex toroid-like particles during the cell discharge has been studied in a nanostructured carbon

electrode with high surface area. Such morphological transition in Li_2O_2 growth is found to be rate dependent based on a vibrational theory of electrochemical kinetics. Under this model, the transition starts in the first monolayer of Li_2O_2, which followed by a transformation of particle growth to film growth if the applied current exceeds the exchange current for the oxygen reduction reaction in a Li-O_2 cell. The mechanism or underlying reasons for the evolution of Li_2O_2 morphology are, however, still not well understood. In particular, the effect of the surface structure of the air cathode on the morphology of the grown Li_2O_2, if any, is still not clear, nor is the effect of Li_2O_2 formation on the mass and charge transport in the air cathode. In order to clarify this, a systemic study is presented in Chapter 5 to show the evolution of Li_2O_2 morphology at different stages of the discharge-charge cycle in a Li-O_2 cell. It is the first time to demonstrate that a sustainable mass transport of diffusive active species (*e.g.*, O_2 and Li^+) and the underlying evolving interfaces are critical to dictate a desirable oxygen reduction and evolution reactions in a porous carbon electrode of Li-O_2 cell.

3.2 Electrocatalysts and Cathode Architecture

The Li-O_2 battery is currently the subject of intense scientific investigation due to the extremely high theoretical energy density of 12 kWh/kg, which far exceeds that of any other existing energy storage technology.[1-3, 23-41] The tremendous theoretical energy density results from using lithium metal as the anode, and from utilizing ambient oxygen

as the cathode oxidant, eliminating the need for an on-board oxygen source and the associated weight penalty. In the Li-O_2 battery, the oxygen electrode should be porous to store the solid products generated from the reaction of Li ions with O_2 during the discharge, and it must integrate a catalyst to promote this reaction. It has been found that a variety of factors dictate the extent of electrochemical (discharge and charge) reactions in Li-O_2 cells including the nature of the catalyst, the catalyst distribution on the porous cathode, the pore volume of the cathode, as well as the type of the applied organic electrolytes.[8, 25, 35-36, 42-43] The design of the oxygen electrode is therefore critical to realizing the full potential of the Li-O_2 cell.[25]

Both the surface area and porosity of the cathode are critical for the performance of Li-O_2 batteries. Larger surface areas provide more catalyst particles and catalytically active sites to accelerate the electrochemical reactions. However, larger surface areas do not always yield larger specific capacities, as has been shown in a previous study by Kuboki *et al.*[44] Qin *et al.* also demonstrated the effects of the cathode porosity on the electrochemical performance, especially the cyclability of the cell, by controlled experiments on MnO_2 catalyst for Li-O_2 batteries.[45] These results illustrate the importance of porosity and, in particular, the pore size. Larger pores facilitate faster oxygen diffusion and provide the volume necessary to accommodate the reduction products deposited during discharge.

For practical application, the Li-O_2 battery must be rechargeable and this

necessitates using a sufficiently high potential or a catalyst to promote the electrochemical reaction.[1, 24] However, high overpotentials on charge and discharge, even at very low current densities of 0.01-0.05 mA/cm^2, result in very low round-trip efficiencies (<60%) and low power capability. It is strongly believed to be dependent on the nature of catalysts applied and their loading process onto the high-surface-area cathode. Metals, metal complexes, and metal oxides have all been examined as the cathode catalysts in the Li-O_2 cells, and these catalysts show large differences in discharge capacity and charge plateau.[1, 3, 33-36, 38, 46-50] However, it should be pointed out that in most cases these catalysts are presynthesized and then dispersed onto the carbon support by mechanical milling.[8, 35, 42, 51] This process can destroy the porous structure of carbon, and is unable to distribute the catalysts on the carbon support uniformly, both of which might severely affect the charge/discharge properties of the oxygen cathode. Consequently, a method is needed for dispersing catalysts with well-controlled particle size uniformly onto the carbon support.

3. 3 References

1. Abraham, K. M.; Jiang, Z. *J. Electrochem. Soc.* **1996**, *143*, 1-5.

2. Laoire, C. O.; Mukerjee, S.; Abraham, K. M.; Plichta, E. J.; Hendrickson, M. A. *J. Phys. Chem. C* **2009**, *113*, 20127-20134.

3. Ogasawara, T.; Debart, A.; Holzapfel, M.; Novak, P.; Bruce, P. G. *J. Am. Chem. Soc.* **2006**, *128*, 1390-1393.

4. Laoire, C. O.; Mukerjee, S.; Abraham, K. M.; Plichta, E. J.; Hendrickson, M. A. *J. Phys. Chem. C* **2010**, *114*, 9178-9186.

5. Zhang, Z. C.; Lu, J.; Assary, R. S.; Du, P.; Wang, H. H.; Sun, Y. K.; Qin, Y.; Lau, K. C.; Greeley, J.; Redfern, P. C.; Iddir, H.; Curtiss, L. A.; Amine, K. *J. Phys. Chem. C* **2011**, *115*, 25535-25542.

6. Du, P.; Lu, J.; Lau, K. C.; Luo, X.; Bareno, J.; Zhang, X.; Ren, Y.; Zhang, Z.; Curtiss, L. A.; Sun, Y.-K.; Amine, K. *Phys. Chem. Chem. Phys.* **2013**, *15*, 5572-5581.

7. Chen, Y.; Freunberger, S. A.; Peng, Z.; Barde, F.; Bruce, P. G. *J. Am. Chem. Soc.* **2012**, *134*, 7952-7957.

8. Freunberger, S. A.; Chen, Y.; Drewett, N. E.; Hardwick, L. J.; Barde, F.; Bruce, P. G. *Angew. Chem. Int. Ed.* **2011**, *50*, 8609-8613.

9. Xu, K. *Chem. Rev.* **2004**, *104*, 4303-4417.

10. Lu, Y.; Wen, Z.; Jin, J.; Cui, Y.; Wu, M.; Sun, S. *J. Solid State Electrochem*. **2012**, *16*, 1863-1868.

11. Shui, J.-L.; Karan, N. K.; Balasubramanian, M.; Li, S.-Y.; Liu, D.-J. *J. Am. Chem. Soc.* **2012**, *134*, 16654-16661.

12. Lei, Y.; Lu, J.; Luo, X.; Wu, T.; Du, P.; Zhang, X.; Ren, Y.; Wen, J.; Miller, D. J.; Miller, J. T.; Sun, Y. K.; Elam, J. W.; Amine, K. *Nano Lett.* **2013**, *13*, 4182-4189.

13. Lu, J.; Lei, Y.; Lau, K. C.; Luo, X.; Du, P.; Wen, J.; Assary, R. S.; Das, U.; Miller, D. J.; Elam, J. W. *Nat. Commun.* **2013**, *4*:2383.

14. Lu, J.; Qin, Y.; Du, P.; Luo, X.; Wu, T.; Ren, Y.; Wen, J.; Miller, D. J.; Miller, J. T.; Amine, K. *RSC Adv.* **2013**, *3*, 8276-8285.

15. Assary, R. S.; Lu, J.; Du, P.; Luo , X.; Zhang, X.; Ren, Y.; Curtiss, L. A.; Amine, K. *ChemSusChem* **2013**, *6*, 51-55.

16. Crowther, O.; Salomon, M. *Membranes* **2012**, *2*, 216-227.

17. Adams, J.; Karulkar, M.; Anandan, V. *J. Power Sources* **2013**, *239*, 132-143.

18. Ottakam Thotiyl, M. M.; Freunberger, S. A.; Peng, Z.; Bruce, P. G. *J. Am. Chem. Soc.* **2012**, *135*, 494-500.

19. Ottakam Thotiyl, M. M.; Freunberger, S. A.; Peng, Z.; Chen, Y.; Liu, Z.; Bruce, P. G. *Nat. Mater.* **2013**, *12*, 1050-1056.

20. Lu, B.; Zhu, C.; Zhang, Z.; Lan, W.; Xie, E. *J. Mater. Chem.* **2012**, *22*, 1375-1379.

21. Hardwick, L. J.; Bruce, P. G. *Curr. Opin. Solid State Mater. Sci.* **2012**, *16*, 178-185.

22. Mitchell, R. R.; Gallant, B. M.; Thompson, C. V.; Shao-Horn, Y. *Energy Environ. Sci.* **2011**, *4*, 2952-2958.

23. Jiao, F.; Bruce, P. G. *Adv. Mater.* **2007,** *19*, 657.

24. Debart, A.; Paterson, A. J.; Bao, J.; Bruce, P. G. *Angew. Chem., Int. Ed.* **2008,** *47*, 4521-4524.

25. Williford, R. E.; Zhang, J.-G. *J. Power Sources* **2009,** *194*, 1164-1170.

26. Andrei, P.; Zheng, J. P.; Hendrickson, M.; Plichta, E. J. *J. Electrochem. Soc.* **2010,** *157*, A1287-A1295.

27. Wang, D.; Xiao, J.; Xu, W.; Zhang, J.-G. *J. Electrochem. Soc.* **2010,** *157*, A760-A764

28. Eswaran, M.; Munichandraiah, N.; Scanlon, L. G. *Electrochem. Solid-State Lett.* **2010,** *13*, A121-A124.

29. Girishkumar, G.; McCloskey, B.; Luntz, A. C.; Swanson, S.; Wilcke, W. *J. Phys. Chem. Lett.* **2010,** *1*, 2193-2203.

30. Hummelshoj, J. S.; Blomqvist, J.; Datta, S.; Vegge, T.; Rossmeisl, J.; Thygesen, K. S.; Luntz, A. C.; Jacobsen, K. W.; Norskov, J. K. *J. Chem. Phys.* **2010,** *132*, 071101.

31. Zhang, J.; Xu, W.; Li, X.; Liu, W. *J. Electrochem. Soc.* **2010,** *157*, A940-A946.

32. Xiao, J.; Wang, D.; Xu, W.; Wang, D.; Williford, R. E.; Liu, J.; Zhang, J.-G. *J. Electrochem. Soc.* **2010,** *157*, A487-A492.

33. Lu, Y.-C.; Gasteiger, H. A.; Crumlin, E.; McGuire, R., Jr.; Shao-Horn, Y. *J. Electrochem. Soc.* **2010,** *157*, A1016-A1025.

34. Lu, Y.-C.; Gasteiger, H. A.; Parent, M. C.; Chiloyan, V.; Shao-Horn, Y. *Electrochem. Solid-State Lett.* **2010,** *13*, A69-A72.

35. Lu, Y.-C.; Xu, Z.; Gasteiger, H. A.; Chen, S.; Hamad-Schifferli, K.; Shao-Horn, Y. *J. Am. Chem. Soc.* **2010,** *132*, 12170-12171.

36. Thapa, A. K.; Saimen, K.; Ishihara, T. *Electrochem. Solid-State Lett.* **2010,** *13*, A165-A167.

37. Bruce, P. G.; Hardwick, L. J.; Abraham, K. M. *MRS Bull.* **2011,** *36*, 506-512.

38. Trahey, L.; Johnson, C. S.; Vaughey, J. T.; Kang, S. H.; Hardwick, L. J.; Freunberger, S. A.; Bruce, P. G.; Thackeray, M. M. *Electrochem. Solid-State Lett.* **2011,** *14*, A64-A66.

39. Wang, Y.; Zhou, H. *Energy Environ. Sci.* **2011,** *4*, 1704-1707.

40. Xu, W.; Xu, K.; Viswanathan, V. V.; Towne, S. A.; Hardy, J. S.; Xiao, J.; Hu, D.; Wang, D.; Zhang, J.-G. *J. Power Sources* **2011,** *196*, 9631-9639.

41. Yoo, E.; Zhou, H. *ACS Nano* **2011,** *5*, 3020-3026.

42. Freunberger, S. A.; Chen, Y.; Peng, Z.; Griffin, J. M.; Hardwick, L. J.; Barde, F.; Novak, P.; Bruce, P. G. *J. Am. Chem. Soc.* **2011,** *133*, 8040-8047.

43. McCloskey, B. D.; Bethune, D. S.; Shelby, R. M.; Girishkumar, G.; Luntz, A. C. *J. Phys. Chem. Lett.* **2011,** *2*, 1161-1166.

44. Kuboki, T.; Okuyama, T.; Ohsaki, T.; Takami, N. *J. Power Sources* **2005,** *146*, 766-769.

45. Qin, Y.; Lu, J.; Du, P.; Chen, Z.; Ren, Y.; Wu, T.; Miller, J. T.; Wen, J.; Miller, D. J.; Zhang, Z.; Amine, K. *Energy & Environmental Science* **2013,** *6*, 519-531.

46. Zhang, G. Q.; Zheng, J. P.; Liang, R.; Zhang, C.; Wang, B.; Au, M.; Hendrickson, M.; Plichta, E. J. *J. Electrochem. Soc.* **2011,** *158*, A822-A827.

47. Ren, X.; Zhang, S. S.; Tran, D. T.; Read, J. *J. Mater. Chem.* **2011,** *21*, 10118-10125.

48. Lu, Y.-C.; Gasteiger, H. A.; Shao-Horn, Y. *Electrochem. Solid-State Lett.* **2011,** *14*, A70-A74.

49. Chung, K.-B.; Shin, J.-K.; Jang, T.-Y.; Noh, D.-K.; Tak, Y.; Baeck, S.-H. *Rev. Adv. Mater. Sci.* **2011,** *28*, 54-58.

50. Chen, J.; Hummelshoj, J. S.; Thygesen, K. S.; Myrdal, J. S. G.; Norskov, J. K.; Vegge, T. *Catal. Today* **2011,** *165*, 2-9.

51. Xu, W.; Xiao, J.; Wang, D. Y.; Zhang, J.; Zhang, J. G. *J. Electrochem. Soc.* **2010,** *157*, A219-A224.

CHAPTER 4

EXPERIMENTAL APPROACHES

4.1 Electrochemical Tests

4.1.1 Cell Assembly

Electrochemical tests were carried out in Swagelok-type cells. As shown in Figure 4.1, the cell consists of a Li-metal anode (7/16 inches in diameter), a glass-fiber separator (1/2 inches in diameter, Fisher Scientific) filled with aprotic electrolyte, a porous carbon cathode (7/16 inches in diameter), and an aluminum mesh (7/16 inches in diameter) as the current collection. These components are sealed except for the Al mesh window, which exposes the porous cathode to O_2. The whole Swagelok cell is assembled in a glove box filled with Ar, and sealed in a glass chamber which is filled with ultrahigh purity oxygen with the pressure 1 bar.

The electrolyte is a solution of lithium salt and ether-based solvent, having one equivalent weight of salt per liter of solution (*i.e.*, concentration 1 M). In this dissertation, $LiCF_3SO_3$ (Sigma-Aldrich) is used as the lithium salt, and the aprotic solvent is tetraethylene glycol dimethyl ether (TEGDME; Sigma-Aldrich).

For cathode electrodes of the cells tested for this dissertation, active materials (porous carbon or carbon + catalyst, 80 wt. %) and the binder (polyvinylidene fluoride (PVDF), 20 wt. %), were mixed in 1-methyl-2-pyrrolidinone (NMP, Aldrich) solution. The slurry was coated on a gas-diffusion layer (TGP-H-030 Torray carbon paper). Then the coated electrodes were dried at 100 °C for 12 hr in a vacuum oven to remove any residual NMP solvent. The mass loading of the active materials is in the range of 0.1-1.0 mg per piece of electrode.

4.1.2 MACCOR System

Electrochemical measurements were conducted with a MACCOR cycler under a constant current density 100 mA/g in the voltage range of 2.2-4.5 V. The observed capacity is normalized by the weight of carbon and catalyst to allow comparison of capacity values. Cell discharge and charge can be carried out in both capacity-controlled and voltage-controlled mode, with equal charge and discharge capacities.

4.2 Catalyst Preparation

Atomic layer deposition (ALD) is applied to deposit the electrocatalysts onto the porous carbon substrate, with enormous help from Dr. Yu Lei and Ms. Mar Piernavieja-Hermida. This is a technique for preparing thin films on planar substrates. It has the capability to deposit highly uniform and conformal coatings on surfaces with complex

topographies and to infiltrate mesoporous materials. In the experiment, ALD was performed in a continuous-flow stainless steel reactor described in detail elsewhere,[1] with the porous carbon substrates and a precursor. About 100 mg carbon powder was carefully spread onto a stainless steel tray, and a stainless steel mesh cover was clamped over the tray to contain the powder while still providing access to the ALD precursor vapors. The carbon powder was held in the reactor at 200 ℃ under continuous flow of 300 sccm ultra-high-purity nitrogen carrier gas at 1 Torr pressure for 30 min to outgas and achieved thermal equilibrium. The Pd ALD was performed using alternating exposures to palladium hexafluoroacetylacetonate($Pd(hfac)_2$, Aldrich, 99.9%) and formalin (Sigma-Aldrich, HCHO 37 wt. % in H_2O) at 200 °C. Timing sequence of a complete ALD cycle can be expressed as t_1-t_2-t_3-t_4, corresponding to the precursor exposure time, N_2 purge time, co-reactant exposure time and N_2 purge time, respectively. The timing sequence utilized for the Pd ALD was 100-300-100-300. Catalyst samples were prepared using 1, 3, and 10 ALD cycles on the carbon powder. The weight loading for each Pd ALD cycle is approximately 1 wt. %.

4.3 Characterization

4.3.1 Electron Microscope

A field-emission scanning electron microscope (SEM, Hitachi S-4700), field-emission transmission electron microscope (TEM, FEI Titan 80-300ST), and scanning

transmission electron microscope (STEM, JEOL JEM-2100F FEG FasTEM) were carried out in the electron microscopy center (EMC) at Argonne National Laboratory. They were employed to evaluate the morphology, particles size, and distribution of the electrocatalysts and discharge products. The ultrahigh resolution mode was selected for the SEM examination, with the accelerating voltage (V_{acc}) 5.0 kV and emission current (I_e) 10 to 15 μA. The samples were protected from exposure to air during transferring to the SEM chamber by a conductive tape applied in the glove box. The TEM samples were examined at an accelerating voltage of 80 kV for the TEM and 200 kV for the STEM. To prepare TEM specimens, a dilute suspension was prepared by ultrasonically dispersing the sample powder in ethanol for 5 min, and a drop of the suspension was placed onto a copper grid and dried.

4.3.2 High Energy X-ray Diffraction (HE-XRD)

High energy X-ray diffraction (HE-XRD) is used to determine the cathode materials and discharge products. The experiments were operated at the Sector 11 of the Advanced Photon Source (APS), Argonne National Laboratory, with the X-ray wavelength around 0.11 Å at beamline 11-ID-C and around 0.77 Å at beamline 11-ID-D. The samples were sealed up with a Kapton tape in the glove box. The 2-D patterns were collected in the transmission mode using a 2-D detector (a Perkin–Elmer large-area detector for beamline 11-ID-C and a Piratus 2M detector for beamline 11-ID-D), and

transformed to 1-D patterns (intensity vs. 2θ) or final data analysis by integration with the FIT2D software.

4.3.3 X-ray Absorption Structure (XAS)

K-edge X-ray absorption spectroscopy (XAS) was performed at the Materials Research Collaborative Access Team (MRCAT) at APS, Argonne National Laboratory. The amount of sample used was optimized for a step height of about 0.5 for the Pd/C samples and about 1 for the Pd/ZnO/C samples. The XAFS spectra were recorded in the transmission mode. Standard procedures based on WINXAS 3.1 software and Athena in the IFEFFIT (version 1.2.11) package were used to normalize and fit the X-ray absorption spectroscopy data. The extended X-ray absorption fine structure (EXAFS) coordination parameters were obtained by a least-square fit in q- and r-space of the isolated nearest neighbor, k^2- weighted Fourier transform data.

4.3.4 X-ray Photoelectron Spectroscopy (XPS)

Pd/C samples were analyzed by X-ray photoelectron spectroscopy (XPS) using a Kratos™ Axis Ultra DLD surface analysis instrument. The base pressure of the analysis chamber during these experiments was 3×10^{-10} Torr, with operating pressures around 1×10^{-9} Torr. Spectra were collected with a monochromatic Al Kα source (1486.7 eV) and a 300 × 700 micron spot size. Prior to introduction into the load-lock vacuum chamber of

the XPS instrument, all air-sensitive samples were loaded into an inert transfer module interfaced with the instrument. Samples were prepared in an Ar-filled glove box, with no more than 1 ppm O_2 and 1 ppm H_2O. Nonconductive samples showed evidence of differential charging, resulting in peak shifts and broadening. Photoelectron peak positions were shifted back toward their true values, and their peak widths were minimized by flooding the samples with low-energy electrons and ions from the charge neutralizer system on the instrument. Peak position correction was further corrected by referencing the C 1s peak position of adventitious carbon for a sample (284.8 eV, PHI Handbook of Photoelectron Spectroscopy), and shifting all other peaks in the spectrum accordingly.

Fitting was done by using the program CasaXPS. Peaks were fit as asymmetric Gaussian/Lorentzians, with 0-30 % Lorentzian character. The FWHM of all subpeaks was constrained to 0.7-2.0 eV, as dictated by instrumental parameters, lifetime broadening factors, and broadening due to sample charging. With this native resolution set, peaks were added, and the best fit, using a least-squares fitting routine, was obtained while adhering to the constraints mentioned above.

4.3.5 Electrochemical Impedance Spectroscopy (EIS)

Impedance was measured with an EG&G 273A potentiostat and a Solartron SI1260 Frequency Response Analyzer. The measurement was taken every 2 hr during

the electrochemical cycle, with frequency ranging from 0.1 Hz to1 MHz.

4.4 References

1. Metz, B.; Davidson, O.; Coninck, H. C. d.; Loss, M.; Meyer, L. A. *IPCC Special Report on Carbon Dioxide Capture and Storage*, 2005.

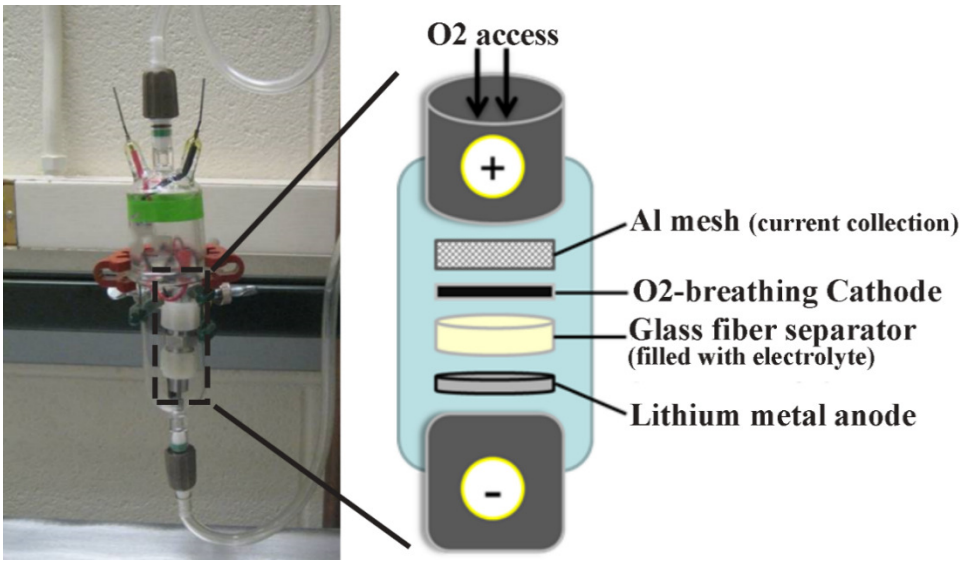

Figure 4.1: Real configuration of the Swagelok-type cell sealed in a glass chamber used for the electrochemical cycles.

CHAPTER 5

MASS AND CHARGE TRANSPORT RELEVANT TO THE FORMATION OF TOROIDAL LITHIUM PEROXIDE NANOPARTICLES

5.1 Experimental Results

To monitor the evolution of Li_2O_2 (*i.e.*, discharge product) morphology, the cells were discharged to different specific capacities and subsequently subjected to SEM observation. The left column in Figure 5.1 shows the SEM images of discharged cathodes at 400, 600, 1200, and 1800 mAh/g, respectively. Typically, a short discharge process (*i.e.*, 400 mAh/g, as shown in Fig. 5.1a) only yields small spherical nanoparticles decorated on porous carbon surface. Scattered toroid-like particles start to appear on the cathode at the discharge capacity of 600 mAh/g (Fig. 5.1c). The size and quantity of these toroid-like particles significantly increase with prolonging the discharge depth to 1200 mAh/g, as shown in Figure 5.1e. When the cell is fully discharged to 2.2 V (>1800 mAh/g), the carbon cathode is completely covered by the toroids with significantly increased particle size (Fig. 5.1g). High-energy XRD

patterns of the cathodes harvested at different discharge depth are shown in Figure 5.2b. The intensity of the peaks increased along with the capacity (pattern 1-5), indicating a growth of the discharge product Li_2O_2.

The different discharge capacities lead to the multifarious morphology of discharge product. They also affect the following charge process. After short discharge processes, the Li_2O_2 toroid were decomposed in the following charge processes, and disappeared when capacity matched (Fig. 5.1b and d). For the charge after deeper discharge 1200 mAh/g, the reduction of Li_2O_2 along with capacity is shown in the XRD spectra (Fig. 5.2b). However, the decomposition is not complete, and the left grains (Fig. 5.1f) influence the following cycles. Cathodes discharged after several cycles are also observed by SEM, shown in Figure 5.3. The discharge products on the carbon cathode appear to be toroid particles after the first, second, and tenth discharge (Fig. 5.3b-d) cycle with 800 mAh/g capacity control. The particle size and quantity increase along with the cycle number. Because the OER cannot fully decompose the Li_2O_2 toroid produced in the long discharge process, there is an inference that in the following discharge process, new products crystallize on the grains left from the previous charge process, which work as the “core” of the new toroid. The size of the core increases due to each incomplete charge; thereupon the toroid size increases until they clog the carbon pore and bring sudden death to the cell.[1]

When the fully discharged cathode is charged with capacity-match, the toroid is merely smaller in volume. The coverage is still complete and would limit the O_2 diffusion, which is a key factor for the discharge actions.[2] The charge capacity is more likely caused by the decomposition of the electrolyte. Figure 5.4 illustrates the charge-discharge curves responses for the 400 mAh/g, 600 mAh/g, 800 mAh/g, 1200 mAh/g, and deep discharge-charge cycles, with the voltage limited in the range of 2.2-4.5 V. The charge potentials are generally found to be larger than 4 V, due to the lack of electrocatalysts in this investigation into the mechanism of discharge product. Charge overpotential, which even exists at very low current density, is one of the major challenges for the Li-O_2 battery. Based on the results in Figure 5.4, it can be divided into two parts: charge overpotential I and II. Part I generally exists in every battery, caused by the material of electrode, current density, temperature, etc. Part II gradually increases along with the corresponding discharge capacity and the change of the Li_2O_2 morphology. As the quantity and size of toroid increase, extra energy is needed to decompose the structure during charge, and results in larger charge overpotential.

Because of the poor electrical conductivity of Li_2O_2, the impact of Li_2O_2 accumulation with cycling on the charge and mass transport in the porous air electrode were valued by the *in situ* electrochemical impedance spectra as shown in Figure 5.5. The impedance spectra were measured after every 2 hr (*i.e.*, 200 mAh/g)

in the first and the fifth 1200 mAh/g capacity-controlled cycle (Fig. 5.5a) and at the end of each charge or discharge pleasure for the 3 cycles in between (Fig. 5.5b). As shown in Figure 5.5a and b, all the EIS plots consist of two semicircles at high to medium frequency range and one slope at the low frequency range. In the first cycle, the first semicircle (the one at the high frequency range) is not so obvious due to its small diameter, but it keeps on enlarging upon cycling in the next four cycles, which is consistent with the growth of solid-electrolyte interphase (SEI) layer on the Li metal electrode. Therefore, the first semicircle is assigned to the resistance (R_{SEI}) – capacitor (C_{SEI}) circuit of the SEI layer, and the second semicircle (the one at the medium frequency range) to the charge transfer resistance (R_{ct}) – double layer capacitor (C_{dl}) circuit of the carbon electrode. The slope at the low frequency range is typically a Warburg diffusion impedance (W_o) element, which can be assigned to the O_2 diffusion in the cathode. According to the above analysis, the equivalent circuit shown in Figure 5.5c was used to fit the plots. Besides the elements defined above, the R_e represents the resistance of the electrolyte.

Figure 5.5d shows the resistance values from the fitting results for the impedance spectra in Figure 5.5a and b. The constant increasing of R_e can be attributed to the decomposition of electrolyte, which is one of the big challenges of the Li-O_2 battery, while the R_W and R_{ct} of the air electrode rise and fall regularly upon discharge and charge. During the discharge, the insoluble product (Li_2O_2) forms and

clogs part of the pores in cathode, preventing the O_2 from diffusing freely and therefore increasing the diffusion resistance R_W. Meanwhile, the Li_2O_2 particles also cover the active sites on the surface of the electrode, leading to the increase in the R_{ct}. During the charge, the Li_2O_2 decomposes into Li^+ ions and O_2, releasing the O_2 diffusion paths and the active sites on carbon, and hence the R_W and R_{ct} decrease. On the other hand, the overall trends of the R_W and R_{ct} over the five cycles are opposite to each other. The R_W rises from one cycle to the next, which agrees with the decrease in the porosity of the cathode after cycling as shown in the SEM images in Figure 5.3. This is because that the Li_2O_2 generated in the discharge cannot be completely decomposed in the charge, resulting in the increasing amount of Li_2O_2 on cathode blocking the diffusion of O_2. Instead, the R_{ct} falls rapidly from cycle to cycle after the first big bumping, indicating reactions other than the Li^+-O_2 redox reaction may occur when the surface of the carbon electrode is covered by the Li_2O_2 particles. In addition, as the EIS were measured with a two-electrode cell, the impedance of the cathode and anode may not be perfectly distinguished. A three-electrode system with appropriate design would help to provide more accurate information on the Li-O_2 cell, especially the air electrode.

5.2 AIMD Calculations

The gradual resistance increase suggests a mass transportation during the discharge. To understand the possible mechanism and primary features of these impedance results, the analysis is turned into atomistic modelling based on AIMD calculations, with the great help from Dr. K-C Lau. In general, we found the basic experimental finding is supported by AIMD simulation. To represent the Li ions and O_2 transport variation and the reduction of these reactive species during the discharge process, the time-evolution of these processes is simulated based on AIMD. The local structure of the porous carbon electrode is shown in Figure 5.6 with tunnel-like pore size ~ 8 Å and length ~ 14 Å within the sp^2-bond carbon networks. Prior to the discharge process, the pore is empty and an O_2 molecule and two Li^+ (*i.e.*, a Li_2O_2 stoichiometric unit) are randomly placed within the pore. During the thermal equilibration at T = 300 K, both the Li^+ and O_2 molecule are found to be behave quite similarly and move randomly governed by thermally activated self-diffusion of these reactive species. Prior to the formation of Li_2O_2, the mean square displacement (MSD) of both O_2 and Li^+ trajectories are both found to be nearly linear time-dependent proportional to diffusion constant of each species (*i.e.*, $<r_i^2(t)> \sim D_i t$). As shown in Figure 5.6a, this linear MSD behavior is reflected nearly isotropically at x-, y-, and z-direction. However as discharge process proceed and when Li_2O_2 formed (as more Li^+ and O_2 units placed within the pore), the motion of these reactive species

becomes less mobile once the chemical bonds formed among these constituent species (Fig. 5.7). Instead of randomly moved initially, the newly added O_2 molecule are found to be significantly less mobile (*i.e.*, MSD is ~ 6-7 times less than prior discharge process as shown in Fig. 5.7a) when $[Li_2O_2]_{14}$ units are formed within the pore (Fig. 5.7b) with atomic density, ρ ~ 1.9 g/cm^3. Thus we expect the further reduction process of reactive species will be thermodynamically unfavorable once the Li_2O_2 formed within the pore approaching atomic density of Li_2O_2 bulk, *i.e.*, ρ ~ 2.3 g/cm^3.

AIMD results of slow O_2 diffusion during Li_2O_2 formation in the pore are consistent with the sharp increase at the end of the discharge process that was attributed to complete choking of the carbon that prevent further O_2 reduction, analogous to the increase in Warburg resistance (W) that related to diffusion resistance of mass transport within the cathode (Fig. 5.5). Besides causing the clogging of the pores during the Li_2O_2 formation in the pore, the continuous accumulation of reduced reactive species of Li^+ and O_2 on the interfaces of micropores of carbon is also affecting the charge transfer process that dictates the ORR during the discharge process. According to DFT calculation, a continuous accumulation of reduced Li^+/O_2 within the pore that forms the Li_2O_2 units can hinder the charge transfer process at the carbon electrode interface. The $[Li_2O_2]_N$ aggregates will become insulating-like in electronic properties when approaching bulk Li_2O_2 as

discharge process proceeds. As shown by the electronic density of states (DOS) in Figure 5.7a, the initial interface of pore is metallic and dominated by the carbon atoms. Prior to ORR during discharge process, the DOS of the diffusive O_2 molecule is discrete-like as expected, in contrast to relatively broadend DOS of reduced O_2 species (Fig. 5.7). As discharge process proceeds with continuous accumulation of Li_2O_2 on the carbon interfaces, the insulating-like Li_2O_2 DOS is dominating the DOS at the Fermi-level of the system as shown in Figure 5.7b. Therefore it is expected that, as Li_2O_2 bulk ultimately formed within the pore, the electronic conduction channels within the system will be blocked if the insulating-like Li_2O_2-bulk feature dominated the system Fermi-level, analogous to the increase in charge transfer resistance (R_{ct}) during discharge as observed in the experiment (Fig. 5.5). It is believed this can be attributed to the decreased in electronic and ionic conducting path in the carbon electrode when the Li_2O_2 insulating layers passivate the carbon interfaces.

It is worth noting that there is a bump between 300 mAh/g and 700 mAh/g in the discharge plateau in Fig. 5.2), while the Li_2O_2 particles form toroid in SEM images. The bump reveals the change of energy, which indicates that the Li_2O_2 toroid may not form by a direct reaction between Li^+ and O_2, but self-assemble through a multistep reaction.

5.3 Conclusions

In summary, the insoluble discharge product, Li_2O_2 particles, accumulates on the O_2-breathing cathode to form a toroidal shape, which clogs the pores and covers the active sites in the cathode. During the charge process, Li_2O_2 decomposes into Li^+ ions and O_2 by OER, and releases the O_2 diffusion paths and the active sites. The different discharge capacities lead to the multifarious morphology of discharge product, and affect the following charge process in the aspects of overpotential, reaction rate, *etc*. The EIS, AIMD, and DFT calculation were applied to simulate the mass and charge transportation. The simulation results indicate that the active species become immobile once the Li_2O_2 chemical bonds formed. The continous accumulation of the discharge products not only clogs the pores in the O_2-breathing cathode, but also hinders the charge transfer process. According to the results, it is possible to demonstrate the importance of a maintainable mass transport of active species to the desirable ORR and OER in the O_2-breathing cathode of the Li-O_2 battery.

5.4 References

1. Viswanathan, V.; Thygesen, K. S.; Hummelshoj, J. S.; Norskov, J. K.; Girishkumar, G.; McCloskey, B. D.; Luntz, A. C. *J. Chem. Phys.* **2011,** *135*, 214704.

2. Read, J. *J. Electrochem. Soc.* **2002,** *149*, A1190-A1195.

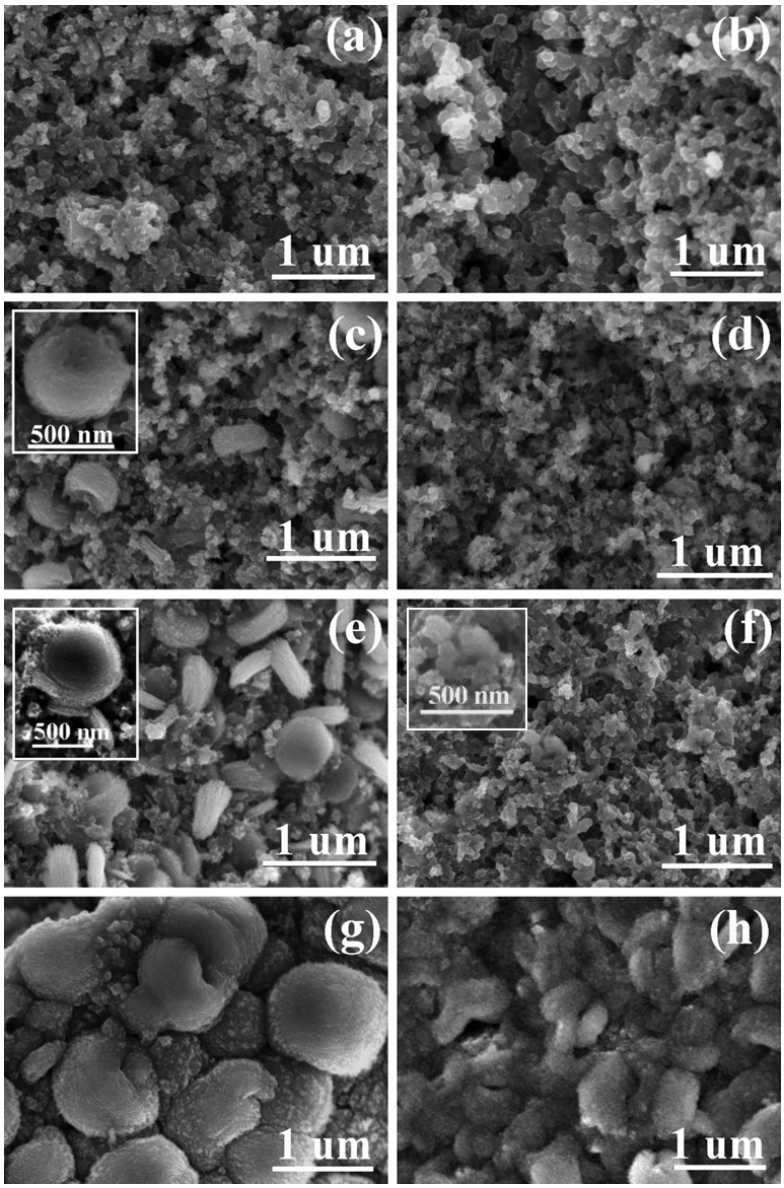

Figure 5.1: SEM images for the graphitized carbon electrodes which are (a) discharged and (b) charged for 400 mAh/g each, (c) discharged and (d) charged for 600 mAh/g each, (e) discharged and (f) charged for 1200 mAh/g each, (g) discharged to 2V (~ 1800 mAh/g), and (h) charged back with the capacity matched.

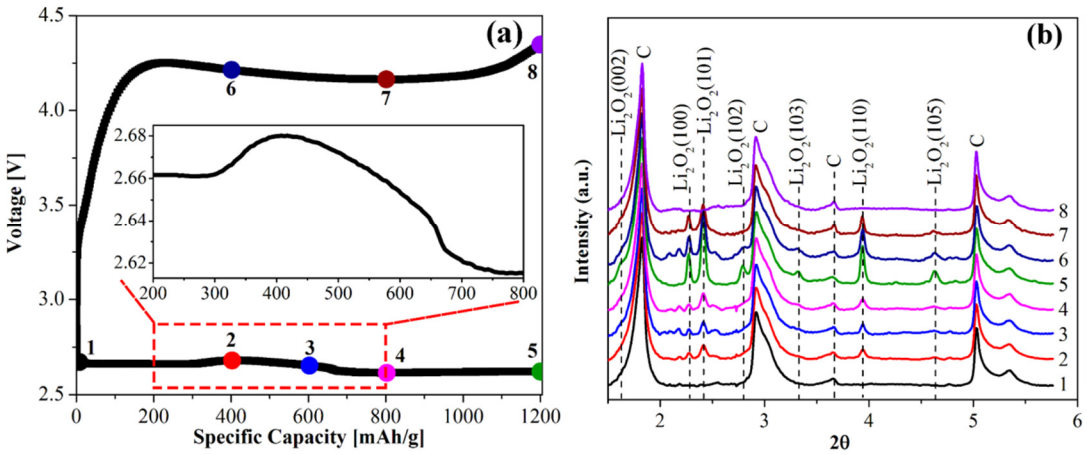

Figure 5.2: Reaction products studied by diffraction patterns. (a) The voltage profile of a 1200 mAh/g capacity-controlled cycle. (b) HE-XRD patterns for graphitized carbon cathodes under different discharge or charge capacities.

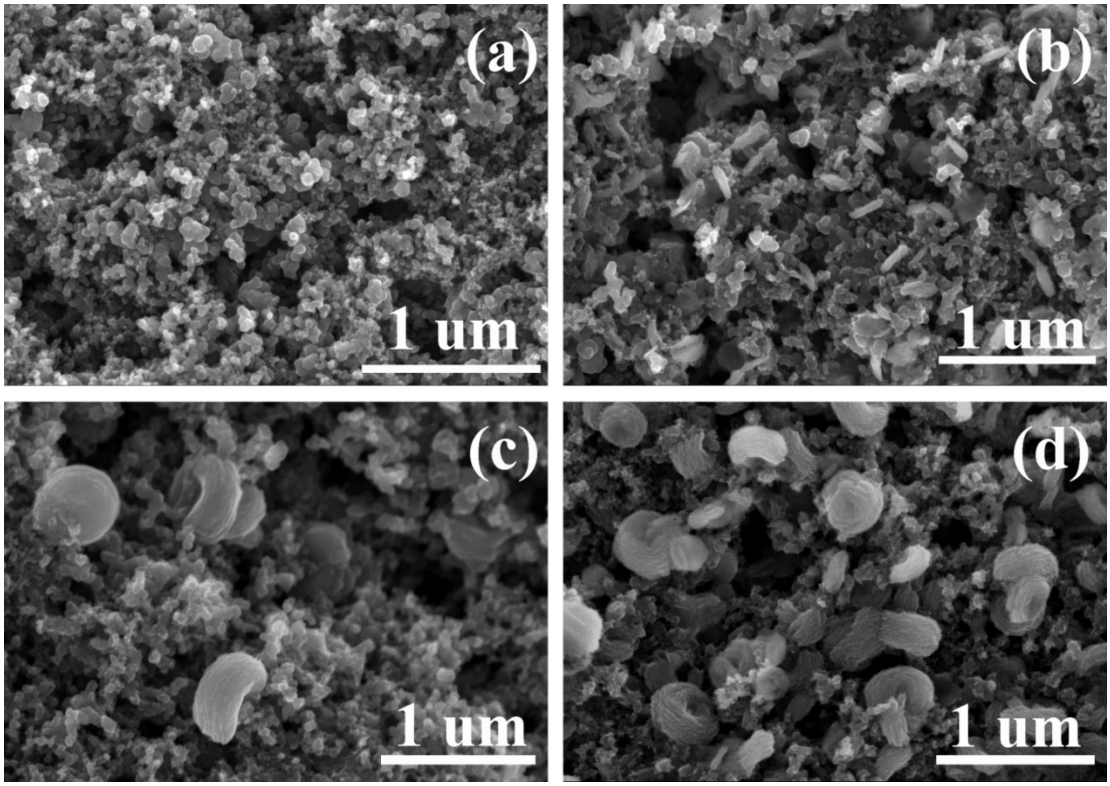

Figure 5.3: SEM images for (a) pristine graphitized carbon electrode; and the electrodes appearance after discharge process (b) 1st discharge cycle, (c) 2nd discharge cycle and (d) 10th discharge cycle with 800 mAh/g capacity controlled.

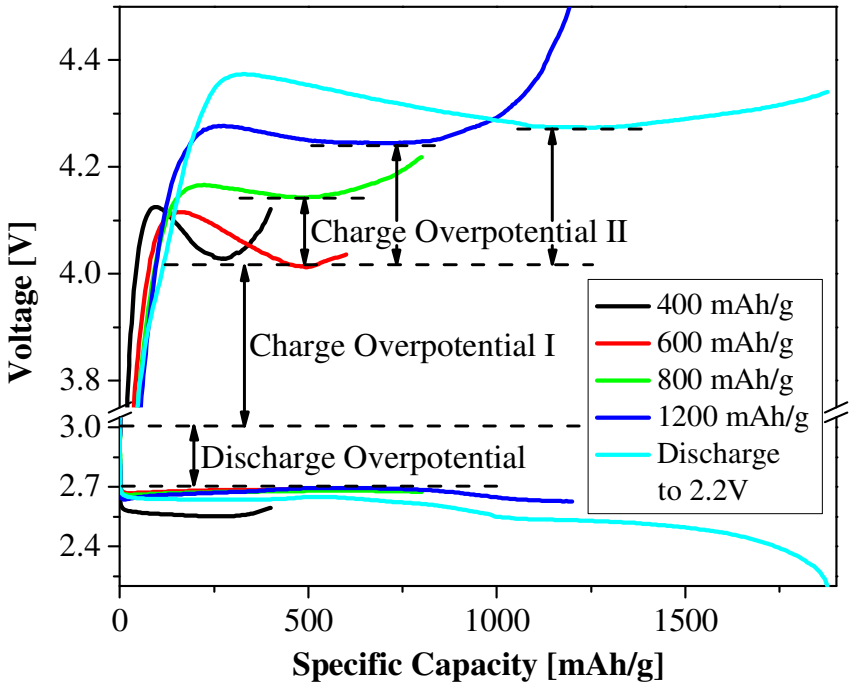

Figure 5.4: The voltage profile as a function of discharge capacity with constant current density of 100 mA/g.

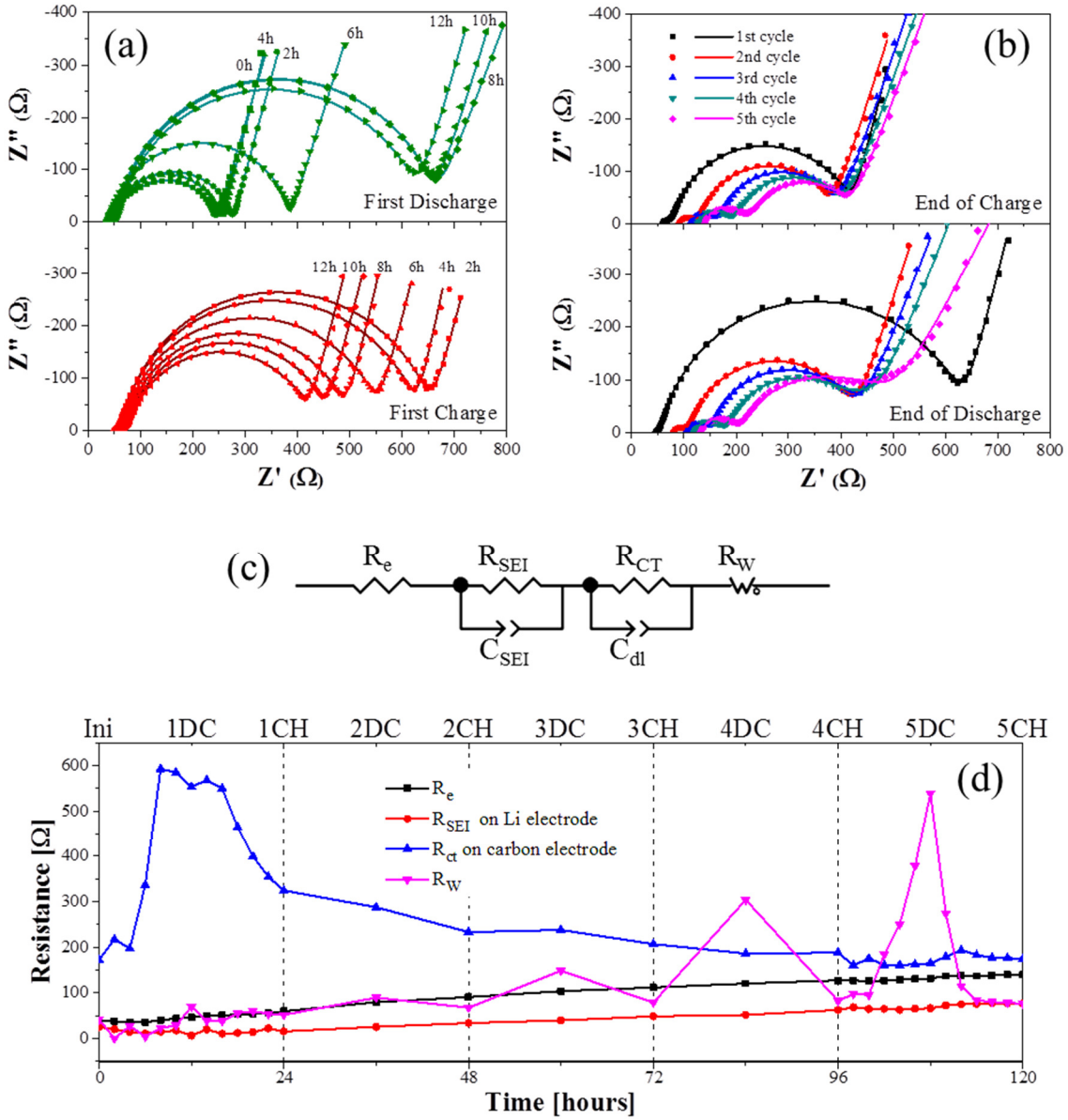

Figure 5.5: Nyquist impedance plots of the Li-O_2 cell (a) after every 2 hr in the first discharge-charge cycle and (b) at the end of each discharge or charge plateaus for the first 5 cycles, (c) equivalent circuit for the impedance data fitting and (d) variation of the resistance values of the fitting results. In the Nyquist impedance plots, experimental data are shown as scatters and the fit data as smooth curves.

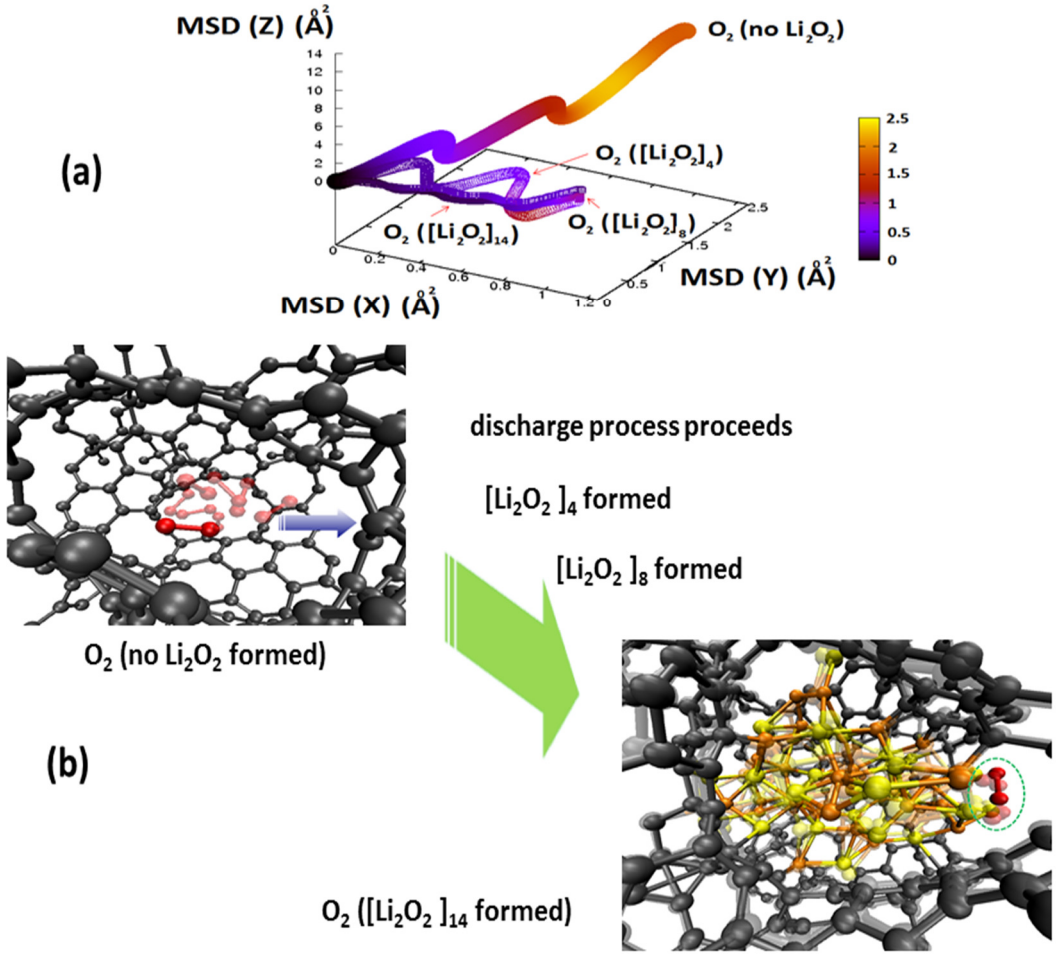

Figure 5.6: Theoretical study of the formation of Li_2O_2 nanoparticles. (a) The mean-square displacement (MSD) in three directions (*x*-,*y*-and *z*-axis) of the trajectory of O_2 gas molecule during the different stages of discharge process from initial (*i.e.*, no Li_2O_2 formed) till $[Li_2O_2]_{14}$ units formed in the pore. (b) The selected snapshot of atomic motion for a free O_2 gas (*i.e.*, no Li_2O_2 formed) and a chemically bonded O_2 species when Li_2O_2 formed during the discharge process.

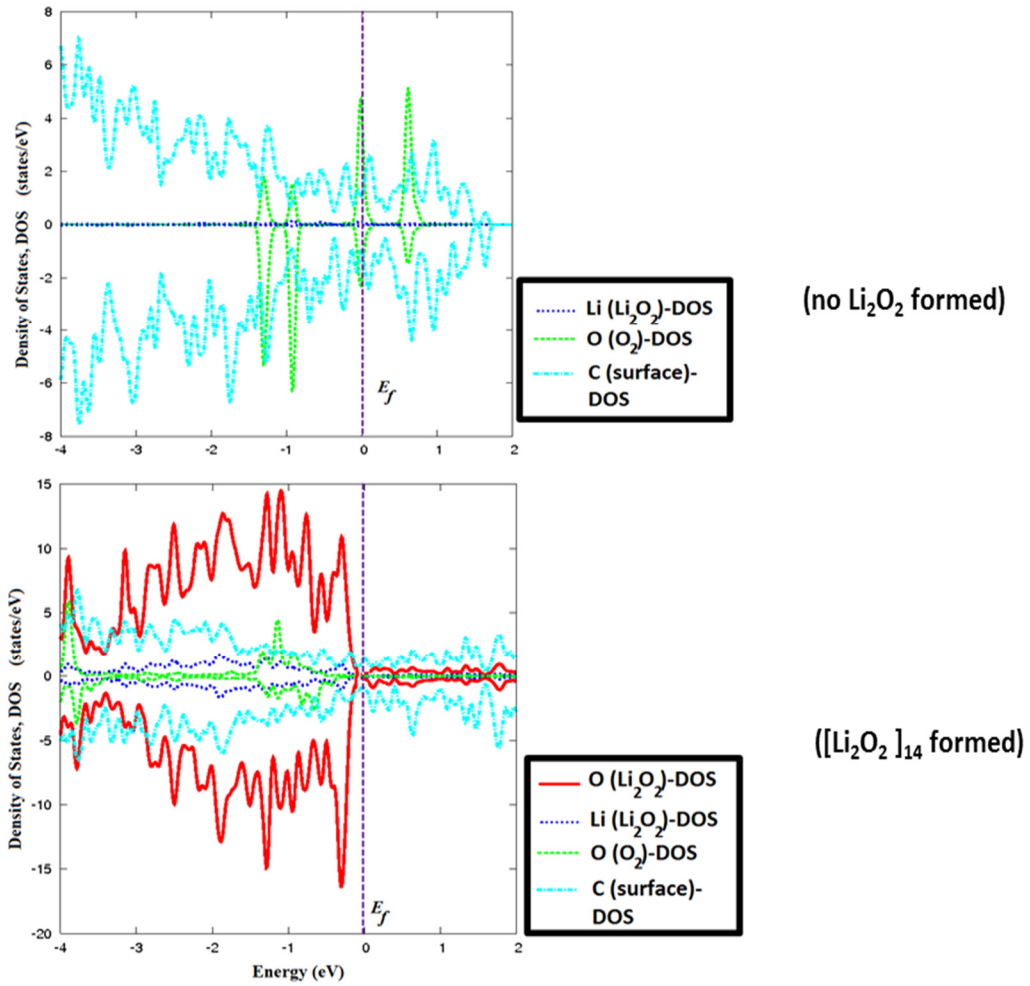

Figure 5.7: The electronic density of states (DOS) of different atomic species formed at the interface of carbon pore before (a) and during (b) the discharge process within the vicinity of the Fermi-level (E_f). The atomic color-code: O (Li_2O_2) in red, Li (Li_2O_2) in blue, O (from O_2 gas molecule) in green, and C (surface of pore) in light blue.

CHAPTER 6

CATHODE ARCHITECTURE I: SYNTHESIS OF POROUS CARBON SUPPORTED PALLADIUM NANOPARTICLE

Reprinted with permission from *Nano Lett.*, **2013**, *13* (9), pp 4182–4189.

6.1 Introduction

Atomic layer deposition (ALD) is a technique for preparing thin films on planar substrates that employs self-limiting chemical reactions between gaseous precursors and a solid surface allowing atomic scale control over the film thickness and composition.[1-2] One of the distinguishing attributes of ALD is the capability to deposit highly uniform and conformal coatings on surfaces with complex topographies and to infiltrate mesoporous materials.[3-5] This feature is particularly attractive for the synthesis of heterogeneous catalysts requiring highly dispersed catalytic species on high surface area, mesoporous supports. Consequently, ALD is being explored as an alternative method for preparing advanced catalysts.[6-10]

The layer-by-layer growth process afforded by ALD typically yields smooth, uniform films, and this is ideal for most microelectronics applications. However, nonuniform deposits can occur when the ALD chemistry is inhibited on the starting substrate or when the ALD material aggregates from surface diffusion. Both of these mechanisms are in effect in the early stages of noble metal ALD on oxide surfaces, which result in the formation of discrete, three-dimensional nanoparticles decorating the surface. This behavior has been exploited to synthesize supported noble metal catalysts exhibiting remarkably high activity as a result of the highly dispersed, small noble metal particles.[11-14] The good dispersion of the active particles on the support during ALD enables a decreasing of the metal loading while still achieving the same catalytic activity as the catalysts with higher metal loading prepared by other methods. This is especially important with noble metal materials where the excess use of the raw materials should be avoided. Uniformed palladium nanoparticles in the size range from subnanometer to a few nanometers, one of the most efficient catalysts for facilitating the oxygen reduction reaction (ORR) in the fuel cell, have been synthesized by ALD on high surface area supports.[11-12, 15-16] However, performing ALD on a porous carbon surface in general has been a technical challenge because of the lack of active sites on carbon for surface reactions, and therefore has not been well studied.

In this study, uniformly dispersed Pd nanoparticles are prepared by the ALD process onto a porous carbon support, exhibiting high electrochemical catalytic activity in

a Li-O_2 cell. STEM and XAS are used to characterize the structure and composition of the ALD Pd/C electrocatalysts. The electrochemical activity of these catalysts is determined using Swagelok-type Li-O_2 cells, and results are compared with those obtained with a bare porous carbon cathode.

6.2 Results and Discussion

The phase purity and crystal structure of the as-prepared ALD Pd/C samples were characterized by high-energy XRD, and the results for the 3-cycle and 10-cycle samples are presented in Figure 6.1a along with the XRD pattern for the original SPL carbon for comparison. With the exception of the SPL carbon peaks, all the peaks for the 10-cycle ALD Pd/C sample in Figure 6.1a can be readily indexed to a pure *fcc* structure with the lattice constant a = 3.89 Å, in good agreement with the reported value for Pd found in the inorganic crystal structure database (ICSD). The average grain size for the 10-cycle ALD Pd/C sample is estimated by the Scherrer equation to be ~7 nm, which is further confirmed by the TEM analysis described below. It was difficult to identify Pd in the 1-cycle and 3-cycle ALD Pd/C samples using XRD due to the relatively low Pd loading. However, Pd in 1-cycle and 3-cycle ALD Pd/C samples can be readily detected using TEM and EXAFS, as demonstrated below.

Representative STEM images of the 1-cycle, 3-cycle and 10-cycle ALD Pd/C samples are illustrated in Figure 6.2a–c, respectively. Well-dispersed and uniform Pd

nanoparticles were prepared over the SPL carbon after 1 cycle and 3 cycles of Pd ALD. However, the 10-cycle sample shows agglomerated Pd nanoparticles (Fig. 6.2c). The average size of Pd nanoparticles was determined from multiple images recorded for each sample to be 2.6, 5.5, and 8 nm following 1, 3, and 10 ALD cycles of Pd, respectively, as shown in Figure 6.2e. In comparison to published literature, the average sizes of Pd nanoparticles on the porous carbon are larger than those on metal oxide surfaces prepared using similar conditions. For instance, on alumina (Al_2O_3), 1 ALD cycle of Pd at 200 °C yields Pd nanoparticles with a diameter of ~1 nm.[11, 17] Only after 25 ALD cycles of Pd does the nanoparticle size increase to 2.9 ± 0.9 nm.[17] Moreover, the metal oxide surfaces yield a higher density of Pd nanoparticles compared to the SPL carbon. These results suggest that there are fewer nucleation sites for the Pd ALD on the SPL carbon as compared to metal oxides, and that Pd diffuses more rapidly on the carbon yielding a smaller number of larger particles. Nevertheless, the Pd coverage on carbon surface is very uniform, as supported by the SEM EDX mapping images (Fig. 6.3a-c). Figure 6.2d shows a high-resolution transmission electron microscopy (TEM) image for a ~5.5 nm Pd/C sample, where lattice fringes for the metal nanoparticles are clearly visible. The nanoparticles show lattice fringes of ~0.23 nm, which is consistent with the *d*-spacing for the Pd [111] plane.[18] These TEM images provide direct evidence that the metal nanoparticles are well crystalline and faceted. In addition, SEM images (Fig. 6.3d-e) on the samples before and after Pd ALD reveal that the porous structure of the carbon is well

preserved during the Pd ALD, which is critical to achieve high performance in Li-O_2 cells.

The chemical composition of the Pd nanoparticles was determined using linear combination fitting of X-ray absorption near edge structure (XANES) spectra recorded in air at room temperature. To facilitate these measurements, XANES reference spectra were recorded for a Pd foil and a PdO standard, as shown in Figure 6.1b. The XANES spectra of 1c, 3c, and 10c Pd/C were compared in Figure 6.1b. With increasing ALD cycles, Pd step edges show a slight shift to lower energy and decreasing whiteline intensity. In comparison to the XANES reference of Pd foil and PdO, this indicates an increase in the percentage of the metallic component for the Pd nanoparticles. The quantitative results obtained from linear combination fittings are illustrated in Figure 6.1c. The 1-cycle Pd/C with the smallest Pd particle size of ~ 2.5 nm consists of ~26% (atomic percent) PdO, and this is the highest PdO content of the three samples. With increasing particle size, the PdO content decreases linearly to a value of ~9% for the 8 nm particles. The fraction of surface atoms in these Pd nano-particles, given by 0.9/size (nm), is 0.36, 0.16, and 0.11 for 2.5, 5.5, and 8 nm Pd and very similar to the fraction of PdO determined from the XANES, suggesting that primarily the surface of the Pd particles are oxidized.

Figure 6.1d shows the Fourier transforms of the extended X-ray absorption fine structure (EXAFS). The peaks at about 2 and 2.5 Å are fingerprint peaks in the first shell

for metallic Pd. The Fourier transform measurements for the ALD Pd samples all show similar features in the first shell, but the peak intensities increase with increasing ALD cycles, *i.e.*, particle size, determined by STEM. In comparison to the Pd foil spectrum, the as-prepared 1-cycle ALD Pd/C measured in air is clearly partially oxidized, showing an additional peak at around 1.4 Å that is typically associated with the Pd-O bond. The EXAFS data were fit, and the results of this quantitative analysis are listed in Table 6.1. The nearest Pd-Pd bond distances are in good agreement with XRD data (2.76 Å). As expected, the Pd-Pd coordination number increases with increasing particle size. The coordination number of nearest Pd-O neighbors in the Pd oxide reference is 4. Thus, the percentage of PdO in the ALD Pd/C samples can also be calculated as $CN_{Pd-O}/4$. The fractions of PdO calculated from the EXAFS measurements are 32.5, 17.5, and 10% for the 1c, 3c, and 10c ALD Pd/C samples, respectively, which are within the error of the results obtained from the XANES linear combination fittings. Similar to the XANES analysis, the fraction of the oxidized Pd determined from the EXAFS fits is very similar to the fraction of surface Pd in these metallic nanoparticles.

On the basis of all the above results, there are two conclusions as follows: (1) the as-prepared Pd/C is surface oxidized and has a crystalline *fcc* structure, and the average particle size is controlled by the number of ALD Pd cycles to be in the range 2-8 nm; (2) the as-prepared Pd nanoparticles are uniformly distributed on the porous carbon surface. These as-prepared Pd/C composites with porous structures and high specific surface area

are of particular interest, since they can provide more active sites to absorb O_2 molecules. This should enhance the catalytic activity for the oxygen reduction reaction (ORR) and the oxygen evolution reaction (OER), as demonstrated below for the Li-O_2 cell.

A Swagelok-type cell consisting of a Li-foil anode and an as-prepared 3c-ALD Pd/C cathode was tested under O_2 atmosphere with a MACCOR cycler. TEGDME-$LiCF_3SO_3$ was selected as an electrolyte, since it was recently demonstrated to be relatively stable towards the discharge product, Li_2O_2, during the discharge reaction.[19] For comparison, the cell containing the cathode with the same loading of SPL carbon only was also tested under similar conditions. Figure 6.4a shows voltage profiles of the first discharge to 2.0 V (deep discharge) under a discharge rate of 100 mA/g. The initial discharge reaction of the cell containing the 3c-ALD Pd/C cathode takes place at approximately 2.70 V, with a total specific capacity of about 6600 mAh/g. The cell with only bare SPL carbon as the cathode, however, only delivered about 1500 mAh/g with a discharge voltage of 2.5 V, which is a few hundred millivolts lower than that of the 3c-ALD Pd/C cathode. This finding provides strong evidence that the oxygen reduction reaction during discharge in the Li-O_2 cell is greatly facilitated when 3c-ALD Pd on carbon is used as the electrocatalyst, which not only contributes to a higher capacity by providing more active sites for the ORR reaction, but also leads to a higher discharge potential. The discharge products on the 3c-ALD Pd/C cathode were subjected to XRD measurement, and results are shown in Figure 6.4b. The diffraction patterns of the

discharged cathode clearly show that Li_2O_2 is the main discharge product on the 3c-ALD Pd/C cathode, while the discharge product on the bare carbon cathode appeared to be only LiOH with no evidence of crystalline Li_2O_2.[20] Note that a small amount of the LiOH was also detected on the 3c-ALD Pd/C samples, which is likely due to the reaction between Li_2O_2 and H_2O either from the residual moisture left on the electrode or from the air during the XRD measurements. The SEM image of the 3c-ALD Pd/C cathode harvested after first discharge clearly showed a large amount of "donut"-like particles, presumably Li_2O_2,[21] filled the pores of the carbon cathode (Fig. 6.5a), while only amorphous-like products are observed for the bare carbon cathode after first discharge (Fig. 6.5b). This result probably indicates that the nucleation of Li_2O_2 strongly depends on the catalytic surface.

In an attempt to fully recover the discharge product, I employed an equal-capacity charging mode in which the cutoff charging condition was specified so that the charging capacity matched the previous discharging capacity, while the charge potential was limited to 4.5 V. Under this mode, the charge of the cell was terminated when either of these conditions was achieved. Figure 6.6a shows the cycle performance of the Li-O_2 cell containing the 3c-ALD Pd/C cathode, from which it can be seen that severe polarization occurred during the first charge. Around 6500 mAh/g was recovered at the 4.3 V plateau during the charge, which accounts for more than 98% (Columbic efficiency) of the discharge capacity. On the second discharge to 2.0 V, the capacity dropped dramatically

to 3000 mAh/g. This result indicates that part of this capacity recovered during the first cycle may come from the electrolyte decomposition at relative high charge potential (>4.3 V).[22] In other words, Li_2O_2 formed during the first discharge does not completely decompose upon charging, which leads to the blocking of the active site or pores. The SEM image of cathode after being charged on the first cycle (Fig. 6.5c) indeed showed some toroid-like Li_2O_2 left on the surface, supporting the above clarification. The deep discharge conditions can also lead to poor cycle performance once an accumulation of the insulating discharge products, particularly lithium peroxide, impedes the transportation of lithium ions, oxygen, and electrons in the electrode. Another possible cause of capacity failure is the poisoning of the Pd catalyst by contaminants or passivation. A buildup of contaminants such as Li_2CO_3 could be the result of gradual decomposition of the TEGDME electrolyte such as by reaction with the Li_2O_2 surface, as found experimentally.[23] All of these aspects would likely lead to the poor cycle performance of the Li-O_2 cell, as presented above.

Figure 6.6c illustrates the voltage profile of the first cycle for the 10c-ALD Pd sample as the cathode material in a Li-O_2 cell. A similar discharge potential (~2.7 V) was achieved which shows the catalytic effect of the 10c-ALD Pd sample towards the oxygen reduction reaction during discharge in the Li-O_2 cell, although the cell delivers much less capacity (~1700 mAh/g) compared to the 3c-ALD Pd sample. The decrease of the capacity of the 10c-ALD sample compared to the 3c-ALD sample is probably due to the

loss of the active site on the cathode surface. The discharge products on the 10c-ALD Pd cathode mainly consist of Li_2O_2, as shown in Figure 6.4b. Surprisingly, the charge potential is significantly lowered to about ~3.4 V, compared to that of 3c-ALD Pd (Fig. 6.6b), 1c-ALD Pd (Fig. 6.6d), and bare carbon (Fig. 6.6e) samples, and this charge potential can be maintained for several cycles (>5). At this stage, the mechanism that leads to the low charge overpotential for the 10c-ALD Pd sample has not been completely understood, which needs to be further explored. It is likely that more coverage of the carbon surface (*i.e.*, the defect sites) in the 10c-ALD Pd sample would not only lead to better electron transfer for the nucleation and growth of Li_2O_2, but also would minimize the possible electrolyte decomposition on the carbon defect sites. Such electrolyte decomposition will result in the deposition of contaminants such as carbonates on the lithium peroxide or on the carbon surface and would likely increase the charge potential. Nevertheless, this is an encouraging result showing that a low charge potential can be achieved when a suitable electrocatalyst is applied to the carbon. It should also be noted that there appear to be two discharge plateaus during the discharge of all ALD-Pd coated carbon samples, which is likely attributed to the impedance change due to the insulation nature of the discharge product, Li_2O_2.

X-ray photoelectron spectra (XPS) were used to investigate the catalyst surface and identify the discharge and charge products during the electrochemical reactions, which were obtained from the 10c-ALD Pd/C cathode in the first discharged and first

charged state, respectively. The Li 1s and Pd 3d XPS spectra were recorded and fitted, as shown in Figure 6.7. Figure 6.7a (bottom spectrum) shows the Li 1s XPS spectrum for the first discharge sample, from which it can be concluded that lithium peroxide formed as the dominant discharge product of the electrochemical reactions[20] along with a small amount of LiOH, which is consistent with the XRD results. The XPS data confirm that the desired discharge product (lithium peroxide) can be produced when a suitable catalyst, in this case the 10c-ALD Pd/C composite, is introduced on the cathode. On the basis of the above XRD and XPS results, it is clearly demonstrated that the catalyst plays a key role in facilitating the oxygen reduction reaction and forming the desired discharge product, Li_2O_2. Upon charging, the lithium signals from lithium peroxide completely disappeared (Fig. 6.7a, first charge), suggesting that these discharged products decompose during the charging process. This finding provides solid evidence that lithium peroxide can be formed and decomposed reversibly during the cycle test of the TEGDME-based Li-O_2 cells.

Figure 6.7b presents the Pd 3d core level XPS spectra of the prepared 10c-ALD Pd/C cathode for different electrochemical treatments (charge/discharge), as marked in the figure. Analysis of the Pd 3d spectrum for the first discharge electrode shows no Pd signal, indicating that Li_2O_2 was sufficiently thick to completely attenuate photoelectrons from the Pd nanoparticles. In other words, the oxygen reduction reaction does take place on the surface of the catalyst during discharge of the cell. The Pd signal reappeared in the

charged samples (first charge in Fig. 6.7b), since the discharge products were decomposed and removed from the electrode surface. It should also be noted that the Pd nanoparticle surface oxidized to PdO_2 during the cycle testing in the Li-O_2 cell.

Finally, it should be noted that although TEGDME, which is used in the present study as the electrolyte, is suspected to be unstable on deep discharge in Li-O_2 cells at potential <2.4 V, it is still of great interest to explore the reactions that may occur in the presence of different catalysts that may promote the two-electron reduction of oxygen to lithium peroxide. Irrespective of the electrolyte problems mentioned above, and in parallel with new efforts with more promising electrolytes,[19, 24] the goal in this study has been to explore a novel approach and design new electrode/electrocatalytic materials for the oxygen cathode, which might help overcome at least some of the limitations of current Li-O_2 cells.

6.3 Conclusions

In summary, ALD was used to synthesize Pd nanoparticles on a porous carbon support and the resulting materials were employed as electrocatalysts for rechargeable Li-O_2 cells. Both XRD and XAFS analyses confirmed the presence of crystalline, metallic Pd. The conformal attribute of ALD ensured that the Pd nanoparticles were uniformly dispersed over the high surface area carbon support, and that the porous structure and surface area were well preserved. As a consequence, the as-prepared catalysts

demonstrated a superior electrochemical behavior, and delivered a capacity of up to 6600 mAh/g (carbon + electrocatalyst) using a current density of 100 mA/g. This reaction was reasonably reversible during the early cycles. These results suggest that ALD is a promising technique for tailoring the surface composition and structure of porous supports in energy storage devices.

6.4 References

1. Puurunen, R. L. *J. Appl. Phys.* **2005,** *97*, 121301-121352.

2. Leskela, M.; Ritala, M. *Thin Solid Films* **2002,** *409*, 138-146.

3. Elam, J. W.; Routkevitch, D.; Mardilovich, P. P.; George, S. M. *Chem. Mater.* **2003,** *15*, 3507-3517.

4. Shin, H. J.; Jeong, D. K.; Lee, J. G.; Sung, M. M.; Kim, J. Y. *Adv. Mater.* **2004,** *16*, 1197.

5. Chen, P.; Mitsui, T.; Farmer, D. B.; Golovchenko, J.; Gordon, R. G.; Branton, D. *Nano Lett.* **2004,** *4*, 1333-1337.

6. Pellin, M. J.; Stair, P. C.; Xiong, G.; Elam, J. W.; Birrell, J.; Curtiss, L.; George, S. M.; Han, C. Y.; Iton, L.; Kung, H.; Kung, M.; Wang, H. H. *Catal. Lett.* **2005,** *102*, 127-130.

7. Jiang, X. R.; Huang, H.; Prinz, F. B.; Bent, S. F. *Chem. Mater.* **2008,** *20*, 3897-3905.

8. Herrera, J. E.; Kwak, J. H.; Hu, J. Z.; Wang, Y.; Peden, C. H. F.; Macht, J.; Iglesia, E. *J. Catal.* **2006,** *239*, 200-211.

9. Keranen, J.; Auroux, A.; Ek, S.; Niinisto, L. *Appl. Catal., A* **2002,** *228*, 213-225.

10. Lei, Y.; Mehmood, F.; Lee, S.; Greeley, J.; Lee, B.; Seifert, S.; Winans, R. E.; Elam, J. W.; Meyer, R. J.; Redfern, P. C.; Teschner, D.; Schlogl, R.; Pellin, M. J.; Curtiss, L.

A.; Vajda, S. *Science* **2010,** *328*, 224-228.

11. Feng, H.; Libera, J. A.; Stair, P. C.; Miller, J. T.; Elam, J. W. *ACS Catal.* **2011,** *1*, 665-673.

12. Lu, J. L.; Stair, P. C. *Angew. Chem., Int. Ed.* **2010,** *49*, 2547-2551.

13. Christensen, S. T.; Elam, J. W.; Rabuffetti, F. A.; Ma, Q.; Weigand, S. J.; Lee, B.; Seifert, S.; Stair, P. C.; Poeppelmeier, K. R.; Hersam, M. C.; Bedzyk, M. J. *Small* **2009,** *5*, 750-757.

14. Lei, Y.; Lu, J. L.; Zhao, H. Y.; Liu, B.; Low, K.-B.; Wu, T. P.; Libera, J. A.; Greeley, J. P.; Chupas, P. J.; Miller, J. T.; Elam, J. W. *J. Phys. Chem. C* **2013**, *117*, 11141-11148.

15. Feng, H.; Elam, J. W.; Libera, J. A.; Setthapun, W.; Stair, P. C. *Chem. Mater.* **2010,** *22*, 3133-3142.

16. Lu, J. L.; Fu, B. S.; Kung, M. C.; Xiao, G. M.; Elam, J. W.; Kung, H. H.; Stair, P. C. *Science* **2012,** *335*, 1205-1208.

17. Lu, J. L.; Stair, P. C. *Langmuir* **2010,** *26*, 16486-16495.

18. Shao, M. H.; Yu, T.; Odell, J. H.; Jin, M. S.; Xia, Y. N. *Chem. Comm.* **2011,** *47*, 6566-6568.

19. Laoire, C. O.; Mukerjee, S.; Plichta, E. J.; Hendrickson, M. A.; Abraham, K. M. *J. Electrochem. Soc.* **2011,** *158*, A302-A308.

20. Lu, J.; Qin, Y.; Du, P.; Luo, X.; Wu, T.; Ren, Y.; Wen, J.; Miller, D. J.; Miller, J. T.; Amine, K. *RSC Adv.* **2013,** *3*, 8276-8285.

21. Lu,Y.-C.; Kwabi, D. G.; Yao, K. P. C.; Harding, J. R.; Zhou, J.; Zuin, L.; Shao-Horn, Y. *Energy Environ. Sci.* **2011,** *4*, 2999-3007.

22. McCloskey, B. D.; Scheffler, R.; Speidel, A.; Girishkumar, G.; Luntz, A. C. *J. Phys. Chem. C* **2012,** *116*, 23897-23905.

23. McCloskey, B. D.; Speidel, A.; Scheffler, R.; Miller, D. C.; Viswanathan, V.; Hummelshoj, J. S.; Norskov, J. K.; Luntz, A. C. *J. Phys. Chem. Lett.* **2012,** *3*, 997-1001.

24. Zhang, Z. C.; Lu, J.; Assary, R. S.; Du, P.; Wang, H. H.; Sun, Y. K.; Qin, Y.; Lau, K. C.; Greeley, J.; Redfern, P. C.; Iddir, H.; Curtiss, L. A.; Amine, K. *J. Phys. Chem. C* **2011,** *115*, 25535-25542.

Table 6.1. Structural Parameters of Different Pd Samples Measured Under Ambient Conditions

Sample	TEM Size (nm)	Scatter	CN	R (Å)	DWF ($\times 10^3$)	E_o (eV)
1c Pd/C	2.6	Pd-Pd	5.3	2.74	3	0.8
		Pd-O	1.3	2.05	1	3.1
3c Pd/C	5.5	Pd-Pd	8.2	2.75	2	0.6
		Pd-O	0.7	2.05	1	2.0
10c Pd/C	8	Pd-Pd	9.2	2.74	1	1.4
		Pd-O	0.4	2.05	1	3.8

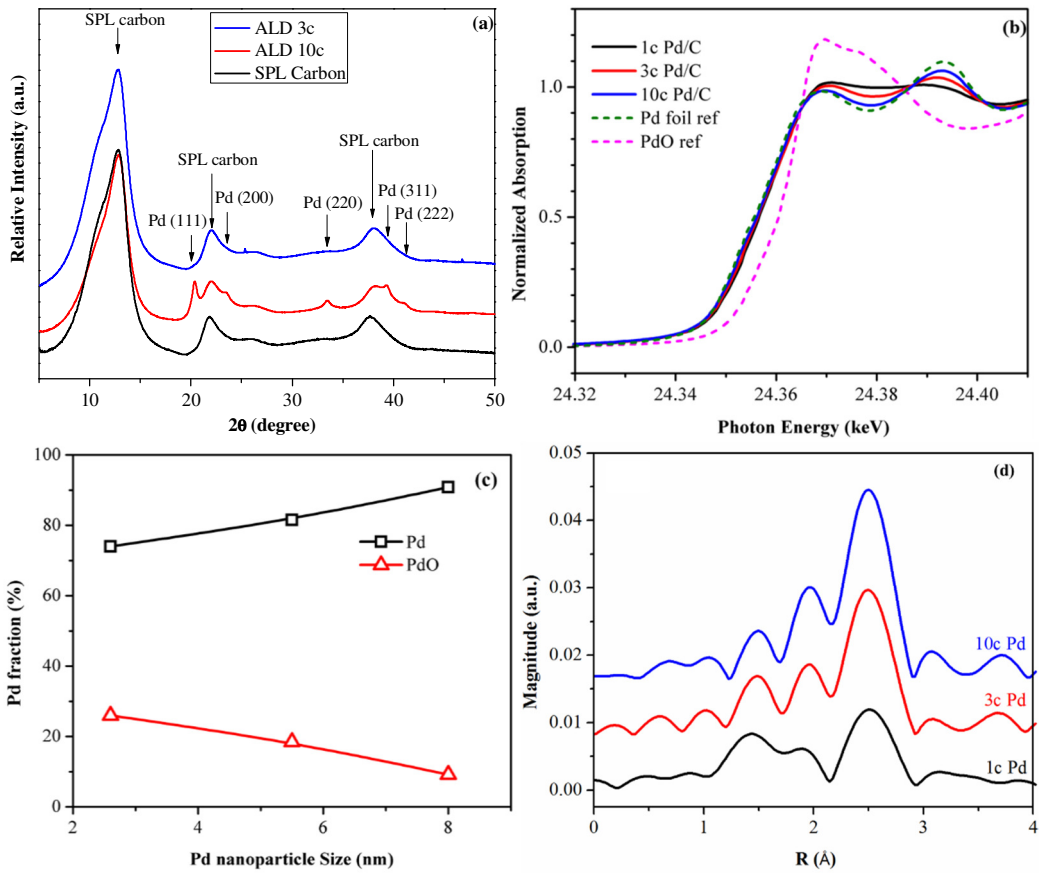

Figure 6.1: Characterization of the as-prepared Pd/C samples. (a) High-resolution XRD patterns of original SPL carbon and SPL carbon after being loaded with Pd catalyst using 3 and 10 cycles of Pd ALD; (b) XANES spectra for 1c Pd (black solid line), 3c Pd (red solid line), 10c Pd (blue solid line) and XANES reference spectra for metallic Pd foil reference (olive dash line) and Pd oxide reference (magenta dash line). (c) Pd oxide fraction of Pd/C samples, obtained using XANES linear combination. (d) Fourier transform of X-ray absorption spectra (k^2: Δk = 2.8-11 $Å^{-1}$). Fitting these data provides the data in Table 6.1.

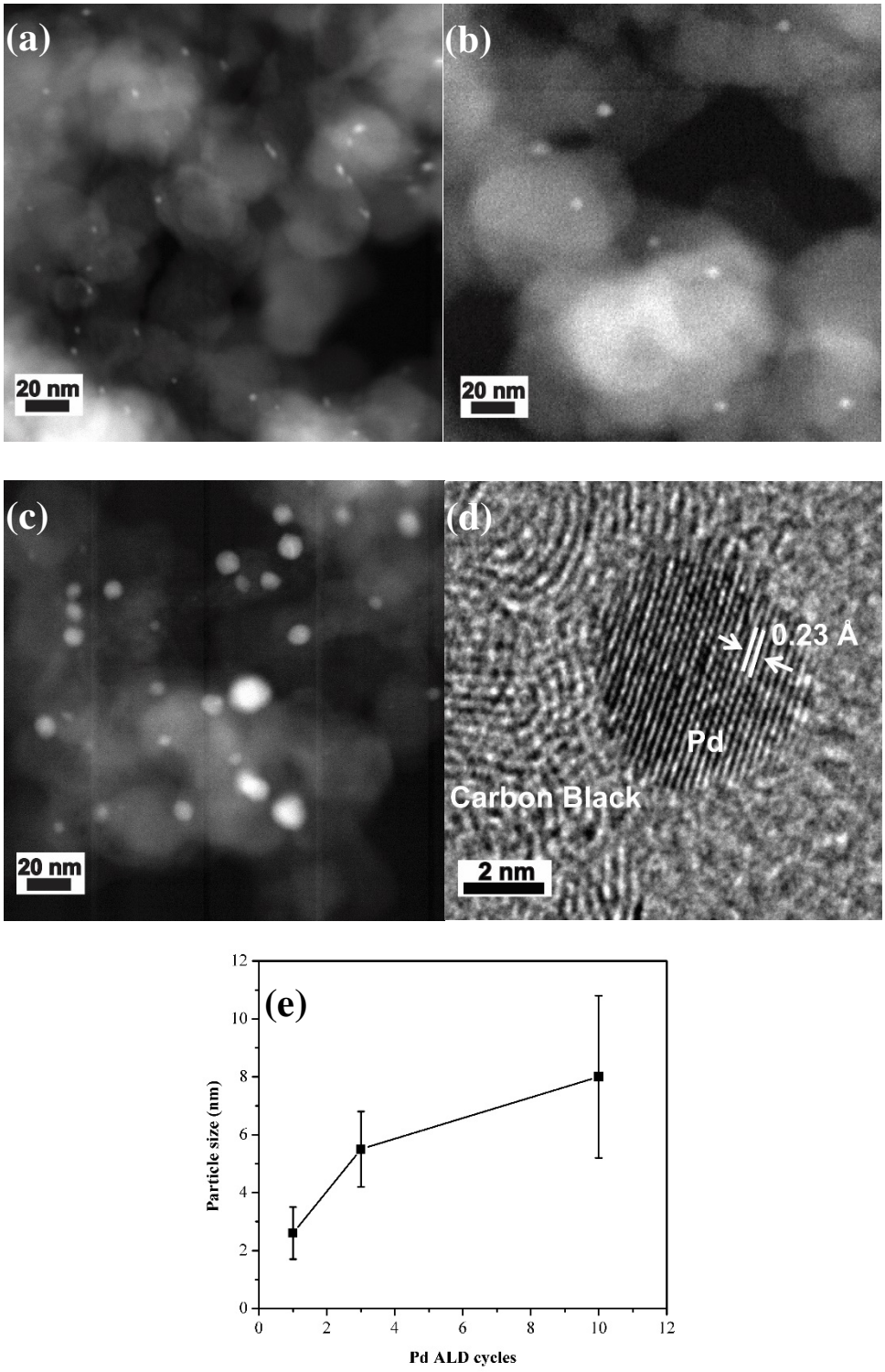

Figure 6.2: STEM images of (a) 1c Pd/C, (b) 3c Pd/C, (c) 10c Pd/C. (d) HRTEM of a Pd nanoparticle ~5.5 nm in diameter prepared by ALD supported over carbon. (e) Pd particle size as a function of ALD cycles.

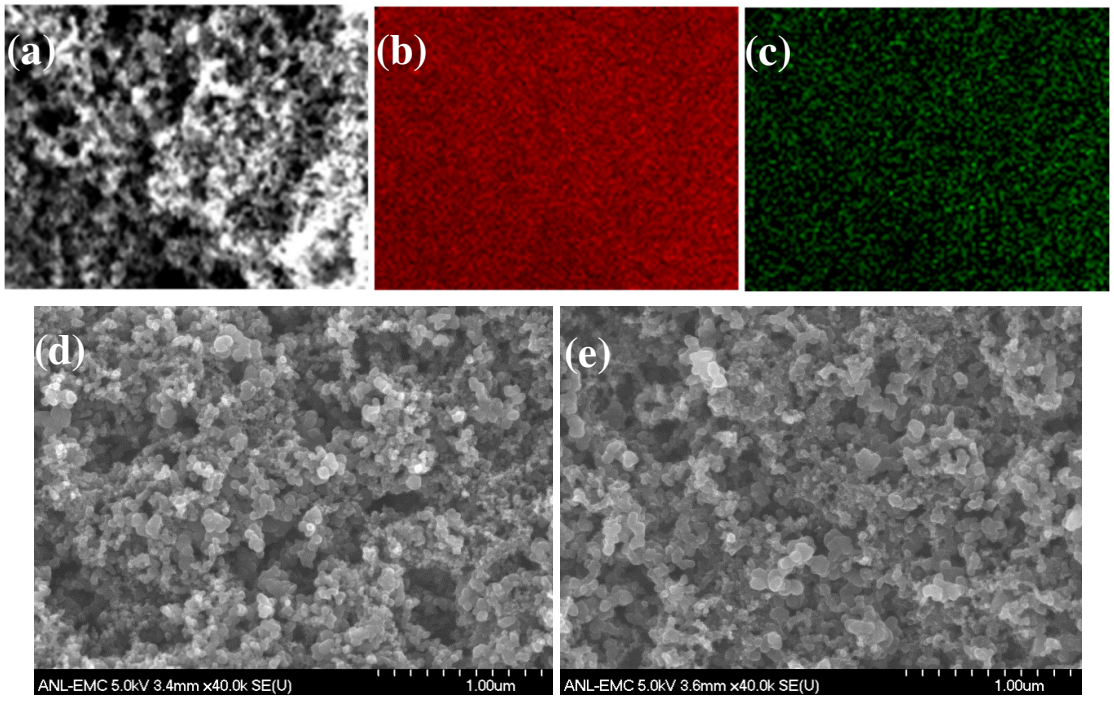

Figure 6.3: SEM images and EDX mappings. (a) SEM image of 10c Pd-ALD coated carbon; (b) EDX elemental mappings of C; and (c) EDX elemental mapping of Pd; SEM images of SPL carbon before (d) and after (e) being loaded with Pd nanoparticles ALD approach.

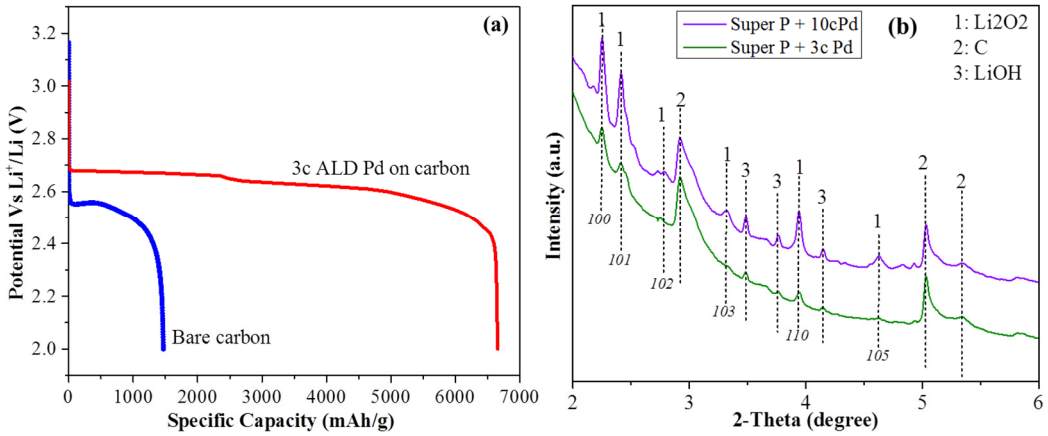

Figure 6.4: Discharge products studied by diffraction patterns. (a) Voltage profile of the first discharge for cathode containing bare carbon and 3c-ALD Pd/C in 1M $LiCF_3SO_3$/TEGDME at 100 mA/g; (b) XRD patterns of cathode containing 3c-ALD Pd/C (bottom) and10c-ALD Pd/C (top) as active materials after first discharge to 2.0 V and 2.2 V, respectively.

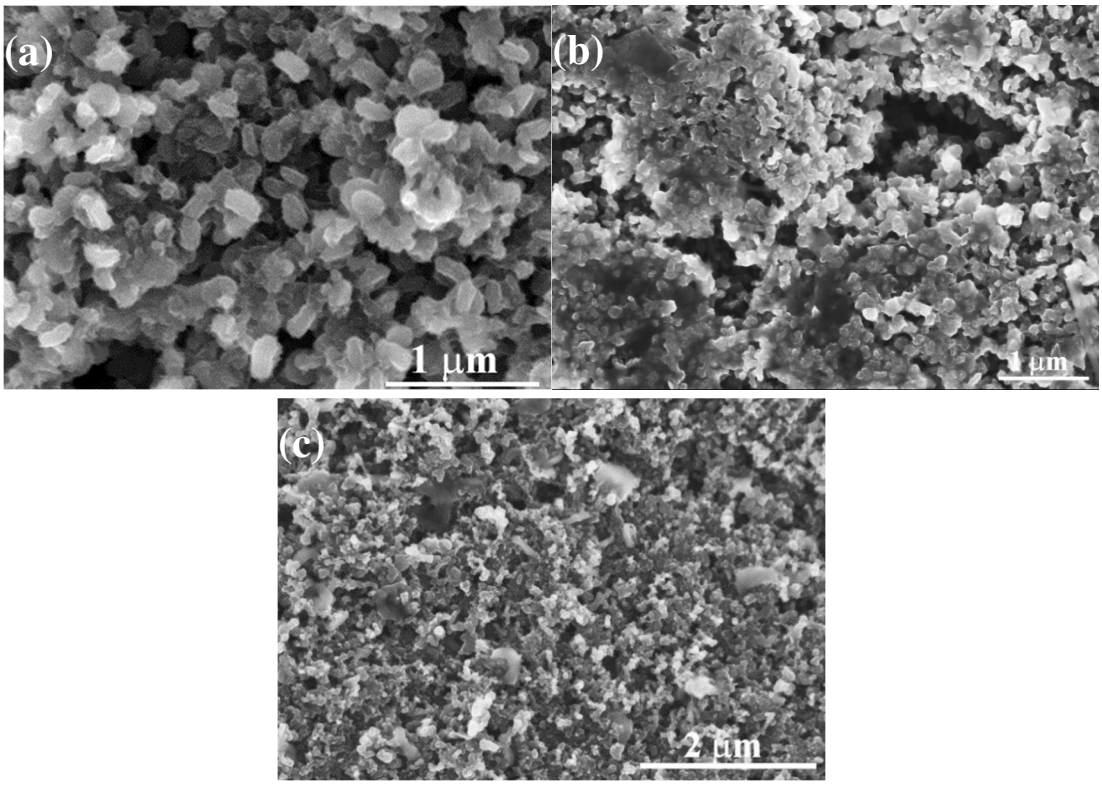

Figure 6.5: SEM image of (a) the 3c-ALD Pd/C cathode harvested after 1st discharge, (b) the bare carbon cathode harvested after 1st discharge, and (c) the 3c-ALD Pd/C cathode harvested after 1st charge.

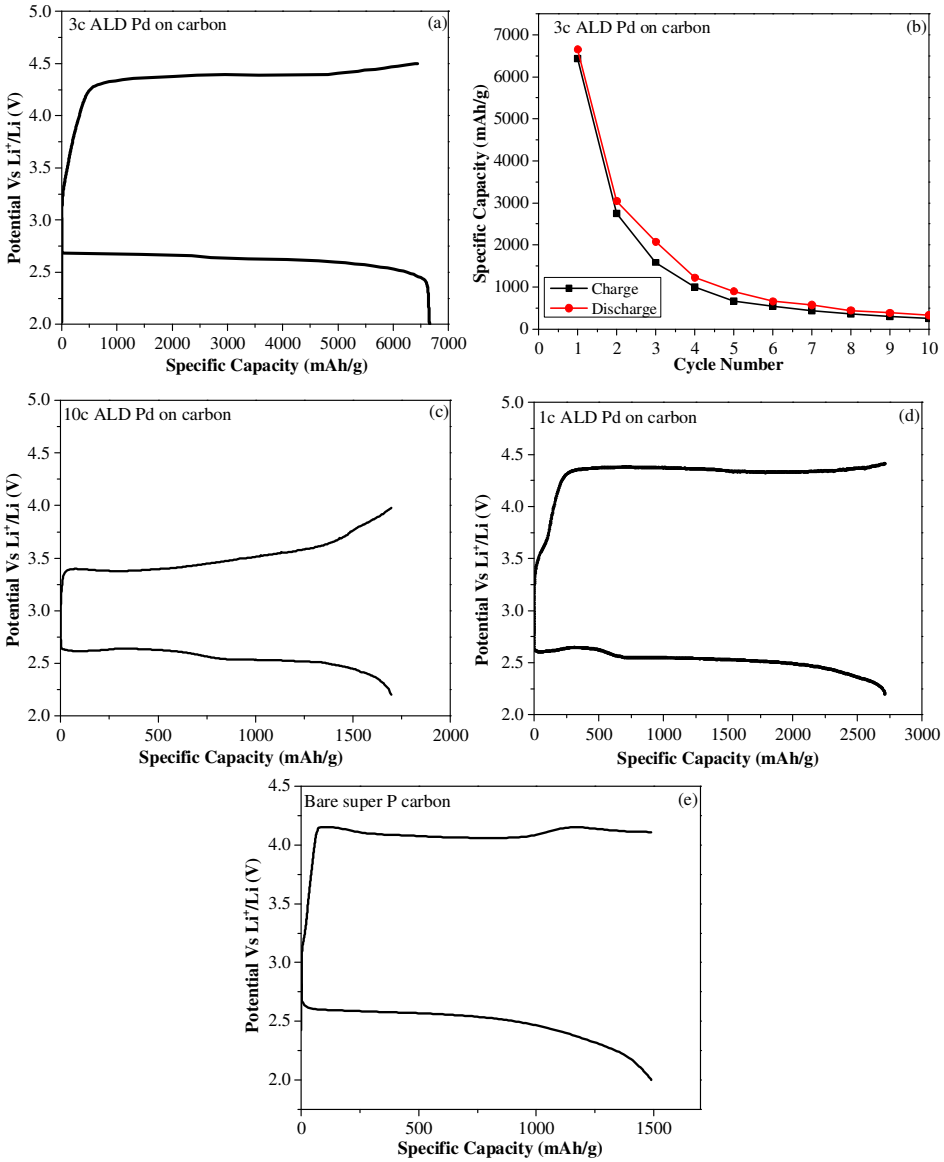

Figure 6.6: Voltage profiles of the first cycle for cathode containing (a) 3c-ALD Pd, (c) 10c-ALD Pd, (d) 1c-ALD Pd, and (e) bare carbon in carbon matrix cycling in 1M $LiCF_3SO_3$/TEGDME at 100 mA/g; (b) Cell capacity as a function of cycle number for air electrodes containing 3c-ALD Pd in carbon matrix cycling in 1M $LiCF_3SO_3$/TEGDME at 100 mA/g.

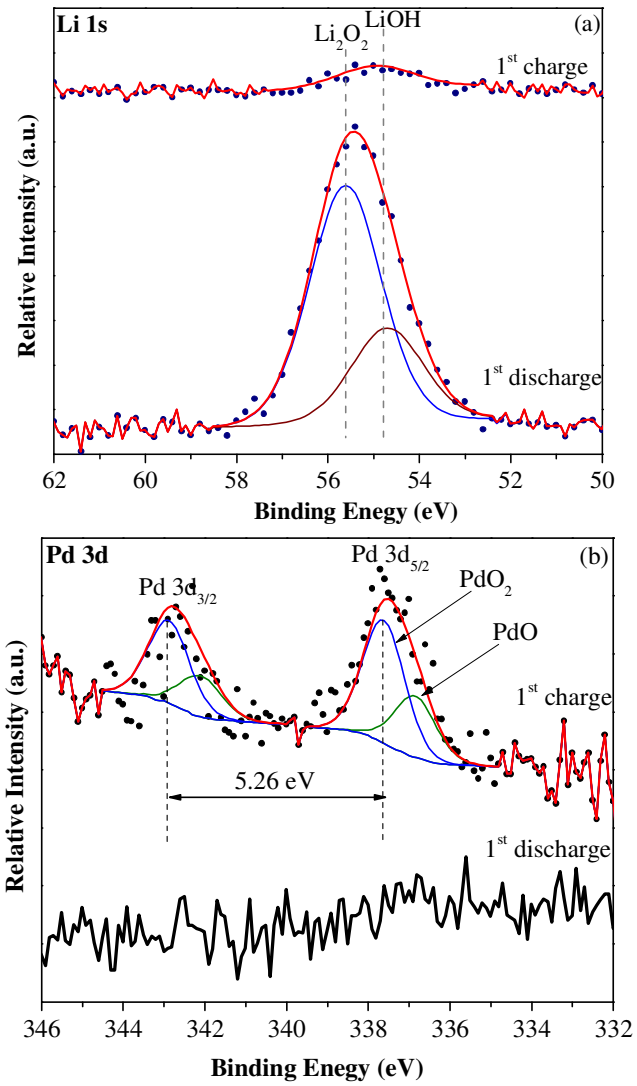

Figure 6.7: XPS spectra of (a) Li 1s and (b) Pd 3d core peaks of the cathode containing as-prepared 10c-ALD Pd/C at different charge/discharge status.

CHAPTER 7

CATHODE ARCHITECTURE II: PALLADIUM NANOPARTICLES ON ZINC-OXIDE-PASSIVATED POROUS CARBON

Reprinted with permission from *Nanotechnology*, **2015**, *26*, 164003.

7.1 Introduction

In this study, I describe an approach based on a cathode architecture that has a protective ZnO coating passivation layer on a porous carbon substrate. Atomic layer deposition (ALD) was applied to prepare these cathode architectures, which addresses the electrolyte decomposition problem by passivating the surface defect sites on the porous carbon. As a consequence, the air cathode based on this modified architecture shows promising results for solving the charge overpotential problem. Bulk zinc oxide (ZnO) has a direct band gap of 3.3 eV, much smaller compared to that of bulk Al_2O_3 (8.8 eV), which has been widely applied as the protective coating material on the defect sites in

various research fields. ZnO ALD using alternating exposures to diethylzinc and water is well understood and provides conformal coatings.[1] In addition, the growth rate of Pd is faster on ZnO surface than on Al_2O_3 surface.[2] All the above advantages make ZnO a promising material as the passivating layer on carbon. Here, graphitized carbon black was first passivated using 2 and 5 ALD cycles of ZnO, followed by 1, 3, and 10 ALD cycles of Pd. The samples were denoted as 1c-Pd/2c-ZnO/C, 3c-Pd/2c-ZnO/C, 10c-Pd/2c-ZnO/C, 3c-Pd/5c-ZnO/C, respectively. The as-prepared samples show high electrochemical catalytic activity in Li-O_2 cells. This cathode architecture reduced the charge overpotential to almost 0 V, the lowest ever reported. The discharge products are characterized by X-ray diffraction (XRD) and scanning electron microscopy (SEM). The effect of the Pd loading on the electrochemical performance of the Li-O_2 cell is also investigated.

7.2 Results and Discussion

The oxidation state and nearest neighbors of the palladium nanoparticles were determined using X-ray absorption near edge structure (XANES) spectra recorded in ambient condition. The XANES spectra of 1c-, 3c- and 10c-Pd on ZnO-passivated carbon are shown in Figure 7.1. Similar to the result in Chapter 6,[3] Pd step edges show a slight shift to lower energy and decreasing whiteline intensity with increasing ALD cycles, suggesting a decrease in the percentage of the oxides component for the Pd nanoparticles.

The XANES linear combination fit was performed to estimate the metal and oxide composition. The Pd nanoparticles primarily exist in the metallic form with 20-25 % oxide species. The percentage of PdO component decreased with increasing ALD cycles. Increasing ALD cycles lead to increase in Pd nanoparticle diameter as well as decrease in percentage of Pd surface atoms. The XANES fittings clearly suggest that the surface Pd atoms are oxidized and the core of the nanoparticles remains metallic.

Figure 7.2a and c illustrate the representative TEM images of the 1-cycle and 3-cycle ALD-Pd on ZnO passivated carbon samples, respectively, which demonstrate a uniform dispersion of the Pd nanoparticles over the carbon substrate. The average size of Pd nanoparticles was determined to be around 3 nm and 6 nm for 1-cycle and 3-cycle ALD-Pd samples, respectively. Compared to the conventional metal oxide surfaces, the Pd particles prepared under similar conditions show much larger particle size on porous carbon.[4-5] In addition, a much higher density of Pd nanoparticles is normally achieved than that on porous carbon due to fewer nucleation sites for the Pd ALD on the carbon substrate, and that Pd diffuses more rapidly on the carbon yielding a smaller number of larger particles, even though the coverage of Pd on carbon surface is still very uniform. These TEM images clearly indicate that the diameter of the Pd nanoparticles increases along with increasing ALD cycles, which is consistent with the XANES results. Figure 7.2b and d show the typical high-resolution TEM images for 1-cycle and 3-cycle ALD-Pd samples, respectively. The lattice fringes for the metal nanoparticles are clearly visible

for both samples, indicating that Pd nanoparticles are well crystalline and faceted. The lattice fringes of the nanoparticles are measured to be ~0.23 nm, consistent with the d-spacing for Pd [111] plane.[6] It should also be pointed out that the porous structure of carbon is well preserved during the process of synthesizing Pd nanoparticles on ZnO passivated carbon samples by ALD, as shown in Figure 7.2e and f. A well preserved porous structure with the appropriate pore size is expected to show high electrochemical performance, since it has been considered one of the major factors that have significant impact on cell capacity and cycle life in Li-O_2 cells.

The electrochemical performance of these cathode architectures was evaluated in a Swagelok-type cell. Figure 7.3a shows the voltage profiles of the first discharge at 2.4 V under a current rate of 100 mAh/g for all the samples. The initial discharge plateau for the 3c-Pd/2c-ZnO/C sample occurs at approximately 2.75 V with a capacity of 1000 mAh/g, which slightly drops to below 2.7 V with a total discharge specific capacity exceeding 10,000 mAh/g. The rest of the cells with different Pd loadings (1c-ALD and 10C-ALD samples), however, delivered much less capacity at the lower discharge plateau. The catalysis is believed to depend on the active sites on the particle surface and the size of the catalyst cluster.[7] For 1c-Pd, the amount of Pd nanoparticles is too small to improve the battery performance. 10c-Pd provide enough catalyst, but the active site is reduced due to the aggregation of the Pd particles. Therefore, Pd loading with the ALD cycle number in between, *e.g.*, 3c-Pd, leads to a higher discharge capacity. It is also

interesting to note that the cell containing 2c-ZnO/C (without Pd loading) as the cathode delivered higher capacity than that of 1c-Pd/2c-ZnO/C sample. Clearly, either the loading or the particle size of the Pd nanoparticle on the ZnO-passivated porous carbon has significant impact on the discharge capacity of the Li-O_2 cell.

Figure 7.3b shows the XRD patterns for cathodes harvested after first discharged, which clearly demonstrates that Li_2O_2 is the main discharge product for all the samples tested in this study. No evidence shows other crystalline species such as Li_2CO_3 or LiOH in the discharge products, although some amorphous compounds cannot be ruled out. Peaks corresponding to the (100), (101), (102), (105) and (110) planes can be indexed to a hexagonal structure Li_2O_2, consistent with the previous reported data. In addition, it can be observed that the intensity of Li_2O_2 for 3c-Pd/2c-ZnO/C sample is much stronger than the other Pd-ZnO-C samples, mainly due to the larger discharge capacity of the former sample. The SEM images of the same discharged cathodes clearly show a large amount of toroid particles covering the whole surface of sample, which is the typical morphology of Li_2O_2 as reported earlier[8] (see Fig. 7.3c-e). However, it appears that the size of the toroidal particle on the discharged 3c-Pd/2c-ZnO/C cathode is much denser and larger than those of the other samples, although a few smaller toroids are also visible between the bigger ones as marked in the figure. Moreover, careful examination of the SEM images indicates that the building blocks of the toroidal discharge products of the Pd/ZnO/C based cathodes are distinctly different, *i.e.*, 10c-Pd/2c-ZnO/C discharge

products are made up of nanofibers; 1c-Pd/2c-ZnO/C discharge products consist of smaller and more spherical nanoparticles, while 3c-Pd/2c-ZnO/C discharge products contain much bigger and denser nanoparticles. This finding provides strong evidence that the oxygen reduction reaction during discharge in the Li-O2 cell is significantly altered when Pd nanoparticles on ZnO passivated carbon are used as the electrocatalyst, which not only contributes to a higher capacity by providing more active sites for the ORR reaction in the case of 3c and 10c ALD-Pd samples, but also leads to a different morphology of the discharge products.

In order to reveal the catalytic activity on the oxygen evolution reaction (charging) of the Pd/ZnO/C based cathodes, I applied a capacity-controlled mode to investigate the discharge/charge behavior of the Li-O_2 cell.[3, 7] Under this mode, the cutoff charging condition is specified so that the charge capacity matches the previous discharge capacity, in this case 1,000 mAh/g, while charge potential is limited to 4.5 V. Figure 7.4 shows voltage profiles recorded from the discharge/charge cycles obtained from the cells with the two different types of cathode architectures, *i.e.*, ZnO passivated graphitized carbon (ZnO/C) and Pd nanoparticles on ZnO passivated graphitized carbon (Pd/ZnO/C). The voltage profiles exhibit that the charge potential is ~4.0 V for the ZnO/C cathode, which is significantly reduced to 3.0 V for all the Pd/ZnO/C cathodes. The observed low charge potential was able to be maintained for over 10 cycles at 1,000 mAh/g capacity. Even more striking, a lowest charge potential at around 2.8 V is observed for the cell

using 1c-Pd/2c-ZnO/C cathode (Fig. 7.4b), which leads to an extremely high round-trip efficiency (>95%) of the cell. Considering that the thermodynamically-determined potential of oxygen evolution reaction from Li_2O_2 is 3.0 V,[9-10] such low charge potential may indicate a completely different reaction pathway from the previous literatures when the Pd/ZnO/C-based materials are used as the cathode in the Li-O_2 cell. While the loading of Pd affects the performance of the Li-O_2 battery, the effect of the ZnO loading on carbon is minor. Figure 7.4c and e show that the voltage profiles from the discharge/charge cycles are similar between 3c-Pd/2c-ZnO/C and 3c-Pd/5c-ZnO/C.

The above results demonstrated that the ALD Pd/ZnO tandem bilayer on carbon has been found to be effective cathode architecture for increasing the discharge capacity and reducing the charge overpotential of Li-O_2 batteries. Although the mechanism is still not clear at the current stage, it is believed that both ZnO and Pd play the critical roles in enhancing the performance of the cell. In particular, the ALD ZnO thin film partially covered the carbon surface and was selectively decorated at the carbon defect sites, which help to minimize side reaction such as electrolyte decomposition and formation of lithium carbonate on the defect sites. The density functional theory (DFT) calculations by Lu *et al*. showed that small Al_2O_3 islands prepared by ALD were small enough that it itself is conductive.[11] A material that is more conductive than Al_2O_3, such as ZnO in this case, would be beneficial to the overall conductivity of the carbon cathode when it is used to passivate the carbon defect sites. Subsequent Pd ALD will selectively deposit uniform Pd

nanoparticles on top of or at the edge of ZnO layer because the carbon surface can be considered inert for Pd ALD. These highly dispersed Pd nanoparticles acted as the electrocatalyst for promoting the discharge and charge reactions, and consequently, the electrochemical performance of the Li-O_2 cells is significantly improved in terms of the discharge capacity and, particularly, the reduction of the charge overpotential.

Finally, it should also be pointed out that the cells with Pd/ZnO/C-based cathode started to fade with a relatively short discharge/charge cycles, even under the capacity-controlled mode. One of the possible reasons that cause the failure of the cell is the degradation of Li anode as shown by the corrosion of the anode at the end of the cycle, while the cathode still maintains its porous structure, as shown in Figure 7.5. The degradation of Li anode in Li-O_2 cells is due to the oxygen-crossover effect, which results in the formation of LiOH and Li_2CO_3, as shown in the work of Assary *et al.*[12-13] Therefore, the protection of the Li anode against the oxygen crossover is one of the key factors in improving the cycle life of the Li-O_2 cells.

7.3 Conclusions

In conclusion, atomic layer deposition (ALD) was used to deposit nanostructured palladium on ZnO-passivated porous carbon as the cathode material for Li-O_2 cells. Comparing to the Pd/Al_2O_3/C cathodes,[11] the ZnO-passivated ones further reduce the charge overpotential and lead to a better cyclability. The results demonstrated that the

oxygen reduction reaction during discharge in the Li-O_2 cell is significantly altered when Pd nanoparticles on ZnO passivated carbon are used as the electrocatalyst, which not only contributes to a higher capacity by providing more active sites for the ORR reaction in the case of 3c and 10c ALD-Pd samples, but also leads to a different morphology of the discharge products. The results also showed that the ALD Pd/ZnO tandem bilayer on carbon is effective cathode architecture for significantly decreasing the charge potential of Li-O_2 batteries, which leads to a high round-trip efficiency of the cell.

7.4 References

1. Elam, J. W.; Sechrist, Z. A.; George, S. M. *Thin Solid Films* **2002**, *414*, 43-55.

2. Feng, H.; Elam, J. W.; Libera, J. A.; Setthapun, W.; Stair, P. C. *Chem. Mater.* **2010**, *22*, 3133-3142.

3. Lei, Y.; Lu, J.; Luo, X.; Wu, T.; Du, P.; Zhang, X.; Ren, Y.; Wen, J.; Miller, D. J.; Miller, J. T.; Sun, Y. K.; Elam, J. W.; Amine, K. *Nano Lett.* **2013**, *13*, 4182-4189.

4. Feng, H.; Libera, J. A.; Stair, P. C.; Miller, J. T.; Elam, J. W. *ACS Catalysis* **2011**, *1*, 665-673.

5. Lu, J.; Stair, P. C. *Langmuir* **2010**, *26*, 16486-16495.

6. Shao, M.; Yu, T.; Odell, J. H.; Jin, M.; Xia, Y. *Chem. Commun.* **2011**, *47*, 6566-6568.

7. Lu, J.; Cheng, L.; Lau, K. C.; Tyo, E.; Luo, X.; Wen, J.; Miller, D.; Assary, R.; Wang, H.-H.; Redfern, P.; Wu, H.; Park, J.-B.; Sun, Y.-K.; Vajda, S.; Amine, K.; Curtiss, L. A. *Nat. Commun.* **2014**, 5:4895.

8. Thapa, A. K.; Saimen, K.; Ishihara, T. *Electrochem. Solid-State Lett.* **2010**, *13*, A165-167.

9. Bruce, P. G.; Freunberger, S. A.; Hardwick, L. J.; Tarascon, J.-M. *Nat. Mater.* **2012**, *11*, 19-29.

10. Lu, J.; Amine, K. *Energies* **2013**, *6*, 6016-6044.

11. Lu, J.; Lei, Y.; Lau, K. C.; Luo, X.; Du, P.; Wen, J.; Assary, R. S.; Das, U.; Miller, D. J.; Elam, J. W. *Nat. Commun.* **2013**, 4:2383.

12. Assary, R. S.; Lu, J.; Du, P.; Luo, X.; Zhang, X.; Ren, Y.; Curtiss, L. A.; Amine, K. *ChemSusChem* **2013**, *6*, 51-55.

13. Assary, R. S.; Lu, J.; Luo, X.; Zhang, X.; Ren, Y.; Wu, H.; Albishri, H. M.; El-Hady, D. A.; Al-Bogami, A. S.; Curtiss, L. A.; Amine, K. *ChemPhysChem* **2014**, *15*, 2077-2083.

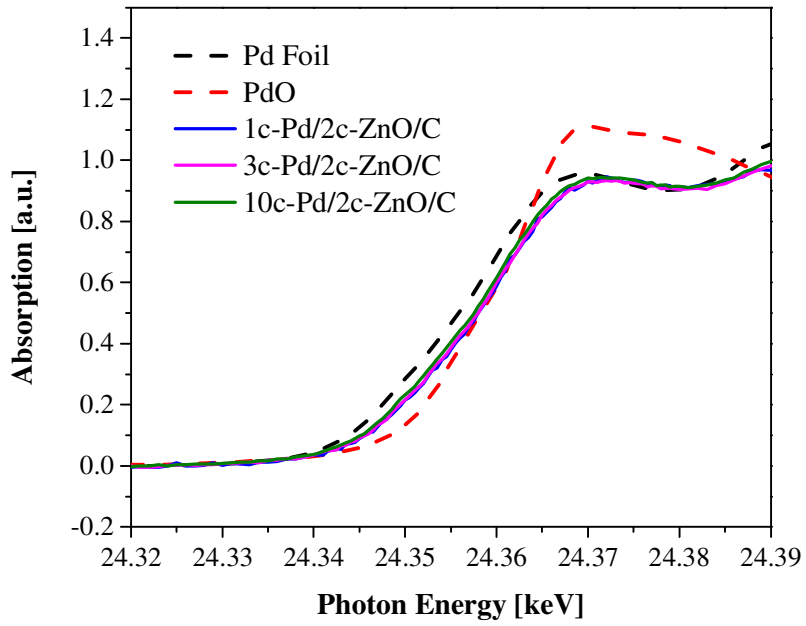

Figure 7.1: XANES spectra for the reference samples Pd Foil and PdO, and for the as-prepared Pd/ZnO/C samples

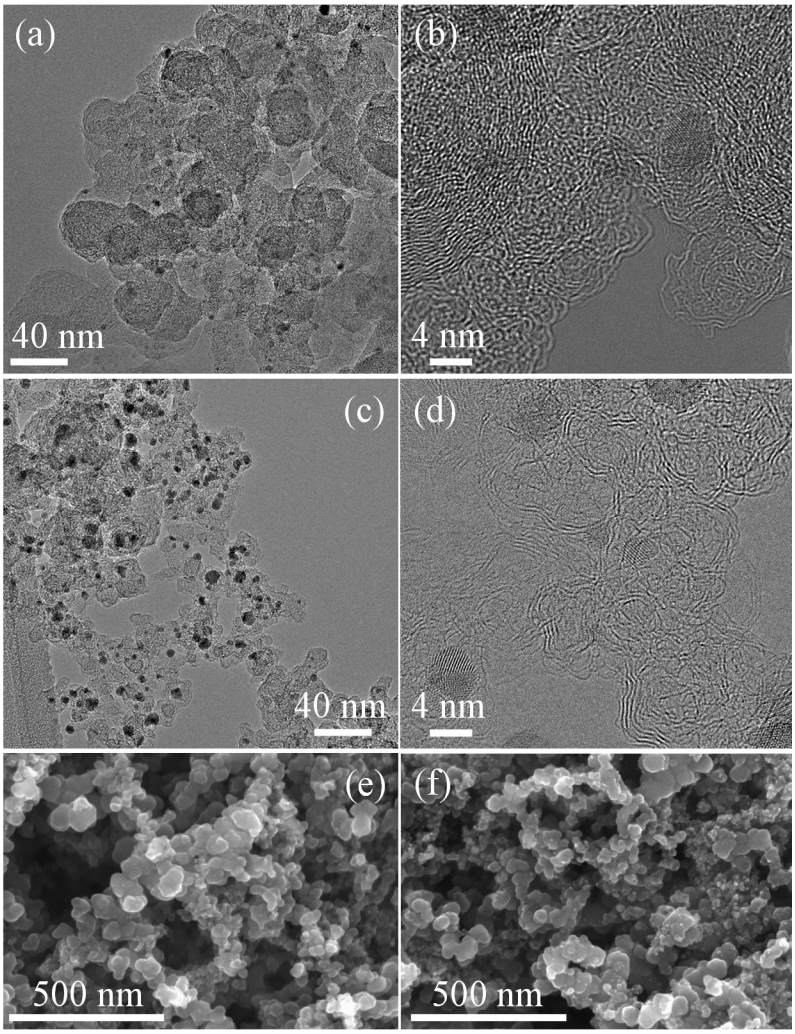

Figure 7.2: TEM images for (a)(b) 1c-Pd/2c-ZnO/C and (c)(d) 3c-Pd/2c-ZnO/C samples. SEM images for (e) carbon substrate and (f) 10c-Pd/2c-ZnO/C sample.

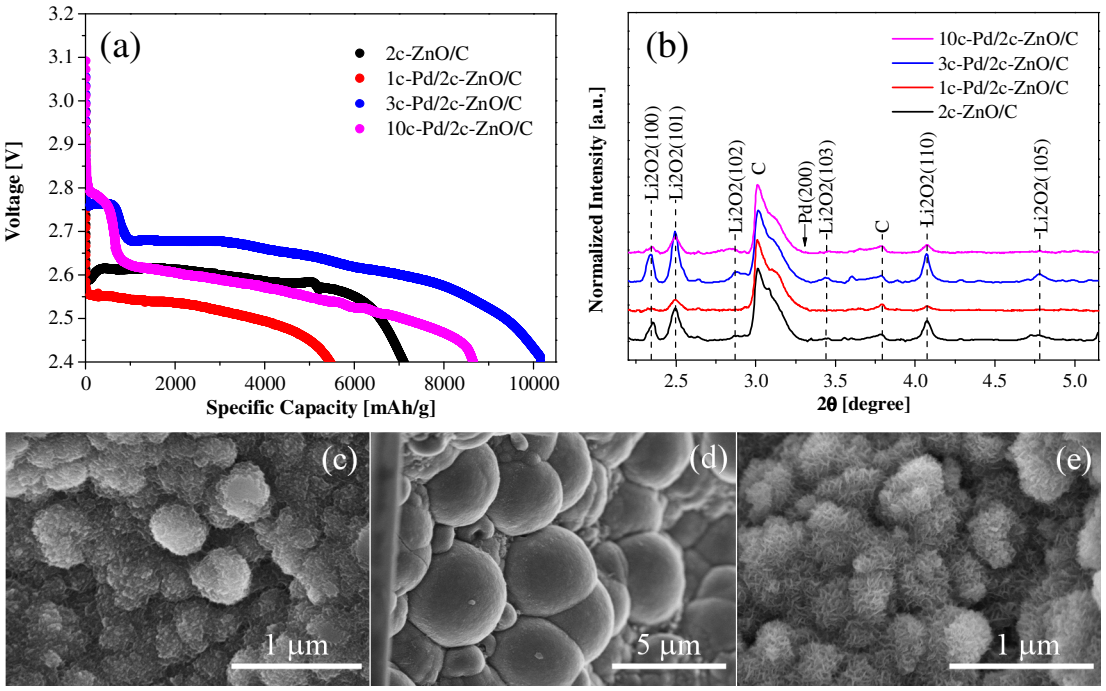

Figure 7.3: Discharge products studied by diffraction patterns and SEM images. (a) Voltage profiles and (b) XRD patterns of the cathodes discharged to 2.4 V. SEM images for the discharges cathodes (c) 1c-Pd/2c-ZnO/C, (d) 3c-Pd/2c-ZnO/C, and (e) 10c-Pd/2c-ZnO/C.

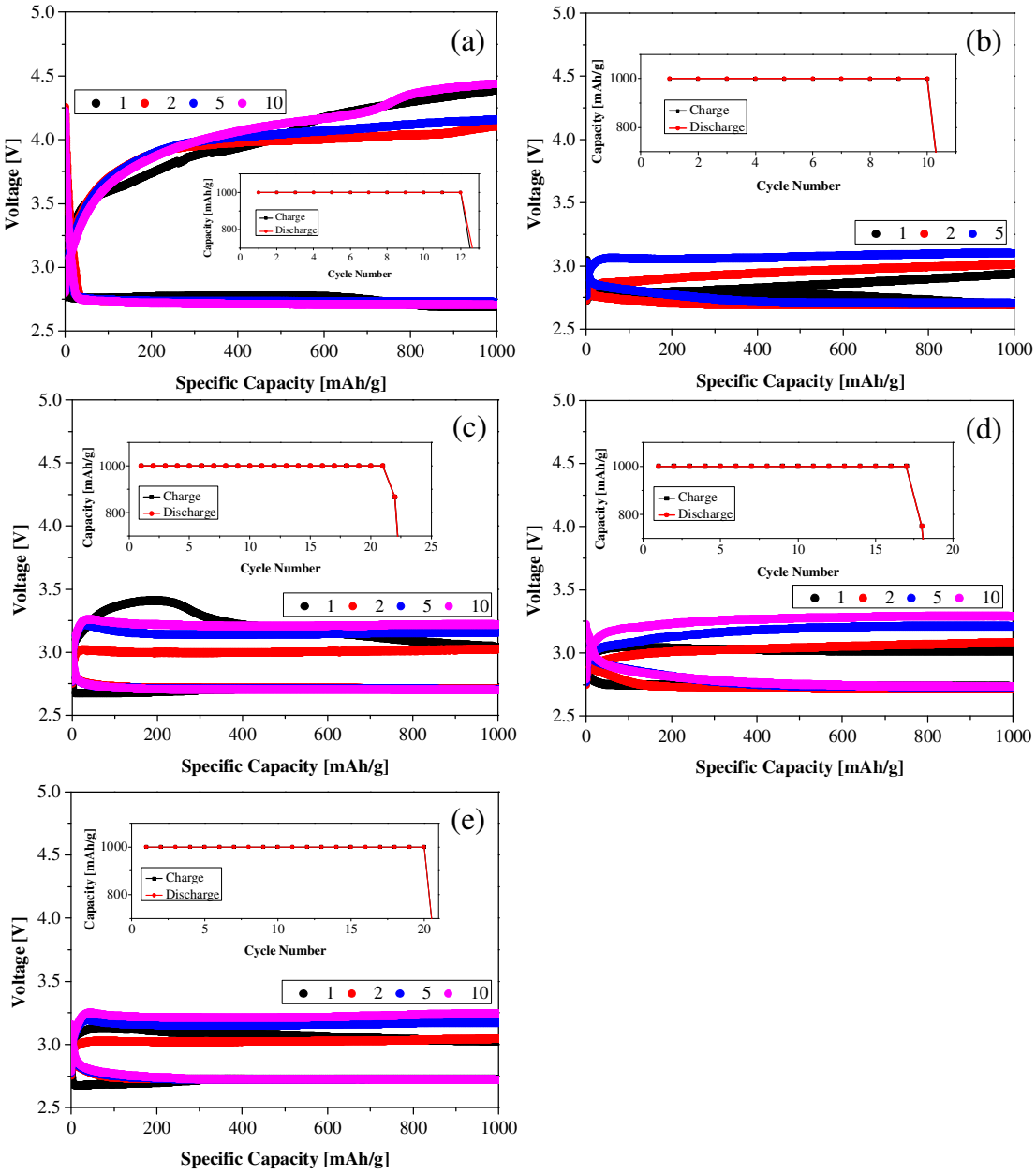

Figure 7.4: Voltage profiles for the 10 hr time controlled mode of the cathode (a) 2c-ZnO/C (b) 1c-Pd/2c-ZnO/C (c) 3c-Pd/2c-ZnO/C (d) 10c-Pd/2c-ZnO/C (e) 3c-Pd/5c-ZnO/C.

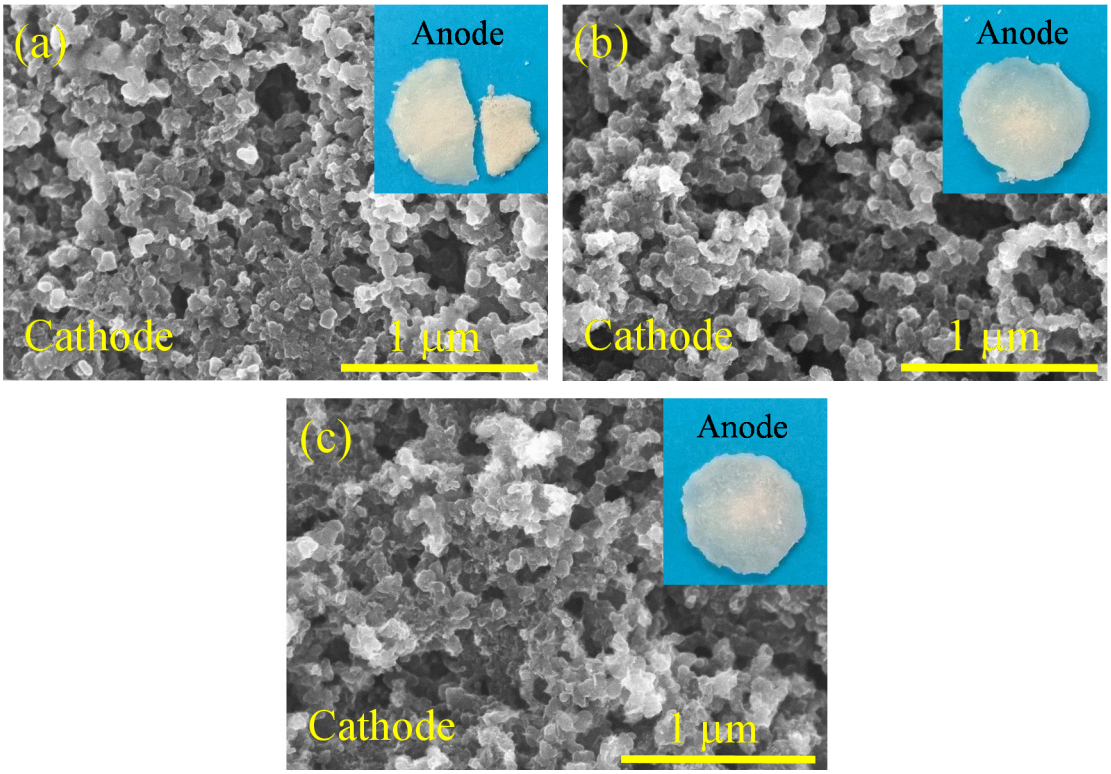

Figure 7.5: SEM images for cathodes and images of the degraded Li anode after discharge/charge cycles (stop at charge) (a) 1c-Pd/2c-ZnO/C, (b) 3c-Pd/2c-ZnO/C, and (c) 10c-Pd/2c-ZnO/C.

CHAPTER 8

CONCLUSIONS

My research aims at the current major hurdles of aprotic Li-O_2 battery, including the underlying mechanism of the electrochemical processes, the promising techniques for cathode architecture, and the stability of the materials used for cathode, anode, and electrolyte. Besides the above, this dissertation is an attempt to establish connections among various aspects, with the hope of improving the battery system holistically.

The major findings of this dissertation study are as follows:

(1) The insoluble discharge product, Li_2O_2 particles, accumulate on the O_2-breathing cathode to form toroidal shape, which clogs the pores and covers the active sites in the cathode. During the charge process, Li_2O_2 decomposes into Li^+ ions and O_2 by OER, and releases the O_2 diffusion paths and the active sites. The different discharge capacities lead to the multifarious morphology of discharge product, and affect the following charge process in the aspects of overpotential, reaction rate, *et al*. For deep discharge, extra energy is needed to break the chemical bonds of the discharge products, causing a high overpotential. Additionally, the corresponding charge reaction would not

completely decompose the Li_2O_2 toroid. The remaining grains block the diffusion path of O_2, decrease the porosity of the cathode after cycles, and lead to a sudden death of the cell. AIMD and DFT calculation was applied to simulate the mass and charge transportation. The simulation results indicate that the active species become immobile once the Li_2O_2 chemical bonds formed. The continous accumulation of the discharge products not only clog the pores in the O_2-breathing cathode, but also hinder the charge transfer process.

(2) At the present stage in the research of aprotic Li-O_2 battery, high overpotential of the electrochemical reactions has been the primary cause of the instability of the aprotice electrolyte and bad cyclability of the battery. A variety of factors has been found to dictate the electrochemical reactions, such as the nature of the electrocatalyst and the surface structure of the porous carbon cathode. Atomic layer deposition (ALD) was used to synthesize catalyst nanoparticles on a porous carbon substrate. The nanoparticles are uniformly dispersed with the size control, while the surface structure of the carbon substrate is well persevered. The resulting materials were employed as the cathode materials in rechargeable aqueous Li-O_2 battery, and demonstrated a superior catalytic activity and electrochemical behavior.

(3) Furthermore, ALD is applied to uniformly nanostructured palladium on Zn-passivated porous carbon substrate. The cathode architecture reduced the charge overpotential to almost 0 V. The results demonstrated that the oxygen reduction reaction

during discharge in the Li-O_2 cell is significantly altered when Pd nanoparticles on ZnO passivated carbon are used as the electrocatalyst and also showed that the ALD Pd/ZnO tandem bilayer on carbon is an effective cathode architecture for significantly decreasing the charge potential of Li-O_2 batteries, which leads to a high round-trip efficiency of the cell.

PUBLICATIONS

1. ***X Luo***†, M Piernavieja-Hermida†, J Lu, T Wu, J Wen, Y Ren, D Miller, ZZ Fang, Y Lei, and K Amine. Pd Nanoparticles on ZnO-passivated Porous Carbon by Atomic Layer Deposition: an Effective Electrochemical Catalyst for Li-O_2 Battery. ***Nanotechnology***, 2015, *26*, 164003. (special issue article; invited)

2. Y Lei†, J Lu†, ***X Luo***†, T Wu, P Du, X Zhang, Y Ren, JT Miller, YK Sun, JW Elam, and K Amine. Synthesis of Porous Carbon Supported Palladium Nanoparticle Catalysts by Atomic Layer Deposition: Application for Rechargeable Lithium-O_2 Battery. ***Nano Lett.***, 2013, *13*, 4182-4189.

3. ***X Luo***, J Lu, ZZ Fang, and K Amine. Growth of Li_2O_2 on Carbon Cathode in a Li-Air Cell: A Self-Assembly Process. 223rd Electrochemical Society (ECS) spring meeting, Toronto, ON, Canada (May 12-16, 2013). Meeting Abstracts 527

† These authors contributed equally